

August 1, 2015  
Edition 2

---



Graham Lau (Department of Geological Sciences) in the Canadian High Arctic  
Photo Courtesy of John Spear (Colorado School of Mines)





---

# Table of Contents:

---

## About the STEMinar

### Year in review

### An archive of the talks and abstracts from the Spring 2015 semester

### Student features of some of our grant winners

-----

<b><i>Optical frequency combs for optical frequency metrology</i></b>	1
Daniel Cole (Dept. of Physics)	
<b><i>Dynamic homogenization of damped periodic materials</i></b>	10
Michael Frazier (Dept. of Aerospace Engineering)	
<b><i>Attention allocation to racial outgroups</i></b>	21
Steffanie Guillermo (Dept. of Psychology)	
<b><i>The effects of gender composition in a group math task</i></b>	24
Sarah Grover (Dept. of Psychology)	
<b><i>Tracking supraglacial lake changes on Ngozumpa glacier, Nepal</i></b>	33
Ulyana Horodyskyj (Dept. of Geological Sciences)	
<b><i>Band gap characterization of two-dimensional damped phononic crystals</i></b>	44
Romik Khajehtourian (Dept. of Aerospace Engineering)	
<b><i>The geobiology of sulfur springs at Borup Fiord Pass</i></b>	52
Graham Lau (Dept. of Geological Sciences)	
<b><i>Combining CFD and distributed pressure sensors for wind sensing with UAS</i></b>	60
Roger Laurence III (Dept. of Aerospace Engineering)	
<b><i>Knots and links</i></b>	65
Caroline Matson (Dept. of Mathematics)	

***An introduction to homotopy type theory***

71

Mark Pullins (Dept. of Mathematics)

***Simulation of impact of bubble dynamics on cell membrane using an adaptive wavelet code***

77

Navid Shervani-Tabar (Dept. of Mechanical Engineering)

# About the STEMinar:

The STEMinar is a graduate student organization at CU Boulder which seeks to promote interdisciplinary interaction among graduate students in STEM departments. The STEMinar hosts seminars given by graduate students about their research. The talks are intended to be relatively non-technical, so that they can be accessible to a broad range of graduate students.

STEMinar speakers have come from a variety of STEM departments including computer science, mathematics, geology, psychology, integrative physiology, physics, chemistry, evolutionary biology, and several engineering sub-disciplines including aerospace and mechanical. During the Spring 2015 semester, STEMinar talks attracted audience members from at least 10 departments on campus. Moreover, since its inception in August 2013, a majority of the STEMinar talks have been presented by women graduate students, a traditionally under-represented group in STEM disciplines. We hope to continue to find ways to foster diversity and community among the graduate students at CU Boulder.

Thanks to a generous contribution from John Stevenson, the Dean of the CU Boulder Graduate School, the STEMinar has put into place a grant giving program. The individuals who received a \$250 STEMinar grant during the Spring 2015 semester were asked to contribute a short document which summarizes their current research project, or reviews a STEM topic that they are interested in writing about. We have encouraged the authors of these papers to address, if possible, how their research relates to other fields, everyday life, etc.

The STEMinar Journal consists of the following:

- A brief year in review of the STEMinar with updates about the future.
- A list of the talks that were presented during the Spring 2015 semester.
- The papers that were submitted by our grant recipients during the Spring 2015 semester.
- Student features of some of our grant winners.

We believe that this journal will highlight the ongoing research that is being done by STEM graduate students at CU Boulder.

-----

**STEMinar Organizer:**

Trubee Davison (Mathematics)

**STEMinar Advisory Committee:**

Trubee Davison (Mathematics)

Sarah Grover (Psychology)

Marianne Reddan (Cognitive Psychology)

## Year in Review:

This year was the second year of the STEMinar organization. We awarded 18 STEMinar grants, giving out nearly \$7500. These funds will directly help graduate students continue to pursue their research aspirations. Here are a few examples of how the grants were used:

- Purchasing math textbooks (graduate student in math)
- Purchasing a new laptop for lab experiments (graduate student in mechanical engineering)
- Offsetting expenses associated to doing a survey for a psychology study (graduate student in psychology)
- Offsetting travel expenses for a student to speak on his research about phonons at a conference in Paris (graduate student in aerospace engineering)

In addition to the grant giving program, and the bi-monthly research seminars, the STEMinar also organized several social events, including a keynote event called Speed Data-ing. This event included a talk by CU Professor Randy O'Reilly of the Psychology Department about how to be a successful graduate student. It was very entertaining and informative. Here is Dr. O'Reilly being introduced by Marianne Reddan and Sarah Grover, the future co-organizers of the STEMinar.



During the speed data-ing, graduate students were able to meet other graduate students from a variety of STEM departments, and learn about their research. This event was generously sponsored the United Government of Graduate Students (UGGS). Below is photograph of the speed data-ing. It was held at eTown, an event center in downtown Boulder, CO.



We also collaborated with a campus organization called the Forum on Science Ethics and Policy (FOSEP). Their primary mission is to promote civic dialogue about issues at the intersection of science and society across the CU campus and community. We encourage the readers to check out their website at:

<https://fosepcu.wordpress.com/>

Below is a photograph of one our joint happy hours with FOSEP where we discussed a range of science related issues that permeate society. They were well attended and informative.



Beginning in the Fall of 2015, the STEMinar will be co-organized by Sarah Grover and Marianne Reddan, who are both PhD students in the Psychology department. Here are Sarah and Marianne at the Speed Data-ing event last year.



# Spring 2015 STEMinar Speakers:

- Fnu Shikhar : January 22, 2015
  - Dept. of Mechanical Engineering
  - [Fnu.Shikhar@colorado.edu](mailto:Fnu.Shikhar@colorado.edu)

## **Ceramic responses under electric fields**

*Materials have been broadly divided in 3 major categories: Metal, polymer and ceramics. Some common examples of ceramic are serving plates, bricks, tiles, etc. But do you know Ceramics are the core features in sensors, semiconductors, superconductors, electrical insulation, rocket-body, bio-engineering, heat insulations? This presentation will try to draw attention towards Ceramics, such as, how is a ceramic different from metal or polymer and why should we care about them? How are they made and how my research would help to improve some fairly old ceramic synthesis problems. We use electric field on ceramics to lower down the temperature and time required for their synthesis. Followed by this, I shall present how this new technique, named as “Flash Sintering”, has altered some of the basic properties of ceramic, what are their potential applications and the science behind them.*

- Ulyana Horodyskyj: February 5, 2015
  - Dept. of Geological Sciences
  - [Ulyana.Horodyskyj@colorado.edu](mailto:Ulyana.Horodyskyj@colorado.edu)

## **Tracking supraglacial lake changes on Ngozumpa glacier, Nepal**

*The formation of supraglacial (surface) lakes appears to be a catalyst for ice mass loss on debris-covered glaciers in the Himalaya. Once formed, these lakes can grow through expansion, by melting and collapsing of surrounding ice walls, and through deepening of their ice floors. As lake water volume increases, so too does the risk for glacial lake outburst floods (GLOFs). Spillway Lake, a large supraglacial base-level lake on Ngozumpa, one of Nepal’s largest and longest glaciers, has been growing since the 1980s. This research utilized time-lapse cameras, weather stations, temperature buoys, and sonar to track these changes in real-time.*

*Oblique-view time-lapse imagery of lakes reveals that multiple drain and refill events, on the meter-scale, can occur during a melt season. Less frequent overhead satellite imagery cannot account for this volume loss, stressing the importance for continued “boots-on-the-ground” observations. Vertical temperature distribution in the sub-basins of Spillway Lake reveal mostly isothermal conditions in the summer, indicating the lake is well-mixed due to constant inputs of meltwater both from above ground (ice walls) and at depth, from englacial and/or subglacial channels. Lake floor melting rate is highest in the*

*fall season, after surface melting ceases and the lake bodies have had sufficient time to accumulate heat. However, the presence of thick debris (mud and rock) on lake floors can insulate the ice from melting. Sonar imaging and 3D model construction of lake floors reveal areas prone to future deepening, which should continue to be monitored in the future.*

- Katharine Adamyk: February 12, 2015
  - Dept. of Mathematics
  - [Katharine.Adamyk@colorado.edu](mailto:Katharine.Adamyk@colorado.edu)

### **Decryption of micronuclear precursors of somatic genes in certain ciliate species**

*It has been postulated that the decryption of micronuclear precursors of somatic genes in certain ciliate species occurs by constrained reversals and block interchanges. Not all permutations are sortable by these constrained sorting operations. We find a linear time criterion for determining which permutations are sortable by constrained block interchanges. For permutations not sortable by constrained block interchanges, we find a linear time criterion for determining which permutations are the final results of attempted sorting by constrained block interchanges. The corresponding theory for constrained reversals appears more complicated and we present partial results for this operation. The constrained sorting operations suggest natural two-player games. By a classical theorem of Zermelo, these games are determined -- that is, some player has a winning strategy. We consider the decision problem of determining which player has a winning strategy in a specific instance of a game.*

- Jordan Holquist: March 5, 2015
  - Dept. of Aerospace Engineering
  - [Jordan.Holquist@colorado.edu](mailto:Jordan.Holquist@colorado.edu)

### **Direct generation of oxygen from electrocatalytic carbon dioxide reduction**

*What is the current direction of NASA? Are they going to an asteroid? The Moon? Mars? I can't actually answer any of these questions, but one thing is certain: no matter the destination, technology development to enable upcoming exploration is a critical need. In my presentation, I'll briefly discuss technology development needs to advance human spaceflight and how you can get involved (read: funding sources and research opportunities that apply to all STEM disciplines).*

*After that, I'll talk about my particular research: the direct generation of oxygen from electrocatalytic carbon dioxide reduction using room-temperature ionic liquid catalysts. This will include an overview of the state of the art of oxygen generation/carbon dioxide reduction on board the International Space Station, a brief introduction to electrochemistry, and ionic liquid chemistry. This technology is not only critical for closing*

*the consumables loop on board spacecraft, but also has implications for carbon-neutral fuel sources, greenhouse gas emissions, and solvent chemistry.*

- Janet Tsai: March 19, 2015
  - Dept. of Mechanical Engineering
  - [Janet.Tsai@colorado.edu](mailto:Janet.Tsai@colorado.edu)

### **The brutalist engineering center: 1965 - 2015**

*As the E in STEM, Engineering is typically grouped with its related disciplines - science and mathematics. Yet unlike these "pure" disciplines, engineering as we know it is relatively new, having only developed its white-collar image in the early days of the Cold War, space race, and founding of NASA.*

*Here at CU, we have a physical reminder of this 1960s makeover of engineering - our Engineering Center Building. Tracing back the conditions which led to this unique building's design and construction, we debunk some contemporary rumors and see how this concrete behemoth still affects how we teach and learn today. While it's no longer the state-of-the-art beacon of space age engineering it was once intended to be, the building has successfully contained our activities for the better part of five decades. Janet will present some fascinating research on the Engineering Center, including a glimpse into the era in which it was built, and what the building means for us as researchers and educators today.*

- Daniel Feucht: April 2, 2015
  - Dept. of Geological Sciences
  - [Daniel.Feucht@colorado.edu](mailto:Daniel.Feucht@colorado.edu)

### **Geophysical imaging of the Rocky Mountain Front Range: Implications for support of high topography in Colorado**

*Have you ever wondered why Denver is the mile high city? Or why the Rocky Mountains are there at all? You probably can guess that it has something to do with plate tectonics, but as it turns out, the Rockies and the adjacent High Plains appear to be something of a special case. The origin of the southern Rocky Mountains, along with their persistence as a mountain range for more than 40 million years, is a hot topic in geology these days and several researchers at CU Boulder are leading the charge to explain this enigmatic landscape of Colorado that we all too often take for granted.*

*In my STEMinar talk I'll present an overview of how mountains are built and maintained over geologic time, discuss how these processes relate to the mountains in our own backyard, and then present my own contribution to the Rocky Mountains puzzle in the*

*form of a large-scale magnetotelluric survey of the Rocky Mountain Front Range in Colorado. Magnetotellurics is a passive electromagnetic geophysical imaging technique that provides a measure of the electrical properties of the Earth at depth. By interpreting electrical properties of the crust and upper mantle in a geologic context we can estimate the distribution of temperature, melt, fluids, and altered mineral composition at depth and in turn say something about which of these mechanisms contributes to the high topography that we see today.*

- Chelsea Heveran: April 9, 2015
  - Dept. of Mechanical Engineering
  - [Chelsea.Heveran@colorado.edu](mailto:Chelsea.Heveran@colorado.edu)

### **Bone quality is impaired in chronic kidney disease**

*What makes a bone strong and tough? What about bone changes to become fragile in aging or disease? In this talk, we will take a tour from the macro to nano scales to explore what makes (and what breaks) this hierarchical and dynamic composite tissue. We will also consider how bone microstructure and material properties contribute to an overall "bone quality." Lastly, we will discuss my progress in understanding how Chronic Kidney Disease, common among the elderly, compromises bone quality to increase skeletal fragility in a large and growing clinical population.*

- Sarah Grover: April 16, 2015
  - Dept. of Psychology
  - [Sarah.Grover@colorado.edu](mailto:Sarah.Grover@colorado.edu)

### **Building bridges: Moving towards a scientific understanding of positive cross-sex interactions in STEM and why we should care**

*This talk presents social psychological theory and research to understand environmental factors that increase women's belonging in STEM. The talk will be given in 3 parts:*

- 1. On the emergent properties of groups: How group interactions shape our self-concept.*
- 2. Present research: Two studies examining the consequences of gender composition in a small group math task for women's performance, the social cohesion they experience with their group members, and self- and others' perceptions of their math ability.*
- 3. Future directions: What are the barriers to positive cross-sex contact and how can they be overcome? What are the verbal and non-verbal cues of group inclusion, and how can they be measured?*

- Navid Shervani-Tabar: April 23, 2015
  - Dept. of Mechanical Engineering
  - [navidst@colorado.edu](mailto:navidst@colorado.edu)

**Complex geometry flows: an approach to simulate the flow over obstacles which has been developed in "Multiscale modeling laboratory"**

- Graham Lau: April 30, 2015
  - Dept. of Geological Sciences
  - [Graham.Lau@colorado.edu](mailto:Graham.Lau@colorado.edu)

**Something's eating the yellow snow**

*Sulfur is one of the most abundant elements in the universe and is essential for life as we know it. Characterizing the role of biology in the geochemical cycling of sulfur from regional to global scales is important for the future exploration of other worlds in our solar system and beyond. For this STEMinar, I will present my research on microbial sulfur cycling within a supraglacial sulfur spring system in the Canadian High Arctic. I'll talk about what we know and have yet to learn about the biological and abiotic processes that are responsible for cycling sulfur at this field site (and I'll also show lots of pretty pictures from my field work).*

## Student Features:

**Ulyana Horodyskyj: Dept. of Geological Sciences**



One of Ulyana's first memories of the mountains is from a trip to the Swiss Alps with her family, when she was just 6 years old. She witnessed an avalanche in the distance while having a snowball fight at 10,000 ft. with her two older brothers. Since then, there has not been an end in sight for her, in regards to exploration of the natural world.

Prior to entering the program at CU, Ulyana completed a B.S. in earth sciences at Rice University and a M.Sc. in planetary geology at Brown University. Her studies have taken her all over the world: from climbing peaks at the top of the world in the Nepalese Himalaya to working on an icebreaker at the bottom of the world in Antarctica.

Ulyana loves working with students and has been able to do this through National Geographic Student Expeditions (Iceland, in 2009/10) and the Girls on Ice science and mountaineering program on Mt. Baker, Washington (2014) and Gulkana glacier, Alaska (2015). From 2011-2013, during the course of her PhD, she traversed over one thousand miles in Nepal, collecting data and funding it via a USAID climber-scientist grant, a Fulbright fellowship to live abroad in Nepal, and crowd fundraising. She created the "Sherpa-Scientist Initiative" to educate locals on changing climate and how to continue to monitor it, as well as welcomed the help of Westerners along the way. Ulyana hopes to continue on this path of citizen science through collaborations with companies including Discovery Channel International,

Vanguard Diving and Exploration (Canada), Midwest ROV LLC (Wisconsin), and Crater Exploration (Alaska).

## Graham Lau: Dept. of Geological Sciences



Graham Lau earned undergraduate degrees in biology and chemistry from York College of Pennsylvania in 2007. He studied astrophysics and geology at the University of Colorado Boulder before entering a graduate program centered on astrobiology. His Ph.D. research, funded by the National Science Foundation and NASA, focuses on microbial sulfur cycling in polar environments. Graham's career has focused on public engagement and science education. Graham can be followed through his blog, A Cosmobiologist's Dream, at [cosmobiologist.blogspot.com](http://cosmobiologist.blogspot.com).

## Roger “Trey” Laurence III: Dept. of Aerospace Engineering



I am originally from Miami, Florida, and received my undergrad degree in Mechanical Engineering from Florida International University. I am currently pursuing a PhD in Aerospace Engineering Sciences. I was drawn to the aerospace field because I felt that aerospace, more so than almost any other field, was pushing the bounds of what is possible within the realm of engineering. I applied to CU Boulder due to both its reputation as one of the top aerospace departments in the country and the abundance of mountains nearby! I work in the RECUV lab, and we fly small unmanned aircraft for severe storms research. Growing up in Miami, I originally wanted to work at the National Hurricane Center, so I'm happy to be combining my interest in severe weather with my love of engineering. As for a career later on, I would love to continue working with scientists studying severe weather; this would most likely involve working for NASA or NOAA. Like most other people in Boulder, I enjoy rock climbing, hiking, snowboarding (backcountry included) and road biking once the snow is gone. I hope I'm lucky enough to get a job in the area after graduation so I never have to leave!

## Carly Matson: Dept. of Mathematics



Carly Matson is going into her third year of the mathematics Ph.D. program at CU Boulder. She was an undergraduate at the University of Virginia and obtained majors in mathematics and cognitive science. Carly has loved recreational math since she was a child, delighting in themed books and competitions, but didn't discover the joys of modern mathematics until an abstract algebra course late in college. Carly also loves music, word games, and the absurd. She would love to contribute something of significance to the field of mathematics, but if not, convincing a few people that it isn't so dreadful would make her equally happy.

## Mark Pullins: Dept. of Mathematics



My name is Mark Pullins. I received my bachelor's degree in mathematics from Princeton University. When I was a teenager, I glimpsed the beauty of mathematics when a teacher proved a theorem using mathematical induction. After that, I decided I wanted to pursue a career in math. I'm currently interested in constraint-satisfaction problems and similar topics.

## Navid Shervani-Tabar: Dept. of Mechanical Engineering



Born in 1992 in Australia; He has got his high school diploma in Mathematics and Physics from Iran's National Organization for Development of Exceptional Talents (NODET). He earned his B.S. in mechanical Engineering from University of Tabriz, Iran. Currently, He is a student at Department of Mechanical engineering at University of Colorado Boulder, USA. His research interests include computational fluid dynamics and experimental study and visualization of cavitation. He is a keen hiker and a card-carrying mountain freak. He also enjoys pencil drawing very much.

# OPTICAL FREQUENCY COMBS FOR OPTICAL FREQUENCY METROLOGY

DANIEL COLE

**ABSTRACT.** The optical frequency comb is so far the most important development of the twenty-first century in the field of precision measurement. It enables determination of the frequencies of electromagnetic radiation in the optical range of the spectrum (spanning infrared, visible, and ultraviolet light) by converting these signals to electronically-measurable microwave frequencies. This allows measurement of frequency and time with unprecedented precision. Here, I introduce optical frequency combs and their use for the measurement of optical frequencies, and highlight some historical notes related to their development. I also highlight an outstanding problem in the field, which is the development of compact, fieldable optical frequency comb systems, and discuss one potential solution in the form of the microresonator frequency comb.

## 1. INTRODUCTION

The 2005 Nobel Prize in physics was awarded to the Max Planck Institute's Ted Haensch and CU's John Hall for the invention of the optical frequency comb [1, 2]. The optical frequency comb (OFC), a frequency-stabilized pulsed laser, solved a long-standing problem in the precise measurement of time and frequency by providing a way to convert electromagnetic radiation at optical frequencies (ranging from roughly 10 THz to 10 PHz, covering the infrared, visible, and ultraviolet portions of the spectrum) to microwave frequencies at hundreds of megahertz. Opening up this entirely new range of the electromagnetic spectrum to precision measurement had an impact on physics which is difficult to overstate: we are now able to measure time and frequency orders of magnitude more precisely than ever before, which has allowed us to establish quantum electrodynamics as the most rigorously tested theory in all of science. Further, we now have the necessary precision in our frequency measurements to determine whether our fundamental "constants" of nature (e.g. Planck's constant  $h$ ) are varying with time, as predicted by some extensions to the Standard Model of particle physics. On a more immediately practical note, optical frequency combs allow fast and precise broadband spectroscopy for reliable identification of trace gases [3], enable searches for extraterrestrial Earth-like planets [4], and can be leveraged to generate microwave signals with unprecedented stability for application in improved navigation and timing systems [5]. In the future, OFCs will enable increased information density in communications networks, easing some of the strain on these networks, which are rapidly saturating.

In this paper, I will introduce the problem of optical frequency measurement and discuss the revolutionary solution provided by optical frequency combs. I will explain

---

*Date:* August 8, 2015.

in detail what OFCs are and how they are produced, and give some historical notes on their development. I will discuss how optical frequencies are measured with an OFC without an external optical reference frequency, and I will conclude by discussing one avenue along which the field is continuing to develop. I aim for a conceptual explanation of the use of OFCs for optical frequency measurement and will necessarily omit some technical details, such as the methods of stabilization of a mode-locked laser and the details of experimental apparatus.

## 2. THE PROBLEM OF MEASURING OPTICAL FREQUENCIES

For the past 50 years or so, the precise measurement of time has been carried out with frequencies in the range of 100 MHz to 10 GHz. This is primarily because good mechanical and electronic oscillators and measurement systems have not been available at higher frequencies. This upper bound on our ability to electronically measure frequency is the reason that the SI second is defined in terms of the 9.193 GHz frequency of a particular electronic transition in the cesium atom, in spite of the fact that transitions at higher frequencies would provide better inherent stability. While electrical engineers are working hard to extend the upper limit of techniques for the direct electronic measurement of the frequency of electromagnetic radiation, presently this limit lies around one terahertz, hundreds of times below optical frequencies of interest. Thus, a physicist wishing to measure the frequency of an optical atomic transition at, say, 200 THz ( $2 \cdot 10^{14}$  cycles per second), must convert her frequency to the microwave domain in order to have an electronic readout of the result, all the while preserving the integrity of the signal. This conversion is done by generating a heterodyne beat at the difference frequency between an optical reference wave of known frequency and the frequency to be measured. A heterodyne beat results when signals at different frequencies are superimposed on the same square-law detector (whose output is proportional to the square of the input), according to the trigonometric identity  $\sin(\omega_1 t) \sin(\omega_2 t) = \frac{1}{2} \cos((\omega_1 - \omega_2)t) - \frac{1}{2} \cos((\omega_1 + \omega_2)t)$ . If the reference and the signal are sufficiently close in frequency, the resulting heterodyne beat at frequency  $\omega_1 - \omega_2$  is then amenable to electronic measurement.

The method of heterodyne beat is the basis of nearly all optical frequency measurements performed, and requires an optical reference frequency known to at least the precision desired of the measurement. Such references are hard to come by. Prior to 1999, they were generated only through the use of the optical frequency chain, which was a complicated system of iterated nonlinear frequency conversion. Constructing an optical frequency chain was a massive undertaking because of the number of steps involved and the complexity of these steps, and was only ever completed at a handful of national labs around the world (one of which was NBS, here in Boulder).

## 3. THE OPTICAL FREQUENCY COMB: A METROLOGICAL GAME-CHANGER

The contribution of the optical frequency comb, which has revolutionized optical frequency metrology and was recognized with the 2005 Nobel Prize in physics, is a new, far simpler way of generating the optical reference frequencies required for the heterodyne technique for optical frequency measurement.

One simple way of thinking about the optical frequency comb is to view it as a pulsed laser whose spectrum (the set of sine waves that make up its time-varying electric field) has been measured and stabilized. This is illustrated schematically in Fig. 1. A pulsed laser is commonly referred to as a “mode-locked” laser (MLL) because in the frequency domain, accessed by performing the Fourier transform on the electric field function  $E(t)$  describing the laser, the pulsed laser consists of an evenly spaced set of “modes” having a well-defined phase relationship (i.e. the modes are “locked” together). In particular, at some recurring time interval, the sine waves corresponding to these modes are simultaneously at a maximum, and they constructively interfere to give a pulse. The frequency with which these pulses occur is known as the repetition rate of the laser, denoted  $f_r$ , and is given by the spacing between the modes in the frequency domain. If this particular fixed phase relationship were replaced by a random one the laser output would remain periodic, but would not exhibit strong pulses.

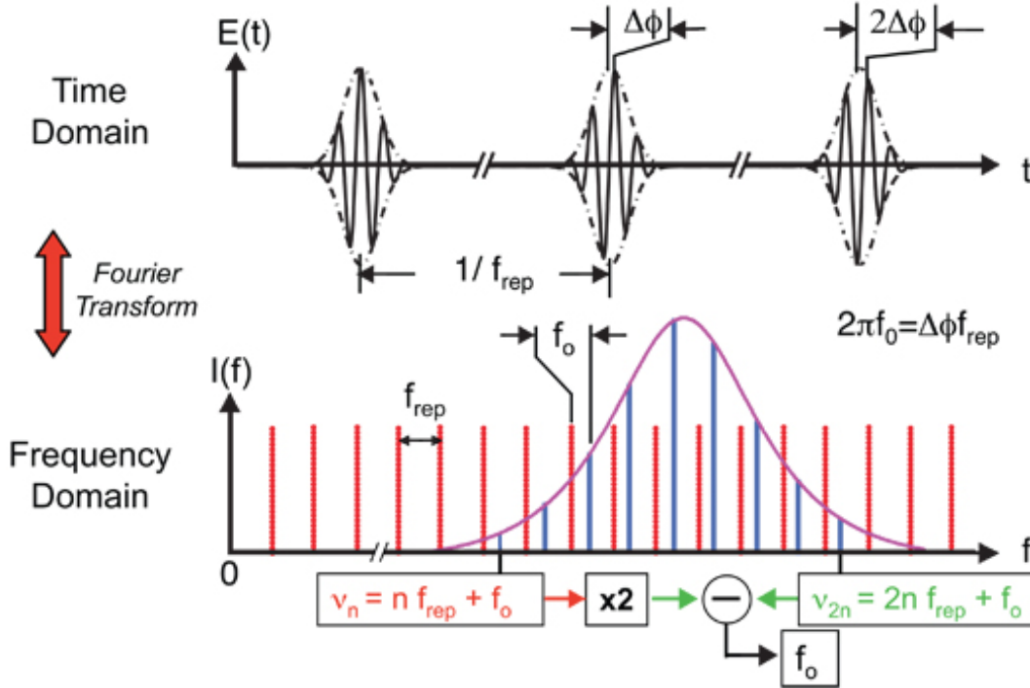
For a typical pulsed laser system it is actually only the intensity, or square modulus of the electric field  $E(t)$ , which is necessarily periodic in time. The electric field function itself consists of a periodic intensity envelope multiplying a sinusoidal carrier wave. This carrier wave can exhibit a pulse-to-pulse phase shift  $\Delta\phi$  with respect to the periodic intensity envelope, so that its maxima in time do not necessarily coincide with the maxima of the intensity envelope. The phase difference between the carrier and the envelope evolves at what is known as the carrier-envelope-offset (CEO) frequency, which is given by  $f_0 = f_r \times \frac{\Delta\phi}{2\pi}$  - this is the normalized pulse-to-pulse phase shift divided by the time over which the shift occurs, the repetition time  $T_r = \frac{1}{f_r}$ . This pulse-to-pulse phase shift occurs because the carrier wave propagates at the phase velocity of the medium, while the intensity envelope propagates at the group velocity of the medium, and the two are not the same in general.

The effect of this pulse-to-pulse phase shift in the frequency domain is to offset the modes of the comb by  $f_0$ , so that the frequency of mode number  $n$  is given by  $f_n = n f_r + f_0$ . It is worth pointing out that a typical frequency comb spans thousands of modes with very high mode number - e.g. in my lab we use a comb with a central frequency of 193 THz and a repetition rate of 250 MHz. The populated modes have indices near 770,000.

The primary characteristic of frequency combs which makes them useful for optical frequency metrology is that they consist of a set of precisely-known optical frequencies which are entirely determined by two microwave frequencies: the repetition rate  $f_r$  and the CEO frequency  $f_0$  (to completely specify the physical characteristics of the comb, one must also know the amplitude and phase of each of the comb’s modes, but precise knowledge of these quantities is unimportant for metrology). Because these microwave frequencies may be measured electronically, the OFC provides a method of “bootstrapping” oneself up from the microwave domain to the optical domain without an external optical reference frequency.

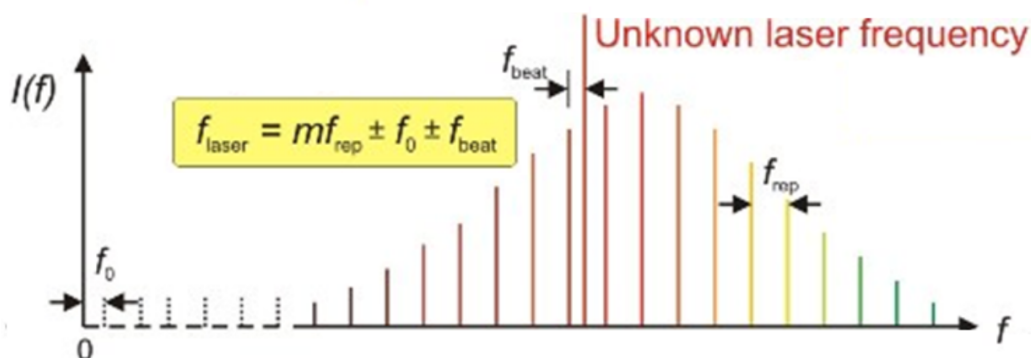
In practice, any mode-locked (pulsed) laser is described by a repetition rate and a CEO frequency, but these frequencies may vary in time in a noisy fashion. Turning a mode-locked laser into a frequency comb for metrology requires measuring these frequencies and stabilizing them. Once  $f_r$  and  $f_0$  are measured and stabilized, any unknown optical frequency falling within the bandwidth of the comb (determined by the

FIGURE 1. A schematic depiction of the temporal and spectral characteristics of a frequency comb. Viewed in the time domain, a frequency comb is a train of pulses spaced at  $\frac{1}{f_r}$ , with a carrier wave that may experience a phase change of  $\Delta\phi$  from pulse to pulse with respect to the intensity envelope. In the frequency domain, the frequency comb consists of the set of modes  $f_n = n f_r + f_0$  (shown as the blue lines), multiplied by an overall spectral envelope (shown in purple) which determines which modes are populated and shifts the center of mass of the spectrum to optical frequencies. Shown below the spectrum is a schematic illustration of the  $f - 2f$  self-referencing technique, wherein mode  $n$  is frequency doubled and beat against mode  $2n$ , yielding a heterodyne beat signal at the CEO frequency  $f_0$ . Figure courtesy of University of British Columbia.



spectral envelope, see Fig. 1) can be measured by beating it against the comb. In practice, this generates a series of heterodyne beat notes, as the unknown signal beats against each mode of the comb. The mode number corresponding to the lowest frequency beat note can typically be determined by making a much less precise diffraction-based wavelength measurement of the signal. The fact that the repetition rate (or spacing between the modes, in the frequency domain) is an electronically-accessible microwave frequency ensures that the lowest frequency beat note will also be electronically accessible. The heterodyne measurement technique with an OFC is shown in schematically in Fig. 2.

FIGURE 2. An illustration of the heterodyne technique for optical frequency measurements using an optical frequency comb. As indicated, the frequency of an unknown optical signal is given by  $mf_r \pm f_0 \pm f_{\text{beat}}$ . To determine the index of the mode participating in the heterodyne beat, a coarse wavelength measurement of the unknown signal can be made, or the change in  $f_{\text{beat}}$  with the change in  $f_r$  can be measured. To determine the signs of the  $f_0$  and  $f_{\text{beat}}$  terms,  $f_r$  and  $f_0$  may be adjusted by the experimenter. Figure - NPL, UK. . Figure courtesy of University of British Columbia.



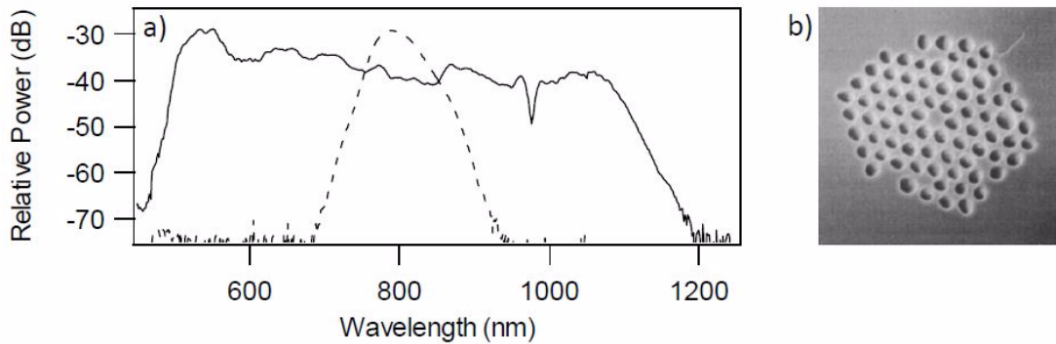
#### 4. FROM MODE-LOCKED LASER TO FREQUENCY COMB: THE MEASUREMENT AND STABILIZATION OF $f_r$ AND $f_0$

The potential to use mode-locked lasers for metrology in the fashion described above was apparent long before the successful generation of a frequency comb, and this potential was tantalizing to physicists working on precise measurements of time and frequency. The major obstacle to the use of MLLs in metrology was the difficulty in detecting the CEO offset frequency of a pulsed laser. The repetition rate corresponds to the rate of arrival of pulses in the laser's intensity at a photodetector, and can be easily measured. The CEO frequency, on the other hand, refers to the behavior of the carrier electric field which multiplies the pulsed intensity envelope, and is not easily measured by phase-insensitive electronic square-law detectors. Without knowledge of the comb's CEO frequency, a frequency comb offers no improvement in measurement resolution compared to a standard diffraction grating spectrometer. Once the repetition rate and CEO frequency are measured, they can be stabilized using techniques for laser control which were standard long before the development of the frequency comb, but these techniques are beyond the scope of this introduction.

The major innovation of Hall and Haensch and their teams was to measure the CEO frequency by accomplishing so-called  $f - 2f$  self-referencing for the first time. The idea is that, if one can obtain a MLL whose spectrum spans a full octave (a factor of two in frequency), then using standard methods of nonlinear optics, the low frequency light at one end of the spectrum can be frequency doubled and beat against the high frequency light on the other end of the spectrum. This generates a heterodyne beat at a

frequency equal to the carrier-envelope offset frequency of the pulsed laser, according to:  $2 \times f_n - f_{2n} = (2nf_r + 2f_0) - (2nf_r + f_0) = f_0$  (see Fig. 1).

FIGURE 3. a) A demonstration of extreme spectral broadening to transform a mode-locked laser’s output (dashed) to an octave-spanning supercontinuum, which enables self-referencing. Note that the spectral power is plotted in decibels [6]. b) Photonic crystal fiber, which enables supercontinuum generation by confining the propagating light extremely tightly to the fiber core, which is surrounded by air pockets in a honey-comb pattern [7].



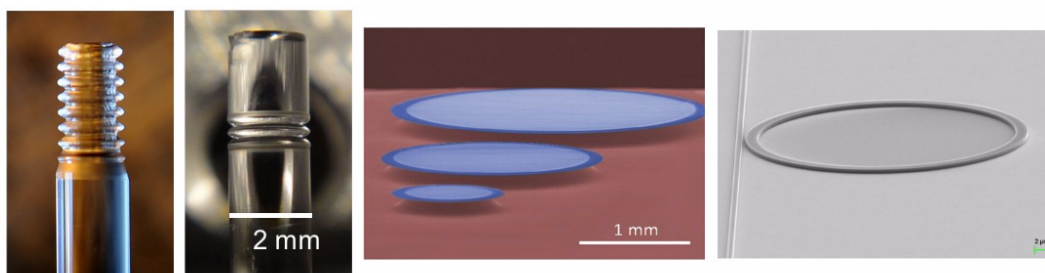
The challenge of  $f - 2f$  self-referencing lies in obtaining an octave-spanning spectrum. This requires extreme broadening of the spectrum generated by a typical pulsed laser, expanding the bandwidth by a factor of 20-50 or more, as shown in Fig. 3a [6]. Such a dramatic expansion of the spectrum was not possible before the development of photonic crystal fiber by Ranka and coworkers at Lucent in 1999 [7]. This development immediately preceded the generation of the first frequency combs by Hall and Haensch. In optics, the transfer of power from one frequency to another is typically accomplished by means of a nonlinear process which increases in efficiency at higher powers (i.e. described by a conversion coefficient like “100 percent per Watt,” valid for powers much lower than 1 Watt). Because of this power-dependent efficiency, the spectral broadening required to generate an octave-spanning spectrum is possible only for extremely high power densities (approximately  $100 \text{ GW/cm}^2$ ). Photonic crystal fiber, shown in Fig. 3b, confines light propagating in the fiber to an extremely small propagation area by having a small light-carrying core surrounded by air holes which have a significantly different refractive index. The small mode area leads to high power density, and if sufficient power is sent into the fiber, octave-spanning supercontinuum can be generated.

## 5. THE NEXT STEP: CHIP-COMPATIBLE FREQUENCY COMBS

Having been developed and used in metrology for the first time some 15 years ago, the optical frequency comb could be considered a mature research technology. Combs were initially generated by stabilizing the spectra of pulsed titanium:sapphire lasers,

but are now generated in a myriad of gain media and platforms, with both free-space and fiber-based laser cavities. Combs spanning frequencies across much of the optical domain are available in some form or another, through either native comb generation or frequency conversion with e.g. optical parametric oscillation, difference frequency generation, or high harmonic generation. However, all of these technologies remain research-scale - a stabilized, self-referenced optical frequency comb usually occupies one or more optical tables in a lab. A remaining challenge is the creation of much smaller, robust platforms for comb generation which would allow the use of combs in settings outside the lab, so that they could improve GPS navigation and timing and be integrated into optical communications systems, for example.

FIGURE 4. Microresonators used at NIST for generation of optical frequency combs through cascaded four-wave mixing. Left to right: silica microrods generated by laser machining (two panels), silica disks fabricated by our collaborators in Kerry Vahala’s group at Caltech, and a silicon nitride microring fabricated by Kartik Srinivasan’s group at NIST Gaithersburg. A waveguide for coupling light into and out of the resonator is also visible in the right panel. Alternatively, a tapered optical fiber may be used in the same configuration.



In my group at NIST Boulder and in several other groups around the world, optical frequency comb generation in microresonators is being investigated as a promising avenue towards a chip-compatible comb platform [8]. A microresonator is a generic term for a small resonant cavity which supports “whispering gallery modes,” spatial modes of light propagation where waves are formed around the circumference of the cavity. Some microresonators used for comb generation are shown in Fig. 4. These microresonators may be constructed from a wide variety of materials (e.g. crystalline  $\text{MgF}_2$  and amorphous silica), and are typically hundreds of microns to several millimeters in diameter. In MLL frequency combs, the pulsed laser is generated by lasing of the gain medium across many frequency modes, combined with some mechanism which enforces the mode-locking behavior (typically a “saturable absorber,” which leads to lower loss in the laser cavity for higher intensity, shorter pulses). In contrast, frequency comb generation in microresonators occurs by cascaded four-wave mixing, a nonlinear process whereby two input photons are combined to generate two output photons at different frequencies, conserving energy in the process. To generate a microresonator frequency comb, a continuous wave laser, called the pump and consisting of a single frequency, is

sent into the resonator, where degenerate four-wave mixing converts two pump photons into one photon at a higher frequency and one photon at a lower frequency. Energy is conserved according to the equation  $f_p + f_p = (f_p + \Delta f) + (f_p - \Delta f) = f_n + f_{-n}$  (recall that the energy of a photon is  $hf$ ). Here the mode number  $n$  is expressed relative to the pump. Once the comb generation is started by degenerate four-wave mixing of pump photons, non-degenerate four-wave mixing (where the two input photons are not of the same frequency) can expand the comb.

Microresonator frequency combs bring a different set of challenges from those of MLL combs. Because of their small size and short cavity round-trip times, their repetition rates are sufficiently high (10 – 1000 GHz) that specialized photodetectors are required to measure the rate of arrival of pulses, raising technical requirements for their eventual implementation. Secondly, there is no mode-locking mechanism in microresonator frequency combs, and so while pulsed operation can be achieved, it is not guaranteed. This can make working with these combs less deterministic, and turn-key operation is as yet a long way off. Chip-compatible turn-key microresonator frequency combs are, however, the ultimate goal, and would enable integration of OFC measurement of optical frequencies into a wide array of technologies outside the lab, continuing the revolution of the optical frequency comb that has already brought us the ability to measure time, frequency, and nature’s fundamental constants to levels that were unimaginable thirty years ago.

## 6. ACKNOWLEDGEMENTS

Thanks to Trubee Davison for organizing the STEMinar, and the CU Graduate School for its support of the program. My work at NIST is supported by the NSF Graduate Research Fellowship program and my advisors Scott Diddams and Scott Papp.

## REFERENCES

- [1] John L. Hall, “Nobel Lecture: Defining and measuring optical frequencies,” *Reviews of Modern Physics* 78, 1279 (2006).
- [2] Theodor W. Haensch, “Nobel Lecture: Passion for precision,” *Reviews of Modern Physics* 78, 1297 (2006).
- [3] Scott A. Diddams, Leo Hollberg, and Vela Mbele, “Molecular fingerprinting with the resolved modes of a femtosecond laser frequency comb,” *Nature* 445, 627 (2007).
- [4] Tilo Steinmetz et al., “Laser Frequency Combs for Astronomical Observations,” *Science* 321, 1335 (2008).
- [5] Tara M. Fortier et al., “Generation of ultrastable microwaves via optical frequency division,” *Nature Photonics* 5, 425 (2011).
- [6] Scott A. Diddams et al., “Direct Link between Microwave and Optical Frequencies with a 300 THz Femtosecond Laser Comb,” *Physical Review Letters* 84, 5102 (2000).
- [7] Jinendra K. Ranka, Robert S. Windeler, and Andrew J. Stentz, “Visible continuum generation in air-silica microstructure optical fibers with anomalous dispersion at 800 nm,” *Optics Letters* 25, 25 (2000).
- [8] T. J. Kippenberg, R. Holzwarth, and S. A. Diddams, “Microresonator-Based Optical Frequency Combs,” *Science* 332, 6029 (2011).

7. FURTHER READING

- (1) Scott A. Diddams, “The evolving optical frequency comb,” JOSA B 27, B51 (2010).
- (2) Th. Udem, R. Holzwarth, and T. W. Haensch, “Optical frequency metrology,” Nature 416, 233 (2002).
- (3) Steven T. Cundiff and Jun Ye, “Colloquium: Femtosecond optical frequency combs,” Reviews of Modern Physics 75, 325 (2003)

*E-mail address:* Daniel.C.Cole@colorado.edu

DEPARTMENT OF PHYSICS, UNIVERSITY OF COLORADO, BOULDER, COLORADO

# DYNAMIC HOMOGENIZATION OF DAMPED PERIODIC MATERIALS

MICHAEL J. FRAZIER

**ABSTRACT.** We consider the dynamics of wave propagation in a dissipative periodic elastic composite. Using a modified form of Bloch's theorem that permits temporal attenuation, we construct the damped frequency band structure and the associated damping ratio band structure. We submit the periodic Bloch field variables to a homogenization scheme proposed by [15] for periodically layered composites, which yields frequency-dependent effective material parameters. These are a macro-scale interpretation of the microstructure dynamics. By necessity, the effective properties, reconstruct the band structure of the original composite. As dissipation effects the band structure, its influence extends to the effective parameters. Although the impact of dissipation on the effective properties has been investigated in other articles, our interpretation of damped Bloch wave propagation is the first to manifest a frequency-dependent effective damping constant. The presence of an effective damping constant, in addition to the effective density and compliance, completes the set of parameters describing a lossy material.

## 1. INTRODUCTION

Often, the aim of composite design is the realization of effective properties (i.e., effective density and effective compliance) unavailable from the constituent. In the static case, taking into account the constituent material filling ratios, the determination of effective properties can be quite straightforward. In the dynamic case, relative motion among the constituent material phases complicates the evaluation. While adherence to Newton's second law of motion is absolute at the length scale of the microstructure, relative motion beyond the resolution of a traveling wave is undetectable, giving the illusion that the classical equation of motion for a continuum fails. The apparent violation at the macro-scale can be rectified by the substitution of a dynamic effective density and compliance for the static versions. In short, for the dynamic case, especially when a high degree of mechanical mismatch exists between the constituent phases, some dynamic homogenization procedure is necessary. At this point, we offer a brief, non-exhaustive history of dynamic homogenization.

Early attempts at dynamic homogenization considered the low-frequency, quasi-static limit in which it is revealed that the effective parameters are nonlocal in space (wavenumber dependent) [1]. References [20] and [6], with the aid of energy methods, sought to place bounds on the elastic properties of randomly inhomogeneous composites. Earlier Ref. [2] asserted that the dynamic effective density could differ from the static version even in the low-frequency limit. However, due to a lack of experimental reinforcement and other criticisms, little credence was given to Berryman's proposal until

---

*Date:* August 8, 2015.

*Key words and phrases.* homogenization, dissipation, periodic elastic composites, Bloch wave propagation.

further theoretical and experimental support were presented by Ref. [12] and by Ref. [4], respectively. In general, the dynamic effective properties of a homogenized medium are nonlocal in space and time. For the general dynamic case, [21] rigorously demonstrated a revised constitutive model in which stress is not only coupled strain but also the material velocity, and the momentum density is not only related to the material velocity but the strain as well. The elegance of the Willis constitutive model, however, does not easily lend itself to the determination of the effective material parameters at finite frequencies. In one dimension, Ref. [18] addressed this by employing a Magnus series expansion of a Floquet wavenumber matrix. Using the plane wave expansion method, Ref. [17] extended the analytic determination of effective material properties to three dimensions. In addition, several numerical techniques were developed for one-dimensional [15, 16] and three-dimensional periodic composites [19]. Other techniques expedite classical band structure calculations [7, 14].

In recent years, periodic elastic composites have garnered the attention of the scientific and engineering community. Whether due to Bragg scattering [10] or local resonances [11], the dispersive nature of periodic materials can be exploited as a passive form of vibration control. Certain extraordinary applications such as sub-wavelength acoustic imaging [23] and acoustic cloaking [5] are also the focus of many ambitious investigations. References [11] and [13] have shown that composites with certain internal components may acquire negative or anisotropic effective properties. Reference [16] demonstrated simultaneously negative dynamic effective density and compliance due to local resonance. These same properties assumed complex values with the incorporation of dissipative effects, introduced as an additional imaginary component of the elastic modulus.

Absent dissipation effects, an elastic wave traveling through a homogeneous medium faces no obstacles and propagates, theoretically, indifferent to space and time. In contrast, a wave propagating through a heterogeneous medium surrenders its energy to a variety of mechanisms: scattering at material interfaces, absorption by resonating bodies, etc. Ultimately, these interactions exact a cost and the wave decays with distance. In the context of Bloch's theorem, modeling this behavior requires the spatial constant to become complex. An inherent material property, dissipation acts over time to consume the energy of a traveling wave, changing its frequency in the process. In the context of Bloch's theorem, modeling the physics this behavior requires the temporal constant to adopt a complex value; however, by convention, many research articles lose the temporal attenuation aspect of dissipation by maintaining an imaginary temporal constant. Guided by this principle of temporal dissipation, this article investigates the impact of viscous dissipation on the frequency band structure and the effective properties of a periodic elastic composite.

## 2. THEORY

**2.1. Homogenization for a 1D Phononic Crystal.** The homogenization method presented here is adapted from that of [15], which is inspired by [22], to incorporate a viscous dissipation constant. Based on a spatial averaging of the periodic portion of the field variables, the dynamic effective properties are determined by relating the homogenized constitutive equations and the temporal attenuation component of the Bloch

solution. To begin the presentation of the homogenization procedure, we introduce the relevant field variables for generalized Bloch wave propagation in a one-dimensional, layered phononic crystal:

$$u(x, t) = U(x)e^{i\kappa x + \lambda t}, \quad (2.1)$$

$$\varepsilon(x, t) = u_x(x, t) = \mathcal{E}(x)e^{i\kappa x + \lambda t}, \quad (2.2)$$

$$\dot{\varepsilon}(x, t) = u_{x,t}(x, t) = \lambda \mathcal{E}(x)e^{i\kappa x + \lambda t}, \quad (2.3)$$

$$\sigma(x, t) = [E(x)\mathcal{E}(x) + \lambda\eta(x)\mathcal{E}(x)]e^{i\kappa x + \lambda t} = \Sigma(x)e^{i\kappa x + \lambda t}, \quad (2.4)$$

$$v(x, t) = u_t(x, t) = V(x)e^{i\kappa x + \lambda t}, \quad (2.5)$$

and

$$p(x, t) = \rho(x)v(x, t) = \rho(x)V(x)e^{i\kappa x + \lambda t} = P(x)e^{i\kappa x + \lambda t}, \quad (2.6)$$

where equations (2.1) through (2.6) are the displacement, strain, strain-rate, stress, velocity, and momentum, respectively. The periodic functions  $U(x)$ ,  $\mathcal{E}(x)$ ,  $\Sigma(x)$ ,  $V(x)$ , and  $P(x)$  have the periodicity of the unit cell. In the exponent,  $\kappa$  is the wavenumber and  $\lambda$  is a complex parameter, the components of which, following Hussein (2009), account for wave propagation with temporal attenuation. The position and time are represented by the variables  $x$  and  $t$ , accordingly, and  $i = \sqrt{-1}$ . Finally, we denote the material density,  $\rho(x)$ , Young's modulus,  $E(x)$ , and viscous dissipation constant,  $\eta(x)$ .

Turning to the method proper, we assume  $x$  to be fixed at some arbitrary position in the periodic medium and multiply the previous equations by  $e^{i\kappa\mathcal{X}}$ . Introducing the change in variables,  $y = x - \mathcal{X}$ , transforms equations (2.2) and (2.4) through (2.6) as follows:

$$\varepsilon(\mathcal{X} + y, t) = \mathcal{E}(\mathcal{X} + y)e^{i\kappa y + \lambda t}, \quad (2.7)$$

$$\sigma(\mathcal{X} + y, t) = \Sigma(\mathcal{X} + y)e^{i\kappa y + \lambda t}, \quad (2.8)$$

$$v(\mathcal{X} + y, t) = V(\mathcal{X} + y)e^{i\kappa y + \lambda t}, \quad (2.9)$$

and

$$p(\mathcal{X} + y, t) = P(\mathcal{X} + y)e^{i\kappa y + \lambda t}, \quad (2.10)$$

The familiar constitutive relations are thus:

$$\Sigma(\mathcal{X} + y) = [E(\mathcal{X} + y) + \lambda\eta(\mathcal{X} + y)]\mathcal{E}(\mathcal{X} + y), \quad (2.11)$$

and

$$P(\mathcal{X} + y) = \rho(x)V(\mathcal{X} + y). \quad (2.12)$$

To arrive at the homogenized medium, each of the field variables is averaged over the unit cell dimension,  $a$ , thus defining the domain  $\Omega = \{\mathcal{X} : -a/2 \leq \mathcal{X} \leq a/2\}$ . Now, with non-spatial and effective material properties, the mean constitutive relations hold.

$$\bar{\Sigma} = (E_{\text{eff}} + \lambda\eta_{\text{eff}})\bar{\mathcal{E}} \quad (2.13)$$

$$\bar{P} = \rho_{\text{eff}}\bar{V} \quad (2.14)$$

Each of the barred field variables are computed using the following average value integral:

$$\bar{A} = \frac{1}{a} \int_{-a/2}^{a/2} A(\mathcal{X})d\mathcal{X}, \quad (2.15)$$

where  $A(\mathcal{X})$  represents any one of the periodic functions of the field variables. It is worth noting that real-valued effective parameters emerge if the average is calculated

over a symmetric unit cell as coupling among the field variables yields complex effective parameters if the unit cell is not symmetric. To determine the corresponding effective material properties requires an additional relation to tie (2.13) to (2.14). Based on work by Ref. [3], we expect the dissipative, homogenized unit cell to adhere to the following result for the complex parameter:

$$\lambda(\kappa) = -\frac{\eta_{\text{eff}}\kappa^2}{2\rho_{\text{eff}}} \pm i\kappa\sqrt{\frac{E_{\text{eff}}}{\rho_{\text{eff}}} - \left(\frac{\eta_{\text{eff}}\kappa}{2\rho_{\text{eff}}}\right)^2} = -\xi(\kappa)\omega(\kappa) \pm i\omega_{\text{d}}(\kappa), \quad (2.16)$$

where the damped frequency dispersion and associated damping ratio dispersion relations are  $\omega_{\text{d}}(\kappa)$  and  $\xi(\kappa)$ , respectively. From equation (2.16), we extract a third linear equation.

$$-2\text{Re}[\lambda]\rho_{\text{eff}} = \kappa^2\eta_{\text{eff}} \quad (2.17)$$

With equations (2.13), (2.14), and (2.17), we easily formulate the effective dynamic properties.

$$\rho_{\text{eff}} = \frac{\bar{P}}{\bar{V}} \quad (2.18)$$

$$\eta_{\text{eff}} = -\frac{2\text{Re}[\lambda]}{\kappa^2}\rho_{\text{eff}} \quad (2.19)$$

$$E_{\text{eff}} = \frac{\bar{\Sigma}}{\bar{\mathcal{E}}} - \lambda\eta \quad (2.20)$$

It is important to note that the use of equation (2.17) restricts the validity of equations (2.18) through (2.20) to cases of critical damping and lesser scenarios.

**2.2. Finite Element Implementation.** The finite element method provides one of many possible avenues for the discretization of the continuous domain of our one-dimensional, layered phononic crystal. What follows is a brief summary of its application to the problem at hand.

Interpreted as an assemblage of rod elements, the continuous domain,  $\Omega$ , of the phononic crystal is divided into a number,  $n$ , of sub-domains (elements),  $\Omega^e$ , at layer boundaries and within the layers themselves. That is,  $\Omega = \cup_{e=1}^n \Omega^e$ , where  $n$  is an indication of the degree of discretization. The discretization of the material properties and the displacement field follows accordingly. For an arbitrary element,  $u^e(x)$  is approximated by a linear interpolation of discrete end displacements (node displacements) contained in the vector  $\mathbf{u}^e$ . That is,  $u^e(x) = \mathbf{N}(x)\mathbf{u}^e$  ( $x \in \Omega^e$ ), where  $\mathbf{N}(x)$  is a vector of interpolating functions. Upon discretization, the application of the Euler-Lagrange equations with Rayleigh's dissipation function, and the incorporation of periodic boundary conditions, the following algebraic eigenvalue problem emerges:

$$[\lambda^2\mathbf{M} + \lambda\mathbf{C}(\kappa) + \mathbf{K}(\kappa)]\mathbf{u} = \mathbf{0}, \quad (2.21)$$

where the displacement vector  $\mathbf{u}$  organizes the total node displacements.

The variables  $\mathbf{M}$ ,  $\mathbf{C}(\kappa)$ , and  $\mathbf{K}(\kappa)$ , representing the mass, damping, and stiffness matrices, respectively, are assembled from the corresponding element level sub-matrices  $\mathbf{M}^e$ ,  $\mathbf{C}^e(\kappa)$ , and  $\mathbf{K}^e(\kappa)$  and are consistent with the displacement vector. To compute

the sub-matrices, consider the element equations of motion from the perspective of the Euler-Lagrange equations:

$$\frac{d}{dt} \left( \frac{\partial T^e}{\partial \dot{\mathbf{u}}^e} \right) - \frac{\partial T^e}{\partial \mathbf{u}^e} + \frac{\partial V^e}{\partial \mathbf{u}^e} + \frac{\partial R^e}{\partial \dot{\mathbf{u}}^e} = 0, \quad (2.22)$$

where  $T^e$  is the kinetic energy,  $V^e$  is the internal energy, and  $R^e$  is Rayleigh's dissipation function. For an arbitrary rod element with cross-sectional area  $A^e$  and material properties,  $\rho^e$ ,  $E^e$ , and  $\eta^e$ , the kinetic energy is given by equation (2.23).

$$T^e = \frac{1}{2} \rho^e A^e \int_{\Omega^e} [V^e(x)]^2 dx = \frac{1}{2} \rho^e A^e \dot{\mathbf{u}}^e \int_{\Omega^e} [\mathbf{N}(x)]^T \mathbf{N}(x) dx \dot{\mathbf{u}}^e \doteq \frac{1}{2} (\dot{\mathbf{u}}^e)^T \mathbf{M}^e \dot{\mathbf{u}}^e \quad (2.23)$$

Therefore,

$$\mathbf{M}^e = \rho^e A^e \int_{\Omega^e} [\mathbf{N}(x)]^T \mathbf{N}(x) dx. \quad (2.24)$$

The remaining element-level sub-matrices,  $\mathbf{K}^e$  and  $\mathbf{C}^e$ , readily emerge from  $V^e$  and  $R^e$ , respectively. Equation (2.25) measures the energy of deformation, the internal energy:

$$V^e = \frac{1}{2} E^e A^e \int_{\Omega^e} [\mathcal{E}^e(x)]^2 dx = \frac{1}{2} E^e A^e \mathbf{u}^e \int_{\Omega^e} [\mathbf{B} + i\kappa \mathbf{N}(x)]^T [\mathbf{B} + i\kappa \mathbf{N}(x)] dx \mathbf{u}^e \doteq \frac{1}{2} (\mathbf{u}^e)^T \mathbf{K}^e \mathbf{u}^e, \quad (2.25)$$

where  $\mathbf{B} = \mathbf{N}_x(x)$ . Thus, the element stiffness matrix follows:

$$\mathbf{K}^e(\kappa) = E^e A^e \int_{\Omega^e} [\mathbf{B} + i\kappa \mathbf{N}(x)]^T [\mathbf{B} + i\kappa \mathbf{N}(x)] dx. \quad (2.26)$$

Rayleigh's dissipation function represents half the rate at which energy is lost in the process of deformation.

$$R^e = \frac{1}{2} \eta^e A^e \int_{\Omega^e} [\lambda \mathcal{E}^e(x)]^2 dx = \frac{1}{2} \eta^e A^e \dot{\mathbf{u}}^e \int_{\Omega^e} [\mathbf{B} + i\kappa \mathbf{N}(x)]^T [\mathbf{B} + i\kappa \mathbf{N}(x)] dx \dot{\mathbf{u}}^e \doteq \frac{1}{2} (\dot{\mathbf{u}}^e)^T \mathbf{C}^e \dot{\mathbf{u}}^e \quad (2.27)$$

While the internal energy depends upon the strain, dissipation arises from the strain-rate. Consequently, the element damping matrix extracted from equation (2.27) exhibits a similar formulation to the element stiffness matrix.

$$\mathbf{C}^e(\kappa) = \eta^e A^e \int_{\Omega^e} [\mathbf{B} + i\kappa \mathbf{N}(x)]^T [\mathbf{B} + i\kappa \mathbf{N}(x)] dx \quad (2.28)$$

### 3. RESULTS AND DISCUSSION

The aim of this article is to illuminate the characteristics of viscous dissipation on the dynamics of heterogeneous periodic media. To this end, for simplicity of exposition, a 1D phononic crystal in the form of the bi-material rod illustrated in Fig. 1 will serve as our material model. With the spatial periodicity denoted by  $a$ , the symmetric unit cell is enclosed by a red, dashed box to ensure real-valued effective dynamic material properties in the absence of dissipation. For non-symmetric unit cells, coupling among the field variables manifests as complex-valued effective properties.

In Fig. 1, the extent  $\ell$  of each constituent material is the same; however, the individual material properties contrast in the extreme manner characteristic of phononic crystals. In the numerical case studies to follow, the density and elasticity of each constituent material remains constant while the dissipation constant is manipulated to demonstrate

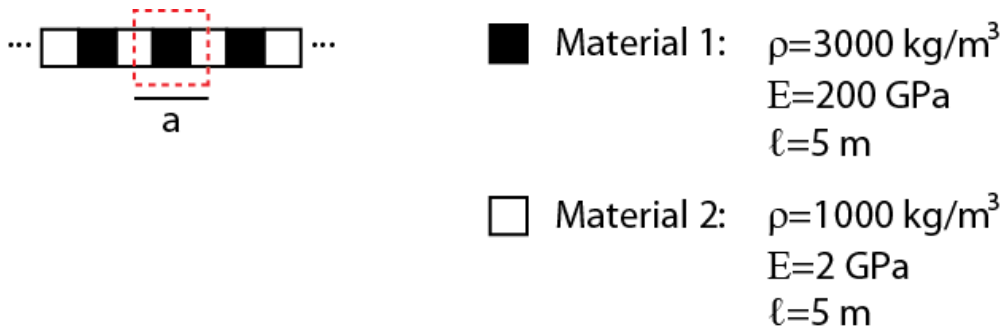


FIGURE 1. Continuous model of a multi-phased 1D phononic crystal with lattice spacing  $a$ .

aspects of damping in phononic crystals. Although the dissipation constant of each constituent material may assume any positive value, we adopt the definition  $\eta = qE$ , where  $q$  is a parameter used to scale the level of dissipation. By numerically tying the dissipation constant to the elasticity, we promote a type of damping, first proposed by Rayleigh, in which the damping matrix is proportional to the stiffness matrix,  $\mathbf{C}(\kappa) = q\mathbf{K}(\kappa)$ . With the damping matrix defined in this way, we may take advantage of the computationally efficient Bloch modal analysis [8] to determine the complex parameter  $\lambda(\kappa; q)$  from which the damped dispersion relations are constructed.

Figure 2 shows the dispersion curves corresponding to our model phononic crystal and illustrates the effects dissipation over a range of damping intensities. As a consequence of using the generalized form of Bloch theory, the familiar frequency dispersion diagram is complemented by one featuring the damping ratio dispersion curves, which relate temporal attenuation. Spatial attenuation is evident in the gaps between frequency dispersion bands representing frequencies for which no propagating mode exists. Although the continuous phononic crystal contains an infinite number of dispersion curves, the finite element method and the standard eigenvalue problem limits the number that can be determined to the number of independent degrees of freedom in the finite element model. However, regardless of the level of discretization, for clarity of exposition, we limit our presentation and discussion to that pertaining to only the first two propagating frequency branches: the acoustic (solid) and the optical (dashed).

By inspecting the dispersion diagrams in Fig. 2, it is immediately evident that dissipation maintains a greater influence over the optical branch (indeed, dissipation's influence increases with branch number) than over the acoustic. While the acoustic branch remains relatively unperturbed in response to elevated levels of damping intensity, the optical branch rapidly descends the frequency range, shrinking the band gap. This behavior is supported by the corresponding damping ratio diagram and is expected based on the results in Refs. [8] and [9]. This behavior also provokes some interesting dynamic phenomena. Given a sufficient level of damping intensity, the first of the phenomena to occur is the change in concavity seen in the optical branch, leading to the perceived reversal of the group velocity (energy velocity). The second dynamic phenomenon to occur with adequate damping readily reveals itself in either the frequency or the damping ratio diagram. In an analogy with finite vibration analysis, the attainment of unity by a curve in the damping ratio diagram necessitates the cessation of

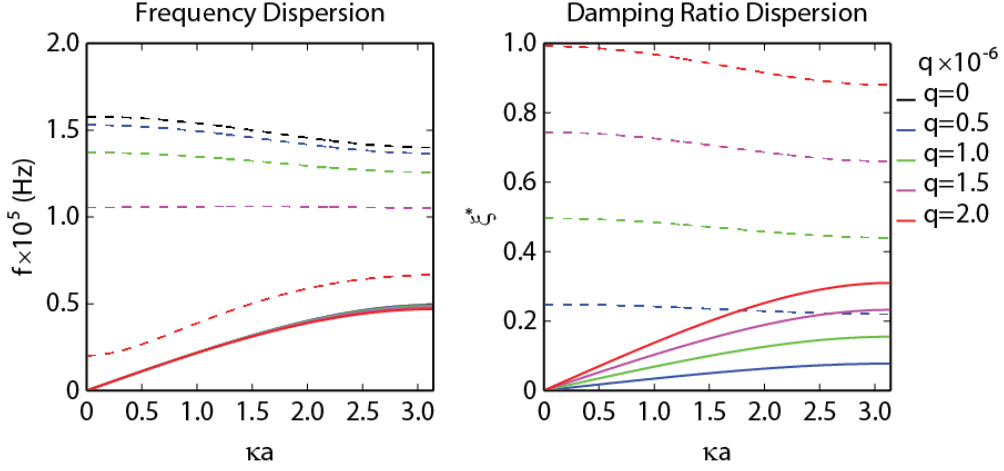


FIGURE 2. Frequency and damping ratio dispersion.

wave propagation as any oscillatory motion is forbidden. In the damping ratio diagram, the curve corresponding to the optical branch at  $q = 2.0$  makes the closest approach to unity. With the appropriate increase in value of  $q$  (not shown),  $\xi^* \geq 1$  over a portion of the irreducible Brillouin zone (IBZ) resulting in optical branch cut-off, incomplete wavenumber coverage for the optical branch. The optical branch entirely vanishes from the diagram  $\xi^* \geq 1$  over the totality of the IBZ.

Given their frequency dependence, the influence of dissipation extends beyond the frequency band structure to impact the effective parameters. Figure 3 below displays the effective dynamic material properties for our representative damped phononic crystal. Within each panel of Fig. 3, the format of the curves follows that of Fig. 2; the solid and dashed curves represent the acoustic and optical modes, respectively. Regarding the non-propagating modes of the band gap, the effective properties are consistent with the tenet of wave propagation,  $(\omega_d/\kappa)^2 = E/\rho - (\eta\kappa/2\rho)^2$ , as either the effective density or the effective compliance becomes negative in this region. Reference [16] found that dissipation bore imaginary components to the dynamic effective parameters; however, our generalized Bloch formulation yields no such artifacts. By separating the damping constant from the elasticity and interpreting it as an independent, real-value parameter, for the first time to the best of our knowledge, dissipation has led the dynamic effective density and dynamic effective compliance to be joined by a dynamic effective dissipation constant (the dynamic effective viscosity, in our case).

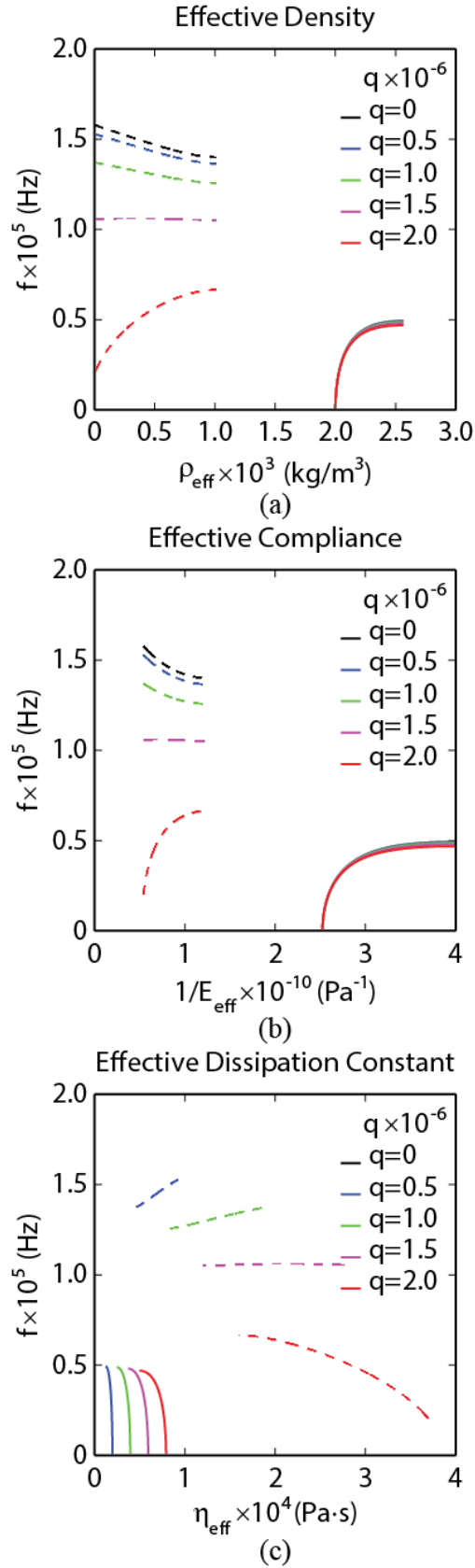


FIGURE 3. Dynamic effective material properties.

In the low-frequency limit, a single wavelength encloses many unit cells, hence losing its ability to resolve the inhomogeneity of the phononic crystal. In Fig. 2, this phenomenon manifests itself in the near linear relationship between frequency and wavenumber as the propagating wave observes the static effective parameters (the volume average of the unit cell constituent materials). The results displayed in Fig. 3 provide one level of confidence in the homogenization procedure presented in the previous section. In the low-frequency limit, when the response of the phononic crystal is nearly static, each of the effective parameters in Fig. 3 is nearly constant and equal to the relevant effective static parameter irrespective of the dissipation. Beyond the low-frequency limit, the kinetics of the sub-wavelength constituents of the phononic crystal appreciably effect the bulk dynamics, and a generalization of Newtonian's laws causes the dynamic effective properties to diverge from the static ones.

Expectedly, the application of damping affects the band structures of the effective properties in a manner reminiscent of the frequency band diagram of Fig. 2—even instigating a change in concavity in the branch corresponding to the optical mode. Naturally, the effective dissipation constant vanishes when the phononic crystal is absent dissipative influence. In addition, while the dynamic effective density and compliance always return to the same effective static values in the long wavelength limit regardless of damping, the dynamic effective dissipation constant returns to different effective static values as the level of damping changes. Moreover, due to our specific Rayleigh damping model,  $\eta_{\text{eff}} = qE_{\text{eff}}$ .

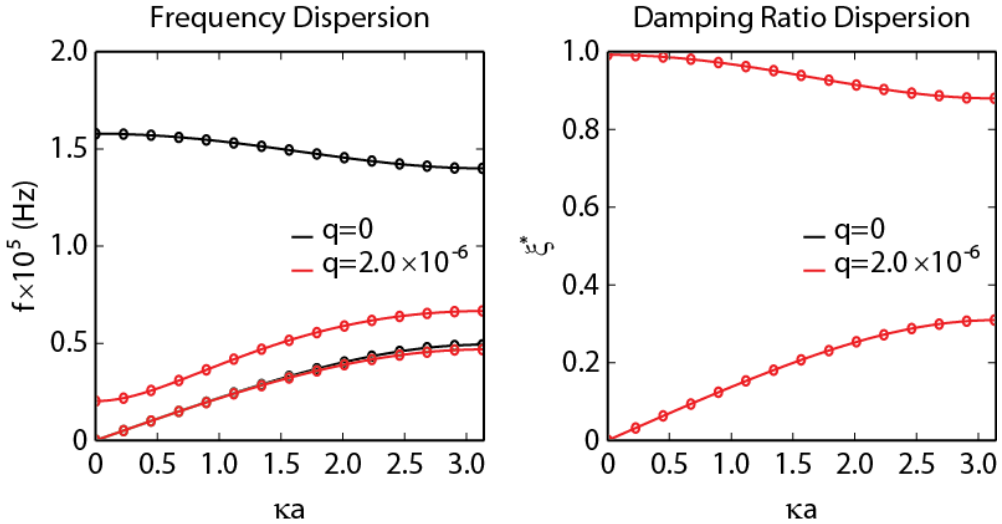


FIGURE 4. Reconstruction of frequency and damping ratio dispersion: (—) Finite Element Solution, (○) Effective Parameter Reconstruction.

As a final testament to the homogenization procedure of the previous section, we substitute the effective parameters corresponding to  $q = 2.0 \times 10^{-6}$  into equation (2.16) and reconstruct the frequency and damping ratio dispersion curves. Figure 4 compares the finite element solution with effective parameter reconstruction.

## 4. CONCLUSION

In this work, we demonstrated the consequences of dissipation on the dynamic effective properties of a viscously damped periodic material. To this end, we used a homogenization scheme proposed by Ref. [15] along with insights from Ref. [3] to define the effective parameters in terms of the averaged field variables and the dispersion characteristics of our model phononic crystal. The calculated dynamic effective properties approached the appropriate static values in the low-frequency limit and were able to reconstruct the damped dispersion relations, providing a level of credibility to the results. To the best of our knowledge, this is the first time a frequency-dependent effective damping parameter has been determined. The incorporation of damping is necessary as dissipation is an inherent and potentially functional property of actual materials that future applications of periodic composites may employ. While this paper employs Bloch modal analysis to consider a Rayleigh-type dissipation model, Bloch state-space analysis may be applied to a general dissipation model. In addition, we acknowledge that nonviscous dissipation could reveal heretofore unrealized results.

## 5. ACKNOWLEDGEMENTS

This material is based upon work supported by the National Science Foundation Graduate Research Fellowship under Grant No. DGE 1144083.

## REFERENCES

- [1] M. J. Beran and J. J. McCoy, "Mean field variation in random media," *Quarterly Appl. Math.* **28**, 245–258 (1970).
- [2] J. G. Berryman, "Long-wavelength propagation in composite elastic media I. Spherical inclusions," *J. Acoust. Soc. Am.* **680**, 1809–1819 (1980).
- [3] W. G. Cady, "Theory of longitudinal vibrations in viscous rods," *Phys. Rev.* **19**, 1–6 (1922).
- [4] F. Cervera, L. Sanchis, J. V. Sánchez-Pérez, R. Martínez-Sala, C. Rubio, F. Meseguer, C. López, D. Caballero, and J. Sánchez-Dehesa, "Refractive acoustic devices for airborne sound," *Phys. Rev. Lett.* **88**, 023902 (2002).
- [5] S. A. Cummer, B. Popa, D. Schurig, D. R. Smith, J. Pendry, M. Rahm, and A. Starr, "Scattering theory derivation of a 3D acoustic cloaking shell," *Phys. Rev. Lett.* **100**, 024301 (2008).
- [6] G. Diener, A. Hürrich and J. Weissbarth, "Bounds on the nonlocal effective elastic properties of composites," *J. Mech. Phys. Solids* **32**, 21–39 (1984).
- [7] M. I. Hussein and G. M. Hulbert, "Mode-enriched dispersion models of periodic materials within a multiscale mixed finite element framework," *Finite Elem. Anal. Des.* **42**, 602–612 (2006).
- [8] M. I. Hussein, "Theory of damped Bloch waves in elastic media," *Phys. Rev. B* **80**, 212301 (2009).
- [9] M. I. Hussein, and M. J. Frazier, "Band structure of phononic crystals with general damping," *J. Appl. Phys.* **108**, 093506 (2010).
- [10] M. S. Kushwaha, P. Halevi, L. Dobrzynski, and B. Djafari-Rouhani, "Acoustic band structure of periodic elastic composites," *Phys. Rev. Lett.* **71**, 2022–2025 (1993).
- [11] Z. Liu, X. Zhang, Y. Mao, Y. Y. Zhu, Z. Yang, C. T. Chan, and P. Sheng, "Locally resonant sonic materials," *Science* **289**, 1734–1736 (2000).
- [12] J. Mei, Z. Liu, W. Wen, and P. Sheng, "Effective mass density of fluid-solid composites," *Phys. Rev. Lett.* **96**, 024301 (2006).
- [13] G. W. Milton and J. R. Willis, "On modifications of Newton's second law and linear continuum elastodynamics," *Proc. R. Soc. A* **463**, 855–880 (2007).
- [14] G. Nagai, J. Fish, and K. Watanabe, "Stabilized nonlocal model for dispersive wave propagation in heterogeneous media," *Comput. Mech.* **33**, 144–153 (2004).

DYNAMIC HOMOGENIZATION OF DAMPED PERIODIC MATERIALS

- [15] S. Nemat-Nasser, J. R. Willis, A. Srivastava, and A. V. Amirkhizi, "Homogenization of periodic elastic composites and locally resonant sonic materials," *Phys. Rev. B* **83**, 104103 (2011).
- [16] S. Nemat-Nasser and A. Srivastava, "Overall dynamic constitutive relations of layered elastic composites," *J. Mech. Phys. Solids* **59**, 1953–1956 (2011).
- [17] A. N. Norris, A. L. Shuvalov, and A. A. Kutsenko, "Analytical formulation of three dimensional dynamic homogenization for periodic elastic systems," *Proc. R. Soc. A* **468**, 1629–1651 (2012).
- [18] A. L. Shuvalov, A. A. Kutsenko, A. N. Norris, and O. Poncelet, "Effective Willis constitutive equations for periodically stratified anisotropic elastic media," *Proc. R. Soc. A* **467**, 1749–1769 (2011).
- [19] A. Srivastava and S. Nemat-Nasser, "Overall dynamic properties of three-dimensional periodic elastic composites," *Proc. R. Soc. A* **468**, 269–287 (2012).
- [20] J. R. Willis, "The overall elastic response of composite materials," *J. Appl. Mech. ASME* **50**, 1202–1209 (1983).
- [21] J. R. Willis, *Dynamics of composites*, Continuum Micromechanics: CISM Lecture Notes, Vienna, Austria: Springer 1997.
- [22] J. R. Willis, "Exact effective relations for dynamics of a laminated body," *Mech. Materials* **41**, 385–393 (2009).
- [23] J. Zhu, J. Christensen, J. Jung, L. Martin-Moreno, X. Yin, L. Fok, X. Zhang, and F. J. Garcia-Vidal, "A holey-structured metamaterial for acoustic deep-subwavelength imaging," *Nature Phys.* **7**, 52–55.

*E-mail address:* michael.frazier@colorado.edu

DEPARTMENT OF AEROSPACE ENGINEERING SCIENCES, UNIVERSITY OF COLORADO, BOULDER, COLORADO

# ATTENTION ALLOCATION TO RACIAL OUTGROUPS

STEFFANIE GUILLERMO

**ABSTRACT.** The current research examined attention allocation towards Black, Latino, and Asian faces, compared to White, ingroup faces, in three separate studies. Attention was measured with an exogenous cueing task that assessed attentional capture and holding towards faces of each racial group. These studies show that participants demonstrate attentional biases towards Black and Latino faces compared to White faces, but do not attend differently to Asian versus White faces. Thus, attention allocation is biased towards certain racial outgroups, perhaps those stereotypically associated with threat. Collectively, these studies show pronounced attention to racial outgroup Black and Latino faces.

## 1. INTRODUCTION

Social psychological research demonstrates that people show pronounced attention to threat-relevant cues, such as angry faces [5] [4]. Within the stereotyping and prejudice literature, research shows that these attentional biases also manifest themselves towards racial groups stereotypically associated with threat. White participants preferentially attend to Black faces compared to White faces [7], with some evidence suggesting that participants' stereotypic associations between Blacks and threat predict these attentional biases [2]. The present research examined attentional biases towards various racial groups, some of which are stereotypically associated with threat and also a racial group not associated with threat. Specifically, the current research investigated attention allocation towards Black, Latino, and Asian faces compared to White, ingroup faces. If biases in attention manifest themselves specifically towards stereotypically threatening racial outgroups, then White participants should preferentially attend to Black and Latino versus White faces, as research suggests that these racial groups are stereotypically associated with threat [1] [8]. In contrast, there should be no preferential attention for Asian compared to White faces, since Asians are not stereotypically associated with threat [3] [6]. In three separate studies, attention to outgroup Black, Latino, and Asian faces compared to White, ingroup faces was measured with an exogenous cueing task that assessed attentional capture and holding towards faces of each racial group. The goal of the current research was to examine whether attention allocation is more pronounced only for racial outgroups stereotypically associated with threat.

## 2. STUDY 1

**2.1. Methods.** *Participants.* Participants were 35 White undergraduates at the University of Colorado, Boulder.

*Design.* Study 1 used an exogenous cueing task with Black and White faces [2]. On

---

*Date:* August 8, 2015.

*Key words and phrases.* social cognition; stereotyping; race; attention.

each trial, participants were presented with a fixation cross in the center of the screen for 500 ms. Then, a face appeared on the left or right side of the screen for 100 ms. The race and location of the face were randomized across trials. Next, a dot appeared on either the left or right side of the screen for 1500 ms. Participants' task was to respond to the location of the dot. The task employed two different types of trials: valid and invalid. On valid trials, the dot appeared on the same side of the screen as the face. These trials assessed the extent to which faces capture attention. On invalid trials, the dot appeared on the opposite side of the screen as the face. Invalid trials assessed the extent to which faces hold attention.

**2.2. Results and Discussion.** *Analytic Strategy.* Attention to race was analyzed by computing an attention index for each racial group. This index was calculated by subtracting participants' response times on valid trials from their response times on invalid trials. Higher values suggest that the face captured attention (reducing response times on valid trials) and held it (increasing response times on invalid trials).

*Results.* Using a repeated measures analysis, response times were analyzed for (a) valid and invalid trials involving (b) Black and White faces. The Race X Validity interaction was significant,  $F(1, 34) = 4.58, p < 0.04$ . This significant interaction indicates that the index of attention to Black faces ( $M = 0.041, s = 0.062$ ) was greater than the index of attention to White faces ( $M = 0.018, s = 0.053$ ). Looking only at valid trials, Black faces captured attention significantly faster than White faces,  $t(34) = 4.02, p < 0.001$ . There was no evidence that Black faces held attention significantly longer than White faces,  $t(34) = 4.02, p < 0.912$ . This finding is consistent with previous research showing that White participants preferentially attend to Black compared to White faces.

### 3. STUDY 2

**3.1. Methods.** *Participants.* Participants were 41 White undergraduates at the University of Colorado, Boulder.

*Design.* Study 2 used the same exogenous cueing task as Study 1, with the exception of including Latino faces instead of Black faces.

**3.2. Results and Discussion.** I analyzed the data for Study 2 as I did for Study 1. The Race X Validity interaction was significant,  $F(1, 40) = 5.43, p < 0.025$ , indicating that the index of attention to Latino faces ( $M = 0.016, s = 0.060$ ) was greater than the index of attention to White faces ( $M = -0.006, s = 0.053$ ). An analysis of valid trials revealed that Latino faces ( $M = 5.803, s = 0.107$ ) did not capture attention significantly faster than White faces ( $M = 5.807, s = 0.116$ ),  $t(40) = 0.63, p < 0.535$ . However, an analysis of the invalid trials showed that Latino faces ( $M = 5.820, s = 0.138$ ) held attention significantly longer than White faces ( $M = 5.801, s = 0.128$ ),  $t(40) = 2.52, p < 0.017$ .

### 4. STUDY 3

**4.1. Methods.** *Participants.* Participants were 33 White undergraduates at the University of Colorado, Boulder.

*Design.* Study 3 used the same exogenous cueing task as in Studies 1 and 2, with the exception of including Asian faces instead of Black or Latino faces.

**4.2. Results and Discussion.** I used the same analytic strategy for Study 3, assessing the Race X Validity interaction. Results showed that this interaction was not significant,  $F(1, 32) = 0.63, p < 0.433$ . The data did not show any significant differences in attention to Asian faces ( $M = 0.039, s = 0.090$ ) compared to White faces ( $M = 0.047, s = 0.087$ ). An analysis of valid and invalid trials showed that Asian faces did not capture attention faster nor hold attention longer than White faces,  $t$ 's  $< 1.4, n.s.$  Thus, there is no evidence of preferential attention to Asian versus White faces.

## 5. GENERAL DISCUSSION

The current research investigated attention allocation to racial outgroup versus ingroup faces. Specifically, I examined attention to Blacks and Latinos - racial groups stereotypically associated with threat and Asians, who are not stereotyped as threatening. The findings demonstrate that attention allocation is biased towards Black and Latino faces compared to White, ingroup faces. There was no evidence of preferential attention to Asian versus White faces. Thus, attention allocation is biased towards certain racial outgroups, perhaps only those stereotypically associated with threat. Current research is directly investigating the influence of threat-relevant stereotypes as the underlying mechanism of racially biased attention allocation. Collectively, these studies show pronounced attention to racial outgroup Black and Latino, but not Asian faces, compared to White, ingroup faces.

## REFERENCES

- [1] Devine, P. G. (1989). "Stereotypes and prejudice: their automatic and controlled components." *Journal of Personality and Social Psychology*, 56(1), 5.
- [2] Donders, N.C., Correll, J., and Wittenbrink, B. (2008). "Danger stereotypes predict racially biased attentional allocation." *Journal of Experimental Social Psychology*, 44, 1328-1333.
- [3] Fiske, S. T., Cuddy, A. J., Glick, P., and Xu, J. (2002). "A model of (often mixed) stereotype content: competence and warmth respectively follow from perceived status and competition." *Journal of Personality and Social Psychology*, 82(6), 878.
- [4] Fox, E., Lester, V., Russo, R., Bowles, R. J., Pichler, A., and Dutton, K. (2000). "Facial expressions of emotion: Are angry faces detected more efficiently?." *Cognition and Emotion*, 14(1), 61-92.
- [5] Hansen, C. H., and Hansen, R. D. (1988). "Finding the face in the crowd: an anger superiority effect." *Journal of Personality and Social Psychology*, 54(6), 917.
- [6] Katz, D., and Braly, K. (1933). "Racial stereotypes of one hundred college students." *The Journal of Abnormal and Social Psychology*, 28(3), 280.
- [7] Trawalter, S., Todd, A. R., Baird, A. A., and Richeson, J. A. (2008). "Attending to threat: Race-based patterns of selective attention." *Journal of Experimental Social Psychology*, 44(5), 1322-1327.
- [8] Weaver, C. N. (2005). "The changing image of Hispanic Americans." *Hispanic Journal of Behavioral Sciences*, 27(3), 337-354.

*E-mail address:* [steffani.guillermo@colorado.edu](mailto:steffani.guillermo@colorado.edu)

DEPARTMENT OF PSYCHOLOGY, UNIVERSITY OF COLORADO, BOULDER, COLORADO

# THE EFFECTS OF GENDER COMPOSITION IN A GROUP MATH TASK

SARAH GROVER

**ABSTRACT.** This research examines the effect of gender composition on group interactions in pSTEM. In each group a female target was given added math expertise. These female “experts” experienced less social cohesion with group members, participated less in the group math task and were rated as worse at math in male-dominated groups than in all-female groups.

## 1. INTRODUCTION

Advances in physical science, technology, engineering and math (pSTEM) fields are driven by collaboration between teams of people. Over the years, pSTEM education has become increasingly collaborative. While STEM environments are often collaborative, they also tend to be male-dominated. Women remain underrepresented in pSTEM, earning about 20% of the undergraduate degrees in these fields [1]. As a direct consequence, female pSTEM majors may often be the only female student in their group. Research in social psychology has shown that cues of underrepresentation that remind minority group members of their stigmatized identity in a domain have detrimental effects on the social cohesion that they experience with majority group members and on their performance in the domain. The present research examines how group gender composition affects group dynamics, and self- and others’ perceptions of a female group member’s math ability. We propose that cues of underrepresentation in pSTEM have negative consequences for social cohesion between female students and their male group members, and for female students’ ability to contribute their unique expertise in a collaborative context. These effects are consequential in their own right, however, they may also have adverse implications for how women perceive their own capabilities in pSTEM fields and for how their capabilities in pSTEM are perceived by their peers.

## 2. UNDERREPRESENTATION AND BELONGING

Cues of belonging are especially important for minority group members who face ability-demeaning stereotypes. Ability-demeaning stereotypes are stigmatizing and can cause minority group members to question their belonging in the stereotyped domain. Negative stereotypes about women’s math and science ability can cause women to feel less belonging in pSTEM fields. A strong sense of belonging in pSTEM is an important contributor to women’s achievement and persistence in these fields [2] [3] [4]. Women’s sense of belonging in math decreased over the course of taking a college calculus class; this decrease in belonging predicted weaker intentions to continue taking math classes after completing calculus [3]. Underrepresentation of women in pSTEM fields is one

---

*Date:* August 8, 2015.

*Key words and phrases.* gender stereotypes, underrepresentation, STEM, group problem solving.

environmental cue that contributes to women’s lower sense of belonging in pSTEM fields. Women who watched a video of a science and engineering conference that was manipulated to be male-dominated (3:1 male to female ratio) reported a lower sense of belonging in science and engineering compared to women who watched a science and engineering conference video that was manipulated to be at gender parity (1:1 male to female ratio) [5]. Taken together, this research demonstrates that belonging is an important predictor of women’s success in pSTEM fields and that cues of women’s underrepresentation can lower their sense of belonging in pSTEM fields.

### 3. UNDERREPRESENTATION AND STEREOTYPE THREAT

Stereotype threat is the concern that one will be judged through the lens of an ability-demeaning stereotype. The concern prompted by stereotype threat can take up precious cognitive resources, and ironically, lead to impaired performance on cognitively demanding tasks. Previous research has shown that cues of women’s underrepresentation in pSTEM fields are sufficiently powerful to prompt stereotype threat effects. Research by Inzlicht and Ben-Zeev (2000) showed that women performed worse on a challenging math test when they were the only female test-taker than when all of the other test-takers were also female [6]. Thus, this research suggests that cues of underrepresentation adversely affect women’s math test performance as well as their sense of belonging in pSTEM fields.

### 4. HYPOTHESES

The present research builds upon previous research by examining the impact of cues of underrepresentation in a collaborative group context, much like those that are increasingly common in pSTEM fields. Examining cues of underrepresentation allows us to examine their effects on group dynamics, as well as downstream consequences for perceptions of women’s math ability both from the perspective of the target of the stereotype and from non-targets.

### 5. OVERVIEW OF STUDIES

Across two studies we tested whether group gender composition affected self- and others’ perceptions of a female expert’s math ability. In both studies, groups of four participants were brought into the lab. We arranged it so that the groups were either male-dominated or all-female. Male-dominated groups consisted of three male participants and one female participant, and all-female groups consisted of four female participants.

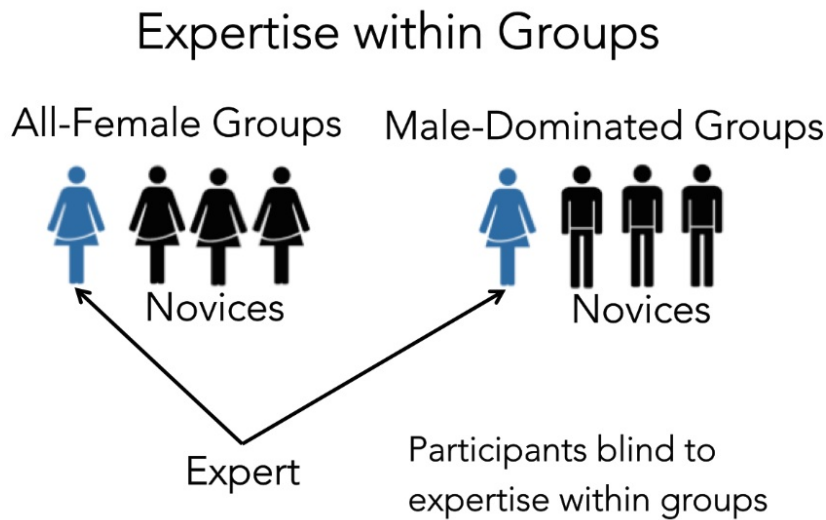
In Study 1, we used a strong manipulation of identity-threatening cues, in addition to manipulating group gender composition, we also manipulated the group task instructions to elicit or protect against stereotype threat. Previous research has shown that framing a task as diagnostic of ability [7], and also mentioning group differences in performance [8] [9] are both cues that elicit stereotype threat effects. Thus, male-dominated groups were told that the group task was diagnostic of true math ability and that men tend to perform better than women on these types of problems. By contrast, all-female groups were told that the problems were not intended to test math ability,

and that we were simply interested in how they worked together as a group ( $N = 48$  four-person groups; 24 male-dominated).

The Study 2 procedures were identical to Study 1 procedures with one important exception. In Study 2, group gender composition (male-dominated vs. all-female) was the only factor that was manipulated across groups; all groups were told that the problems were diagnostic of true math ability, but there was no mention of gender differences in performance on the problems ( $N = 59$  four-person groups; 30 male-dominated).

In both studies, we used individual tutorials to experimentally manipulate expertise within each group. One female in each group, the expert, was trained to solve problems nearly identical to those that would be presented in the group task. The other three participants, the novices, were not trained to solve problems that were relevant to the problems presented in the group task. Although participants were told that they might receive different tutorials, they were unaware of the contents of their group members' tutorials and did not know that there was only one female expert in each group. Male-dominated groups always consisted of three male novices and one female expert, and all-female groups always consisted of three female novices and one female expert (see Figure 1). The expert tutorial allowed us to equate female experts on training for the group problems.

FIGURE 1. Gender Composition and Expertise within Groups.



Each group had fifteen minutes to complete four multiple-choice problems, and all groups did so in the allotted time. The first two problems were easy warm-up problems intended to allow participants to become familiar with the task and their group members. The second two problems were nearly identical to the problems presented in the female expert's tutorial, but used different numbers. We told groups to work together to solve each problem. Groups were also told that they would be filmed so we could see how they worked together. A male and a female undergraduate research assistant blind to

study hypotheses coded each video to obtain a behavioral measure of the female expert's actual performance on the expert-relevant group problems.

Following the group task, participants returned to their individual cubicles to complete a questionnaire in which they completed judgments of each of their group members and themselves. Our primary outcome of interest was perceived math ability, which is a composite of six items assessing different aspects of math ability including the quality of contributions in the group task and perceptions of trait-level math ability ( $\alpha_{\text{study 1}} = .91$ ;  $\alpha_{\text{study 2}} = .92$ ). Participants also rated the extent to which they enjoyed having each of the other participants in their group, how much they felt they belonged in the group and their endorsement of the stereotype that men are better at math than women.

Despite the fact that female experts were equated on training in male-dominated and all-female, we expected that female experts in male-dominated groups would be perceived as worse at math as compared to female experts in all-female groups by both themselves and others (Hypothesis 1). We also expected to find lower social cohesion between the female expert and her group members in male-dominated groups as compared to in all-female groups (Hypothesis 2) and that female experts in male-dominated groups would actually perform worse in the group task compared to female experts in all-female groups (Hypothesis 3). We hypothesized the effect of group composition on perceptions of the female experts' math ability would be explained (i.e., mediated) by lower social cohesion between the female experts and the novices, and the female experts' poorer performance in male-dominated groups compared to all-female groups (Hypothesis 4).

## 6. SUMMARY OF RESULTS

First, I will present the results testing our primary hypothesis that female experts would be perceived as worse at math in male-dominated groups as compared to in all-female groups (Hypothesis 1). To test this hypothesis we analyzed our composite measure of perceived math ability in a 2 Group Composition (all-female vs. male-dominated) x 2 Target of Judgment (expert vs. novices) x 2 Perceiver (expert vs. novices) multilevel model with Kenward-Roger approximate degrees of freedom (two-tailed test with  $\alpha = .05$ ). We analyze the data in a multilevel model to account for the dependence in the data due to the grouping of participants. The results of both Study 1 and Study 2 revealed a significant interaction of Group Composition with Target of Judgment  $F_{\text{Study1}}(1, 63.9) = 5.61, p = .02, F_{\text{Study2}}(1, 65.9) = 6.39, p = .01$  (See Figure 2 for a plot of the interaction in Study 1 and Figure 3 for a plot of the interaction in Study 2). This interaction was not further qualified by an interaction with Perceiver, which demonstrates that the interaction was the same for the experts' and novices' perceptions of math ability. To interpret the interaction in the two studies we tested the simple effects of Group Composition. Consistent with Hypothesis 1, in both Study 1 and in Study 2, we found that female experts in male-dominated groups were perceived as worse at math compared to female experts in all-female groups, by both themselves and their group members  $t_{\text{Study1}}(202) = 3.55, p = .0005, t_{\text{Study2}}(84.7) = 2.99, p = .004$ . Whereas there was no significant difference in perceptions of the male novices' math ability as compared to the female novices' math

THE EFFECTS OF GENDER COMPOSITION IN A GROUP MATH TASK

ability in either study  $t_{\text{Study1}}(74.6) = 0.39, n.s.$ ,  $t_{\text{Study2}}(65.7) = -1.49, n.s.$  Given that there was no significant difference in perceptions of the novices' math ability in male-dominated as compared to all-female groups, we were able to rule out the possibility that participants in all-female groups simply rated everyone higher on math ability than participants in male-dominated groups.

FIGURE 2. Study 1 perceived math ability by Target and Condition, collapsing across Perceiver. Error bars represent  $\pm 1$  standard error.

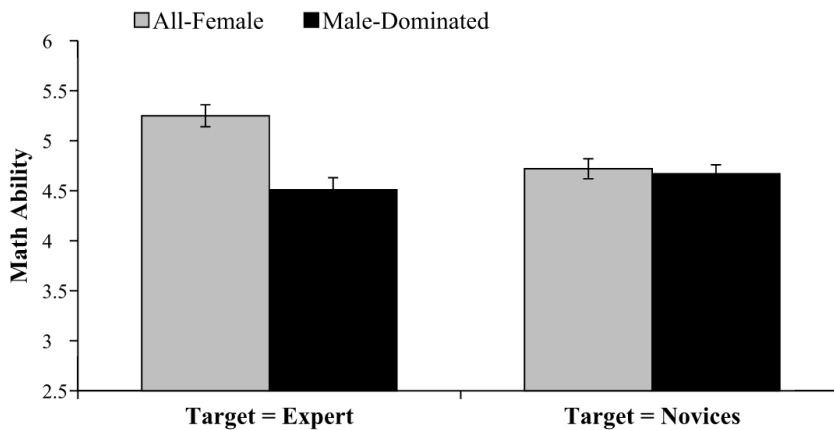
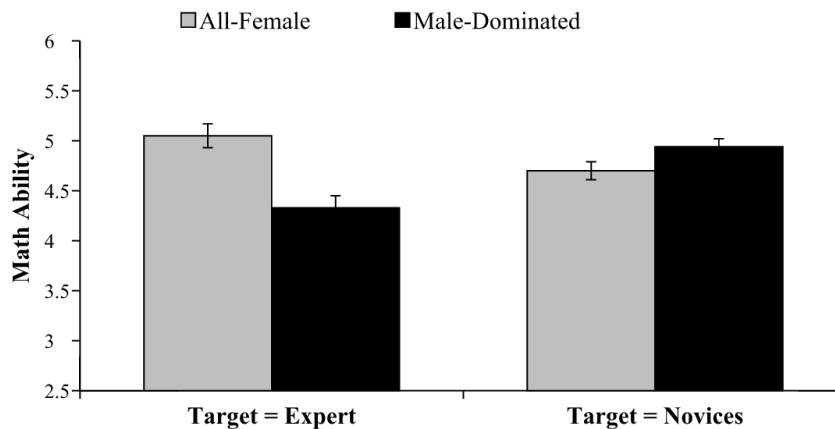


FIGURE 3. Study 2 perceived math ability by Target and Condition, collapsing across Perceiver. Error bars represent  $\pm 1$  standard error.



We provide tests of Hypotheses 2-4 in the following analyses. For the sake of increased statistical power and parsimony, we combine data from the two studies for these analyses, including Study 1 as a covariate to control for any differences due to Study 2. We examine the effect of group composition in two separate multiple mediation models, one for the experts' self-perceptions and the other for the novices' perceptions of

the experts to allow for the possibility that different processes could drive the effect of group composition on self- versus others' perceptions. Estimates of indirect effects were obtained with 5,000 bootstrap resamples. In both multiple mediation analyses we examined four potential mediators of the effect of group gender composition on perceptions of the female experts' math ability, these included the female expert's sense of belonging in the group, the extent to which the novices enjoyed having the female expert as a group member, the female expert's performance on the expert-relevant problems, and the novices' stereotype endorsement. We found a significant difference between male-dominated and all-female groups for each of the four proposed mediators. Consistent with Hypothesis 2, female experts reported less belonging in male-dominated groups than in all-female groups  $\beta = -.30$ ,  $SE = .09$ ,  $p = .002$ , and that male novices enjoyed having the female expert as a group member significantly less than female novices did,  $\beta = -.34$ ,  $SE = .09$ ,  $p = .0004$ . Consistent with Hypothesis 3, we found that female experts in male-dominated groups performed significantly worse on the expert-relevant problems than female experts in all-female groups  $\beta = -.20$ ,  $SE = .08$ ,  $p = .02$ . In support of Hypothesis 4, we also found that male novices endorsed the stereotype that men are better at math than women more strongly than female novices did  $\beta = .21$ ,  $SE = .10$ ,  $p = .03$ .

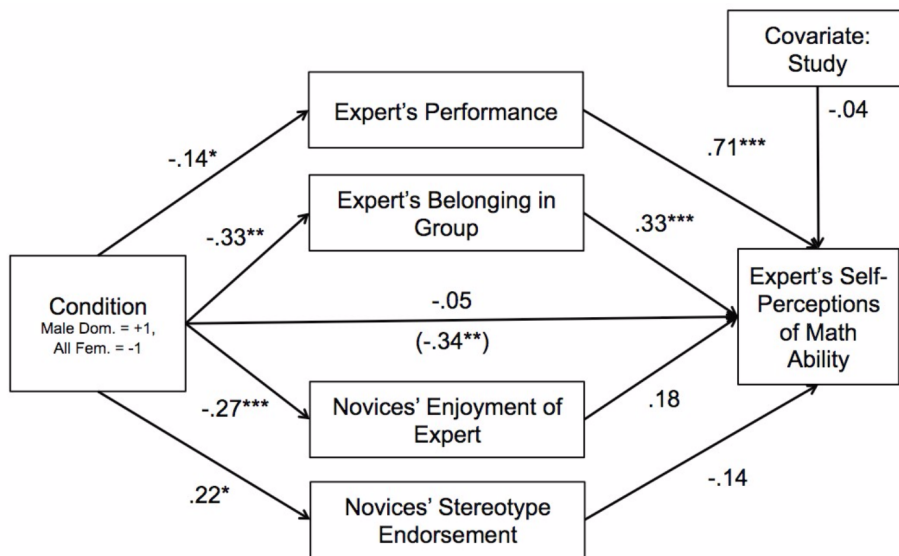
The results of the multiple mediation analysis for the female experts' self-perceptions of math ability are presented in Figure 4. First, we see that female experts in male-dominated groups saw themselves as significantly worse at math than female experts in all-female groups  $\beta = -.27$ ,  $SE = .09$ ,  $p = .004$ , consistent with Hypothesis 1. After accounting for the four proposed mediators the effect of group composition on the female expert's self-perceptions of math ability was no longer significant  $\beta = -.04$ ,  $SE = .08$ ,  $p = .63$ , *n.s.* Two different processes explained the effect of group composition on the experts' self-perceptions of math ability. First, the female experts' lower sense of belonging contributed to the effect  $\beta = -.08$ ,  $SE = .04$ , 95%  $CI[-.17, -.02]$ , and second, the effect was explained by the female experts' performance on the expert-relevant problems  $\beta = -.09$ ,  $SE = .04$ , 95%  $CI[-.18, -.03]$ .

Finally, we examine the results of the same multiple mediation analysis for the novices' perceptions of the female experts' math ability. We see that male novices perceived female experts as significantly worse at math than female novices did  $\beta = -.37$ ,  $SE = .09$ ,  $p = .0001$ . Again, the four mediators completely accounted for the effect of group composition on novices' perceptions of female experts' math ability  $\beta = -.09$ ,  $SE = .07$ ,  $p = .17$ , *n.s.* Two significant mediators emerged from the analysis. First, the effect of group composition on the novices' perceptions of the expert's math ability was in part accounted for by the experts' poorer performance in male-dominated groups  $\beta = -.05$ ,  $SE = .03$ , 95%  $CI[-.13, -.009]$ . Second, the extent to which novices enjoyed having the expert in their group also accounted for the effect of group composition  $\beta = -.17$ ,  $SE = .06$ , 95%  $CI[-.33, -.10]$ .

Taken together, the results of these multiple mediation analyses provided support for Hypothesis 4 that the effect of Group Composition on perceptions of the female expert's math ability would be mediated by lower social cohesion and the expert's poorer performance in male-dominated groups compared to all-female groups. Although we found that male novices explicitly endorsed the stereotype that men are better than women at math, this difference did not emerge as a significant mediator in either analysis.

THE EFFECTS OF GENDER COMPOSITION IN A GROUP MATH TASK

FIGURE 4. Multiple mediation model of female expert’s self-perceptions of math ability. Path values represent the unstandardized regression coefficients. The value inside of the parentheses below the middle line is the total effect of Group Composition. The value above the middle line is the direct effect of Group Composition after accounting for the four mediators. Group Composition is a contrast-coded variable, male-dominated groups = +1, all-female groups = -1. Study is also a contrast coded variable, Study 1 = -1, Study 2 = +1. [  $p < .1$ , \*  $p < .05$ , \*\*  $p < .01$ , \*\*\*  $p < .001$ . ]

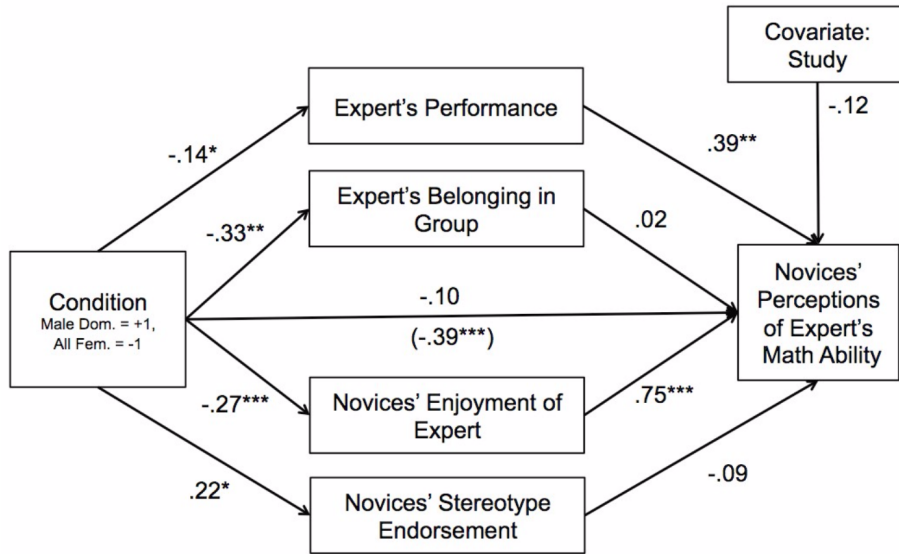


7. CONCLUSION

Despite receiving equivalent training, female experts in threatening male-dominated groups were perceived as worse at math groups as compared to experts in all-female groups. We saw that the effect of group composition on perceptions of the female experts’ math ability was driven by lower social cohesion and the experts’ poorer performance in male-dominated groups as compared to all-female groups.

In conclusion, these studies show us that male-dominated groups can hinder the extent to which women’s prior training and ability is able to shine through in a collaborative context. This research suggests that women are likely to experience less social cohesion with male peers in male dominated groups and not perform as well as they could in a non-threatening all-female group. We know that both of these effects are extremely important because they each have a unique negative effect on women’s self-perceptions and their group members’ perceptions of their math ability. Collaborations in STEM could be even more productive and educationally beneficial if the environments were more collegial and less identity threatening for women. We conclude that

FIGURE 5. Multiple mediation model of the novices' perceptions of the female expert's math ability. Path values represent the unstandardized regression coefficients. The value inside of the parentheses below the middle line is the total effect of Group Composition. The value above the middle line is the direct effect of Group Composition after accounting for the four mediators. Group Composition is a contrast-coded variable, male-dominated groups = +1, all-female groups = -1. Study is also a contrast coded variable, Study 1 = -1, Study 2 = +1. [ $p < .1$ , \*  $p < .05$ , \*\*  $p < .01$ , \*\*\*  $p < .001$ .]



interventions to improve women's success in STEM fields should not only aim to reduce stereotype threat but also should work to promote social cohesion between male and female group members.

## 8. ACKNOWLEDGEMENTS

I would like to thank the STEMinar for the generous grant to support my continued research on the effects of group gender composition on group dynamics in pSTEM fields. I would also like to thank my advisers Dr. Tiffany Ito and Dr. Bernadette Park and the CU Stereotyping and Prejudice Lab. This research was supported by an NSF graduate research fellowship awarded to Sarah Grover.

## REFERENCES

- [1] Science and Engineering Indicators. (National Science Foundation, 2014).
- [2] Cheryan, S., Plaut, V. C., Davies, P. G. and Steele, C. M. Ambient belonging: How stereotypical cues impact gender participation in computer science. *J. Pers. Soc. Psych.* 97, 1045-1060 (2009).
- [3] Good, C., Rattan, A. and Dweck, C. S. Why do women opt out? Sense of belonging and women's representation in mathematics. *J. Pers. Soc. Psych.* 102, 700 (2012).

THE EFFECTS OF GENDER COMPOSITION IN A GROUP MATH TASK

- [4] Lewis, K. L. et al. Fitting in to Move Forward: Using a Belonging Framework to Understand Gender Disparities in Persistence in the Physical Sciences, Technology, Engineering, and Mathematics (pSTEM). (Under review).
- [5] Murphy, M. C., Steele, C. M. and Gross, J. J. Signaling threat: How situational cues affect women in math, science, and engineering settings. *Psych. Sci.* 18, 879-885 (2007).
- [6] Inzlicht, M. and Ben-Zeev, T. A threatening intellectual environment: Why females are susceptible to experiencing problem-solving deficits in the presence of males. *Psych. Sci.* 11, 365-371 (2000).
- [7] Steele, C. M. and Aronson, J. Stereotype threat and the intellectual test performance of African Americans. *J. Pers. Soc. Psych.* 69, 797-811 (1995).
- [8] Aronson, J. et al. When White men can't do math: Necessary and sufficient factors in stereotype threat. *J. Exp. Soc. Psych.* 35, 29-46 (1999).
- [9] Spencer, S. J., Steele, C. M. and Quinn, D. M. Stereotype threat and women's math performance. *J. Exp. Soc. Psych.* 35, 4-28 (1999).

*E-mail address:* Sarah.Grover@colorado.edu

DEPARTMENT OF PSYCHOLOGY, UNIVERSITY OF COLORADO, BOULDER, COLORADO

# TRACKING SUPRAGLACIAL LAKE CHANGES ON NGOZUMPA GLACIER, NEPAL

ULYANA HORODYSKYJ

**ABSTRACT.** The formation of supraglacial (surface) lakes appears to be a catalyst for ice mass loss on debris-covered glaciers in the Himalayan Mountains. Once formed, these lakes can grow through expansion, by melting and collapsing of surrounding ice walls, and through deepening of their ice floors. As lake water volume increases, so too does the risk for glacial lake outburst floods (GLOFs). Spillway Lake, a large supraglacial base-level lake on Ngozumpa, one of Nepal's largest and longest glaciers, has been growing since the 1980s. This research utilized time-lapse cameras, weather stations, temperature buoys, and sonar to track these changes in real-time.

Vertical temperature distribution in the sub-basins of Spillway Lake reveal mostly isothermal conditions in the summer, indicating the lake is well-mixed due to constant inputs of meltwater both from above ground (ice walls) and at depth, from englacial and/or subglacial channels. Lake floor melting rate is highest in the fall season, after surface melting ceases and the lake bodies have had sufficient time to accumulate heat. However, the presence of thick debris (mud and rock) on lake floors can insulate the ice from melting. Sonar imaging and 3D model construction of lake floors reveal areas prone to future deepening, which should continue to be monitored in the future.

## 1. INTRODUCTION

Since the 1950s and 1960s, many debris-covered glaciers in the Nepalese Himalaya have developed large moraine-dammed supraglacial lakes [18]. These are lakes that grow through expansion and deepening on the surface of a glacier [7] [15] [17]. As global temperatures continue to rise [16], and lakes continue to grow in volume, they pose a flooding risk to the villages below [5] [13]. The two conditions suggested to promote formation of supraglacial lakes are sloped surfaces  $< 2^\circ$  (see [12]), and surface speeds  $< 10$  m/yr (see [11]). Hence, they occur in terminal regions of “dead ice” zones of glaciers.

The Spillway is a supraglacial lake on the south/southeast-flowing Ngozumpa glacier in the Gokyo valley, lying between the Rowaling and Khumbu valleys of eastern Nepal (Fig. 1). Benn (2001) and Thompson (2012) have documented growth stages of this lake since the early 2000s [1] [17]. It has the capacity to grow into a much larger moraine-dammed lake (5 – 6 km in length). Presently, the Spillway consists of multiple sub-basins that are gradually merging into a larger lake. Its water level is controlled by the elevation of a spillway along the western lateral-frontal moraine (Fig. 1B).

Over the past three decades, Spillway has undergone cycles of rapid growth “spurts” alternating with periods of slower expansion [2]. Deepening rates vary locally in the

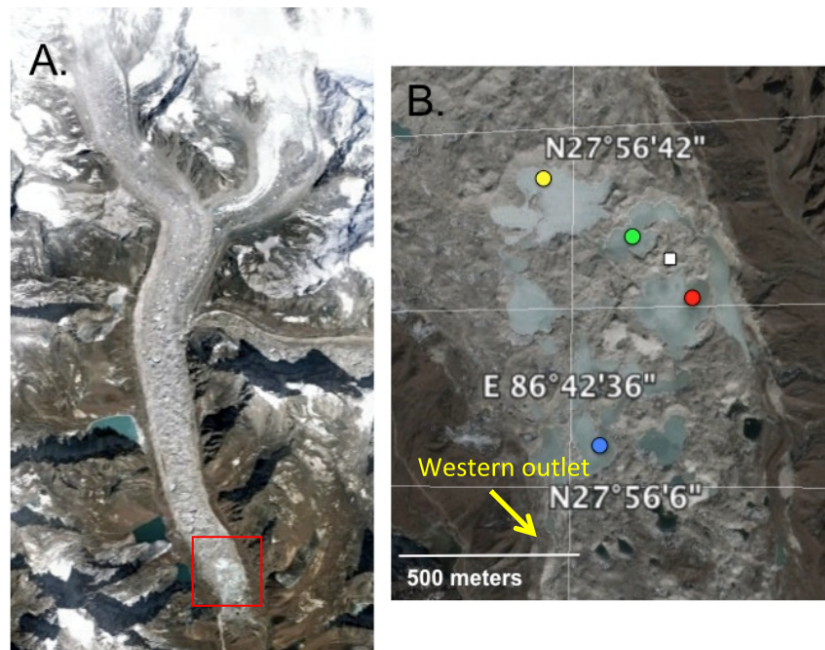
---

*Date:* August 8, 2015.

*Key words and phrases.* Himalaya, glacier, supraglacial lake, sonar .

sub-basins from less than a meter per year to tens of meters per year ([17]; cf. Thompson unpubl. data). Quantifying lake expansion and deepening remains an important objective, given the millions of cubic meters of water that can potentially outburst downstream.

FIGURE 1. 2014 GeoEye high-resolution satellite image of Ngozumpa glacier (A) with Spillway Lake close-up (B), showing temperature buoy locations in the sub-basins (yellow: northwest; green: northeast; red: main; blue: southwest), weather station (white square) and glacier outlet channel (yellow arrow).

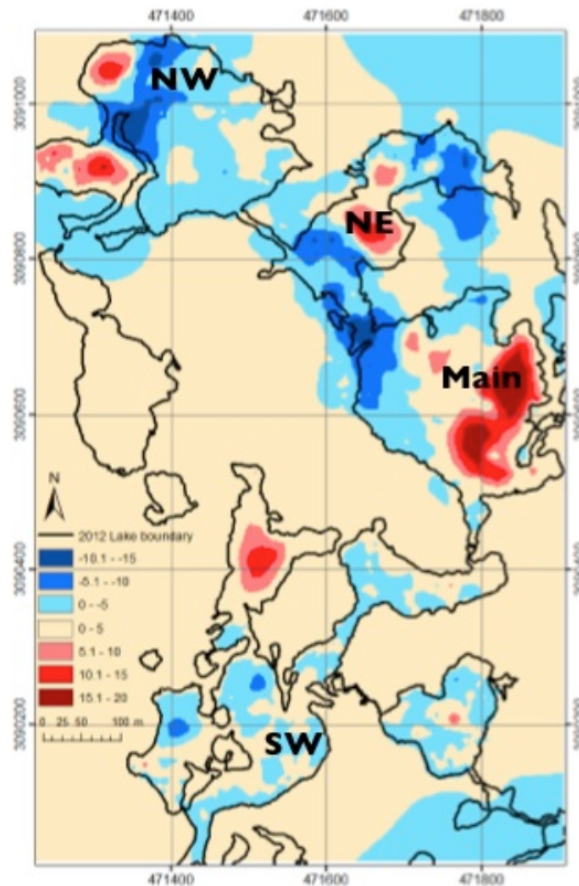


## 2. METHODS

Four study regions were selected within the Northwest (NW), Northeast (NE), Main, and Southwest (SW) sub-basins of Spillway Lake (Fig. 2) based on Thompson et al (2012) area and depth maps and new survey work from 2012. In this paper, I focus on the “Main” sub-basin, which has regions undergoing the most rapid deepening with time (5 – 7 m/yr). This sub-basin first began growing and expanding northward in 2001.

Turbidity with depth was measured in-situ (June 2014) with a handheld turbidimeter, using a 90-degree scatter nephelometer on a 30-meter weighted cable. The detected light intensity is directly proportional to the turbidity of the water. Water samples also were collected and measured in the lab with units reported in Nephelometric Turbidity Units (NTU). They were then filtered, weighed, and converted to suspended sediment concentration (SSC), as per the method in [3].

FIGURE 2. Derived depth-difference map from point-interpolated maps in 2009 and 2012. The 2012 data do not have the benefit of differential GPS height measurements (uncertainty  $\pm 1$  m). Areas of red are deepening, blue are shallowing, and beige is stable. Buoy locations from this study are noted (NW, NE, Main, and SW). In a 3-year period the most significant deepening (5 – 10 m) occurred in the Main sub-basin at seasonal rates of up to 7 m/yr.



For a week in June 2014 instantaneous vertical temperature profiles were measured using a weighted cable and handheld Oakton PC10 probe with a resolution of  $0.1^{\circ}$  C and accuracy of  $\pm 0.5^{\circ}$  C. For long-term measurements (June 2013 - June 2014), a buoy with three sensors on each line was constructed using surface and sub-surface pool floats, anchored to the lake floor with sandbags containing debris (mud and rock) dredged from the bottom.

Samples were collected from lake floors using an Ekman dredge with a trigger release messenger. In some regions, lake floor materials consisted of a thick mud packet, while in others it included a mixture of rocks, pebbles, and mud. Samples were measured at the Colorado School of Mines, using a KD-2 instrument to quantify heat capacity,

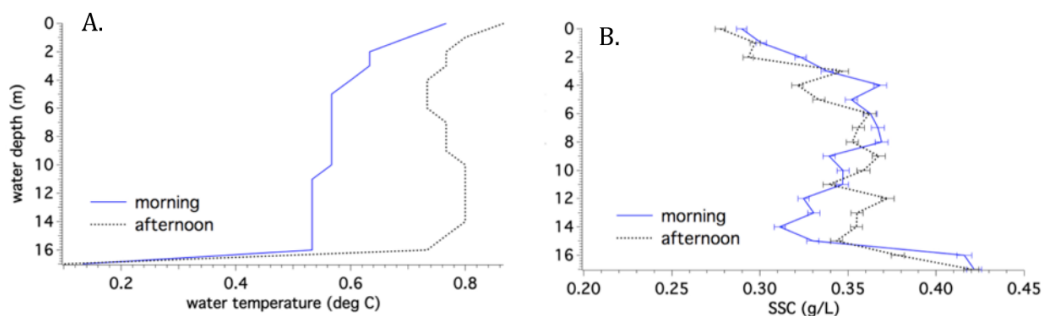
thermal diffusivity, and thermal conductivity, while particle density and porosity were measured separately.

Open water side-scan sonar transects were collected in early June 2014, after the lake thaw and before the start of the monsoon. A remote-operated boat, developed by a team at the Milwaukee School of Engineering and Midwest ROV LLC, provided the platform for a commercial fish finder, transducer, and GPS. Using multiple sonar returns during the transects, relative roughness and hardness maps provide information on presence of hard (rock) versus soft (mud), and compacted versus loose materials on the lake floors.

### 3. RESULTS

Temperatures and turbidity values (converted to suspended sediment concentration, SSC) were measured in the vicinity of the buoys for the sub-basins in the mornings and afternoons during the first week of June 2014. Figure 3A shows the temperature variations with depth in the Main sub-basin while Figure 3B shows the suspended sediment concentration variations. The lines represent morning and afternoon averages for the week. Main sub-basin is isothermal with depth until reaching  $0.1^{\circ}\text{C}$  at the bottom, which is interpreted to be either bare ice or a very thin layer of debris. A general trend of an increase in suspended sediment concentration (from approximately  $0.26 - 0.42\text{ g/L}$ ) with depth is seen.

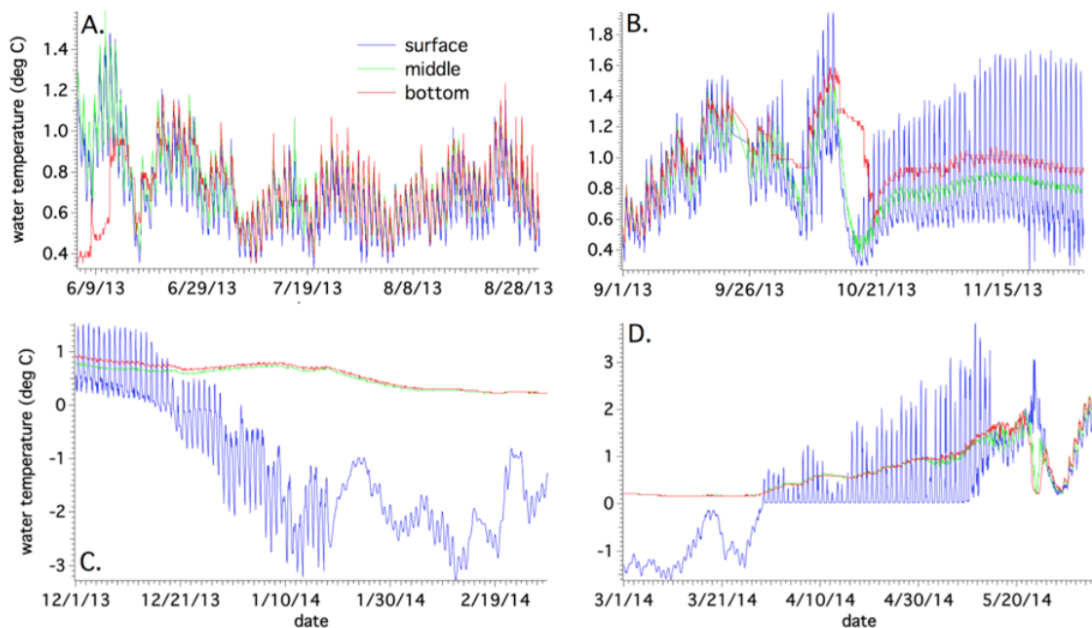
FIGURE 3. Vertical temperature and turbidity variations in the Main sub-basin. Blue line is indicative of morning averages while the black dotted line represents afternoon averages.



Long-term surface, middle and bottom temperatures were measured for the Main sub-basin (with a 17-m long buoy) from June 2013 - June 2014. The sub-basin was found to have an annual average temperature of  $0.136^{\circ}\text{C}$  (surface), due to long ice cover;  $0.706^{\circ}\text{C}$  (middle); and  $0.747^{\circ}\text{C}$  (bottom). Close-ups of seasonal temperature variations can be seen in Figure 4. During the summer (Fig. 4A), bottom temperatures reach a maximum of  $1.2^{\circ}\text{C}$ , while averaging  $0.7^{\circ}\text{C}$ . Similar temperatures from top to bottom indicate that during the monsoon, the lake is mostly isothermal and well-mixed. Inputs include subaerial meltwater from surrounding ice walls, englacial/subglacial sources, and precipitation. During the fall (Fig. 4B), average bottom temperatures increase to  $1^{\circ}$

C (max of  $1.59^{\circ}\text{C}$ ). During this time, due to decreasing air temperatures, subaerial and englacial melting inputs decrease, compared with the summer.

FIGURE 4. Seasonal temperature variations in Main sub-basin buoy location for the summer/monsoon (A), fall (B), winter (C) and spring (D). Surface sensor in blue; middle sensor in green; bottom sensor in red.



Cyclone Phailin dropped 1 meter of snow in the area in mid-October (2013), leading to a decrease in surface and bottom temperatures, from which point the latter did not recover to pre-cyclone values (Fig. 4B). During the winter freeze (Fig. 4C), bottom temperatures remain above zero ( $0.57^{\circ}\text{C}$ ). The delay in surface freezing is due to strong ( $0.8\text{ m/s}$ ) surface currents in the vicinity of the buoy locations; this has been documented in the field to persist through late December. During the spring thaw (Fig. 4D), the surface undergoes freeze-thaw cycles for most of April, until total thaw of the lake occurs in early May. Bottom temperatures peak out at  $2.45^{\circ}\text{C}$  before the water column mixes again at the end of the month. A late season snowstorm accounts for the anomaly seen in the data on May 26, when surface temperature suddenly dropped.

An Ekman dredge was used to collect samples from the sub-basins, to measure material properties in the lab including grain size, particle density, thermal conductivity, heat capacity, and diffusivity. Consistently at the buoy locations, dredged materials included a surface of compacted fine mud, with silt and sand-sized particles and pebbles mixed in with depth. Quantifying thermal conductivity of sediment is important when attempting to model ice melt below debris. Underwater, there is no need to account for meteorological variables, thereby reducing the complexity. Conductive heat flux can be calculated using:

$$Q_c = -k \frac{dT}{dz} \quad (3.1)$$

where  $k$  is the thermal conductivity of the material (W/m-K),  $T$  is the temperature within the sediment layer at some point  $z$  within that layer  $m$ , and  $Q_c$  is the downward conductive heat flux. As per Kraus (1975) (see [8]) and Nakawo and Young (1981) (see [9]), simplifying the temperature gradient to be linear within the debris layer, the equation becomes:

$$Q_c = \frac{k(T_s - T_i)}{h_d} \quad (3.2)$$

where  $T_s$  is the temperature at the surface of the debris and  $T_i$  is the temperature of the underlying ice, taken to be 0° C.

The melt rate can be calculated using:

$$M = 3.1536 \cdot 10^7 Q_c / L\rho$$

where the constant converts time from seconds to years,  $Q_c$  is the calculated heat flux,  $\rho$  is the density of ice, and  $L$  is the latent heat of melting. Debris samples were measured in the lab for their thermal properties (Table 1). The average thermal conductivity is approximately 1.8 W/m-K, close to that found previously (1.7 W/m-K) for debris on the surface of Ngozumpa by Nicholson and Benn (2006) [10].

TABLE 1. Six samples (one from each sub-basin and two extra within the Main sub-basin) and the average values for thermal conductivity (k), thermal resistivity (rho), volumetric heat capacity (C) and thermal diffusivity (D), with error.

	K (W/(m-K))	rho (°C-cm/W)	C (MJ/(m³-K))	D (mm²/s)	error
<b>Rocky mud mixture</b>	1.964	50.9	2.707	0.726	0.0058
	1.663	60.1	2.686	0.619	0.0050
	1.764	56.7	2.572	0.686	0.0080
	1.813	55.1	2.768	0.655	0.0090
	1.663	60.1	3.098	0.537	0.0067
	1.868	53.5	2.464	0.758	0.0044
<b>Average</b>	<b>1.789</b>	<b>56.067</b>	<b>2.716</b>	<b>0.664</b>	<b>0.006</b>

Calculated ice melt rates can be found in Table 2, which show annual rates for all the sub-basins (for comparison) with sediment thicknesses varying from 0.1 – 1 m. Figure 5 shows the seasonal variations. The thinner the debris, the faster the ice will melt. Rates are upwards of 10 m/yr in all sub-basins except for NW, which was the coldest overall basin. At only 10 cm of sediment, ice melt rates are reduced significantly, to less than 2 m/yr. With a 1 m thickness of sediment assumed to line the bottom of Spillway Lake (see [17]), the melting is found to be negligible in all sub-basins.

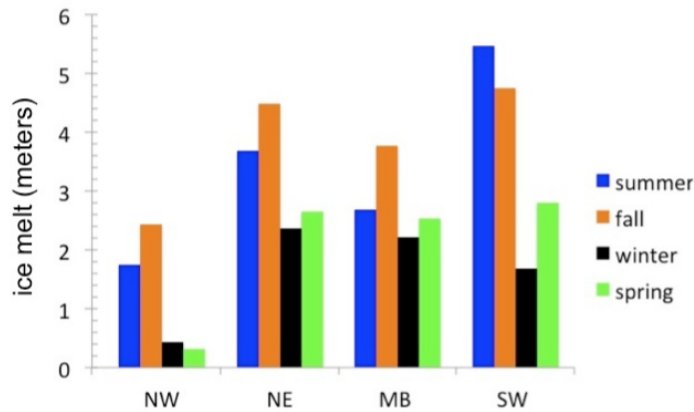
Figure 5 compares the sub-basins across the seasons, using only one debris thickness (1 cm) as an example. In NW, NE, and Main (MB), ice melt rates are highest during

TABLE 2. Seasonal ice melt rates (in m/yr) for all the sub-basins, with simulated debris thicknesses from 1 cm - 1 meter.

ANNUAL bottom ice melt				
Debris thickness (m)	NW (m)	NE (m)	MB (m)	SW (m)
0.01	6.13	16.41	14.06	18.38
0.02	3.06	8.21	7.03	9.19
0.05	1.23	3.28	2.81	3.68
0.1	0.61	1.64	1.41	1.84
0.15	0.41	1.09	0.94	1.23
0.3	0.20	0.55	0.47	0.61
0.5	0.12	0.33	0.28	0.37
1	0.06	0.16	0.14	0.18

the fall, while for SW, summer rates are higher. High rates in the SW basin can be attributed to its shallower depth and significant distance away from actively calving and/or melting ice walls. The decline of surface melting in the fall in the other basins aids in heat storage. Winter and spring rates are low in the NW buoy site, given its very cold temperatures throughout. The rates are comparable for the NE and MB. With the addition of an ice cover, heat can be dedicated towards bottom melting. This has been documented by Sakai and others (2000b) for small supraglacial ponds on the Khumbu glacier flowing off Mt. Everest [14].

FIGURE 5. Ice melt (meters) for the sub-basins during the summer (blue), fall (orange), winter (black) and spring (green), using 1 cm of debris thickness.



Lake floor roughness can be estimated by acoustic backscatter from the primary sonar echo (E1 layer). To the side scan sonar, smooth bottoms, such as compacted muds and sands act as acoustic mirrors and reflect most of the returning echo away from the receiver. In contrast, irregular bottom surfaces, consisting of rocks and boulders, reflect sound with multi-path back to the receiver. To determine bottom hardness, the secondary echo region (E2) or Peak Sv can be used. This is a measure of the acoustic

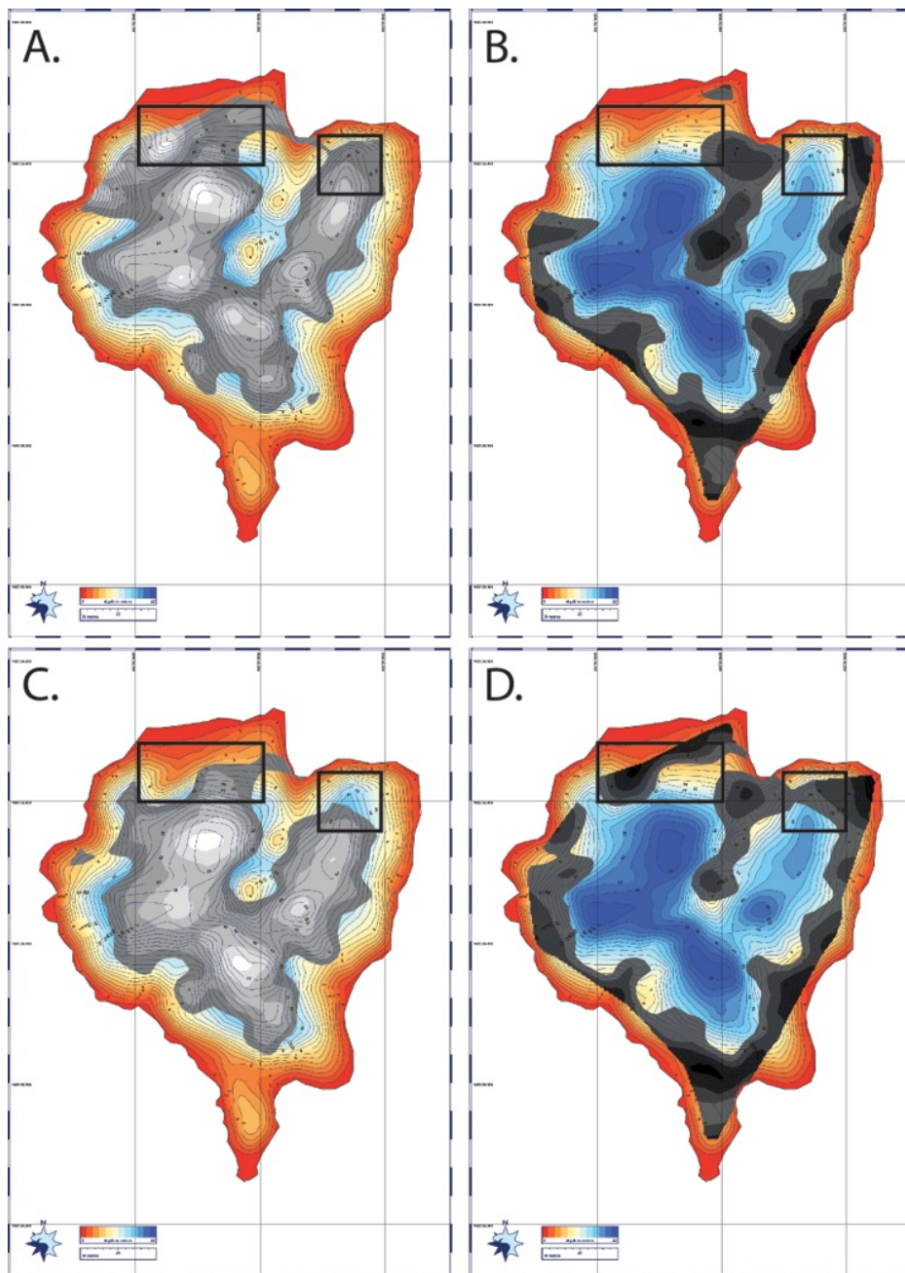
absorption or impedance of the bottom. Mud and materials with high water content will absorb a large proportion of the transmitted acoustic energy, reducing the echo amplitude, whereas hard substrates will reflect a greater proportion of the transmitted energy, resulting in high amplitude secondary echoes [4] [6].

Figure 6 shows E1 and Peak Sv maps for the Main sub-basin. (A) reveals smooth substrate from the E1 return while (C) shows soft substrate from the calculated Peak Sv. (B) and (D) show rocky (E1) and hard (Peak Sv), respectively. Rocky and hard returns in the Main sub-basin (Fig. 6B, D) are seen along shore and on the hummocky shallower terrain in the middle of the basin. Overlain black boxes highlight areas with smooth (A) and hard (D) returns, which reveal areas of possible bare or nearly bare ice. More field data are needed to validate these results, using seismic and/or ground-penetrating radar. However, in the case of Main sub-basin, vertical temperature measurements (Fig. 3A) showed  $0.1^{\circ}$  C at the bottom, while field photos revealed upwelling activity in the region, likely pointing to a active englacial/subglacial inputs and near-bare ice in the region.

#### 4. CONCLUSION

The Main buoy location was in 17 m of water. The emergence of its southern sector started in 2001, with northward expansion beginning in 2004. Northwestern expansion began in 2008. Thus, the oldest part of the sub-basin is in the south, while the youngest is towards the NW. The sonar returns, as seen in Figure 6 show smooth and soft in the deep, older areas of the basin, here interpreted to be mud. Sonar returns and substrate classification in the younger parts of the sub-basin point to hard and smooth surfaces and more research is needed to determine whether or not this is bare ice. However, this would correlate well with the high (5 – 7 m/yr) deepening rates in the region. Using the measured bottom water temperatures, to achieve these deepening rates in the older region of the basin would require  $< 5$  cm of debris coverage. However, given the age of the basin (13 years), there should have been sufficient time to accumulate thick debris. Documented flow currents of  $> 1$  m/s, even late into the dry season in the narrow region connecting the Main sub-basin with the lower parts of the lake (SW, as seen in Fig. 2), can potentially extend settling time of particles in this basin and/or bottom currents can potentially lead to lake floor scouring of debris.

FIGURE 6. Main sub-basin roughness and hardness maps, generated from E1 and Peak Sv acoustic backscatter values. Smooth (A), rough (B), soft (C) and hard (D) are shown, with boxes overlain to show smooth hard returns, interpreted to be bare ice. In areas of very thick sediment cover, like the older southern region of Spillway, bottom deepening is expected to be minimal, although expansion can continue towards the north and west, exploiting weaknesses (cracks) in the terrain.



In the Main sub-basin, despite older and younger regions, deepening is continuing at the highest rate in Spillway Lake. More information is needed, in the form of seismic or radar survey, to better quantify debris thickness and to detect the presence of bare ice in this region, while current meters set at depth can be used to quantify the flow associated with englacial and subglacial inputs. Higher resolution multi-beam sonar surveys could prove useful in mapping subaqueous ice cliffs in the vicinity of calving ice walls surrounding the eastern part of the Main sub-basin. In view of the danger from large waves associated with calving during the measurements, unmanned remotely steerable sensor platforms offer advantages for future survey work, beginning in 2016-17.

#### REFERENCES

- [1] Benn, D.I., Wiseman, S., and K.A. Hands, (2001), Growth and drainage of supraglacial lakes on the debris-mantled Ngozumpa Glacier, Khumbu Himal, Nepal, *Jour. Glac.*, 47, 626-638.
- [2] Benn, D.I., Bolch, T., Hands, K., Gulley, J., Luckman, A., Nicholson, L.I., Quincey, D., Thompson, S., Toumi, R., and S. Wiseman, (2012), Response of debris-covered glaciers in the Mt. Everest region to recent warming, and implications for outburst flood hazards. *Earth-Science Reviews*, 114, 156-174.
- [3] Chikita, K.A., Jha, J., and T. Yamada, (1999), Hydrodynamics of a supraglacial lake and its effect on the basin expansion: Tsho Rolpa, Rolwaling Valley, Nepal Himalaya. *Arctic, Antarctic, and Alpine Research*, 31, 58-70.
- [4] Chivers R.C., Emerson N. and D.R. Burns, (1990), New acoustic processing for underway surveying. *The Hydrographic Journal*, 56, 8-17.
- [5] Kadota, T., (1994), Report for the field investigation on the Tsho Rolpa glacier lake, Rolwaling Valley, February 1993-June 1994. WECS Report. N551.489 KAD.
- [6] Kloser R.J., Bax N.J., Ryan T., Williams A., and B.A. Barker, (2001), Remote sensing of seabed types in the Australian Southeast Fishery; development and application of normal-incident acoustic techniques and associated ground truthing. *Marine and Freshwater Research*, 52, 4475-4489.
- [7] Komori, J., (2008), Recent expansion of glacial lakes in Bhutan Himalayas. *Quaternary International*, 184, 177-186.
- [8] Kraus, H., (1975), An energy balance model for ablation in mountainous areas. *IAHS Publ.* 104 (Symposium at Moscow 1971 - Snow and Ice), 74-82.
- [9] Nakawo, M. and G.J. Young, (1981), Field experiments to determine the effect of a debris layer on ablation of glacier ice. *Ann. Glaciol.*, 2, 85-91.
- [10] Nicholson, L.A., and D.I. Benn, (2006), Calculating ice melt beneath a debris layer using meteorological data. *Jour. Glac.*, 52 (178), 463-470.
- [11] Quincey, D.J., Richardson, S.D., Luckman, A., Lucas, R.M., Reynolds, J.M., Hambrey, M.J., and N.F. Glasser, (2007), Early recognition of glacial lake hazards in the Himalaya using remote sensing datasets. *Global and Planetary Change*, 56, 137-152.
- [12] Reynolds, J.M., (2000), On the formation of supraglacial lakes on debris-covered glaciers. Symposium at Seattle 2000 - Debris Covered Glaciers: International Association of Hydrological Sciences Publication, 264, pp. 153-161.
- [13] Richardson, S.D., and J.M. Reynolds, (2000), An overview of glacial hazards in the Himalayas. *Quaternary International*, 65(6), 31-47.
- [14] Sakai, A., Takeuchi, N., Fujita, K., and M. Nakawo, (2000b), Role of supraglacial ponds in the ablation process of a debris-covered glacier in the Nepal Himalayas. Symposium at Seattle 2000 - Debris Covered Glaciers: International Association of Hydrological Sciences, 264, pp. 119-130.
- [15] Sakai, A., Nishimura, K., Kadota, T., and T. Takeuchi, (2009), Onset of calving at supraglacial lakes on debris-covered glaciers of the Nepal Himalaya. *Jour. Glac.*, 55(193), 909-917.

TRACKING SUPRAGLACIAL LAKE CHANGES ON NGOZUMPA GLACIER, NEPAL

- [16] Shrestha, A.B., Wake, C.P., Mayewski, P.A., and J.E. Dibb, (1999), Maximum temperature trends in the Himalaya and vicinity: an analysis based on temperature records from Nepal for the period 1971-94. *Journal of Climate*, 12, 2775-2786.
- [17] Thompson, S., Benn, D.I., Dennis, K., and A. Luckman, (2012), A rapidly growing moraine dammed glacial lake on Ngozumpa Glacier, Nepal. *Geomorphology*, 75, 266-280.
- [18] Yamada, T., (1998), *Glacier Lake and its Outburst Flood in the Nepal Himalaya*. Monograph No. 1. Data Centre for Glacier Research, Japanese Society of Snow and Ice, Japan. 96 pp.

*E-mail address:* Ulyana.Horodyskyj@colorado.edu

DEPARTMENT OF GEOLOGICAL SCIENCES, UNIVERSITY OF COLORADO, BOULDER, COLORADO

# BAND GAP CHARACTERIZATION OF TWO-DIMENSIONAL DAMPED PHONONIC CRYSTALS

ROMIK KHAJEHTOURIAN

**ABSTRACT.** The goal of this study is to introduce damping in two dimensional (2D) phononic crystals (PCs) and investigate its effect. In order to demonstrate the dynamical behavior and damping effects in a PC, a convenient model of four masses in a square lattice connected by sets of springs and dampers, is considered. A brief discussion on generalized Bloch's theorem and the treatment of both viscous and viscoelastic damping is provided. Frequency and damping ratio band structures are generated for models. Special attention is devoted to the quality of band gaps in transition from viscoelastic to viscous damping.

## 1. INTRODUCTION

Phononic crystals have an attractive property which makes them very unique in regards to other materials: the existence of frequency band gaps where acoustic or elastic waves are forbidden to propagate. This is achieved by distributing the constituent materials periodically. By selecting the size, arrangement and type of material, frequency band gaps can be opened to control elastic wave propagation in a specific manner. In many cases, of interest is the effect of damping on the frequency band structure. The dissipative property of some materials is utilized to great effect on structures such as aircraft and ships where engine noise and vibration are detrimental to standard operation. In damped PCs, the band structure can be generated via generalized Bloch theory. Previous work has been published on analyzing the behavior of band gap materials in engineering structures by considering damping effects. In an early study, a 1D mass-spring-dashpot structure was used to model and the effect of damping, as well as a hypothetical type of damping associated with damped forced modes, was investigated [1]. The subject of another work was the effect of viscous damping on bending wave propagation of a 1D periodic beam structures [2]. Acoustic band gaps have also been studied by considering viscoelastic damping for 3D and 2D lattice [3, 4]. In another work, the vibrational response of 1D and 2D finite periodic lattice structures considering the effects of boundaries, viscous damping, and imperfections was the focus [5]. The next venues explored included the analytical derivations of the dissipation relations in a 1D viscoelastic lattice [6]. The transmission of acoustic waves through viscoelastic 2D PC structures also has been investigated experimentally and theoretically using the finite difference time-domain method [7]. Recently, the theory of wave dispersion in damped elastic periodic materials was introduced and the effects of proportional Rayleigh damping on the band structure was considered [8]. In another work, wave dispersion's theoretical equations were derived for 1D damped PC and 2D continuum

---

*Date:* August 8, 2015.

*Key words and phrases.* Phononic Crystal, Band Structure, Damping.

damped elastic periodic materials while considering both proportional and general viscous damping [9]. Most recently, equations for the 1D viscoelastic damped PCs and acoustic metamaterials (AMs) were formulated in Ref. [10]. In this paper, we extend the concept of the 1D damped PC to obtain a model for 2D damped PC.

## 2. DAMPED TWO DIMENSIONAL PHONONIC CRYSTAL

In this study, a lumped mass model made of four masses in a square arrangement connected by springs and damping elements is considered (Fig. 1). The set of homogeneous differential equations describing the motion of each mass in the 2D damped PC model by accounting periodicity of the unit cell are easy to derive.

**2.1. Generalized Bloch's theorem.** In order to apply Bloch's theorem on damped periodic structures, both an imaginary component for temporal oscillation and a real component that incorporates temporal attenuation should be considered. To do so, a generalized form of Bloch's theorem which has complex root  $\mu$  in the temporal component is considered as

$$\mathbf{u}(\mathbf{x}, \boldsymbol{\kappa}; t) = \tilde{\mathbf{u}}(\mathbf{x}, \boldsymbol{\kappa}) e^{i\boldsymbol{\kappa}\mathbf{x}} e^{\lambda t}, \quad (2.1)$$

where  $\mathbf{u} = \{u, v\}$  is the displacement field,  $\tilde{\mathbf{u}}$  is the displacement Bloch function,  $\mathbf{x} = \{x, y\}$  is the position vector,  $\boldsymbol{\kappa} = \{\kappa_x, \kappa_y\}$  is the wavevector, and  $i = \sqrt{-1}$ . Generalized Bloch's theorem for the mass  $m_{p,q}$ , located at  $p$  and  $q$  in the  $x$  and  $y$  direction within the  $(p+n, q+m)$ th unit cell is discretized as

$$\mathbf{u}_{p+n, q+m} = \bar{\mathbf{U}}_{p,q} e^{i(\kappa_x x + \kappa_y y + n\kappa_x a + m\kappa_y a)} e^{\lambda t}, \quad (2.2)$$

where  $a$  is the length of unit cell,  $\bar{\mathbf{U}}_{p,q} = \{U_{p,q}, V_{p,q}\}$ , and  $m$  and  $n$  denote the unit cell in  $x$  and  $y$  directions respectively. Applying Eq. (2.2) into the equations of motion provides a complex eigenvalue problem for the PC as

$$[\lambda^2 \mathbf{M} + \lambda \mathbf{C}(\boldsymbol{\kappa}) + \mathbf{K}(\boldsymbol{\kappa})] \tilde{\mathbf{u}} = \mathbf{0}, \quad (2.3)$$

where  $\mathbf{M}$ ,  $\mathbf{C}(\boldsymbol{\kappa})$  and  $\mathbf{K}(\boldsymbol{\kappa})$  are defined as the mass, damping, and stiffness matrices that are found by sorting the equations of motions into matrix form, using the coefficient  $\lambda$ .

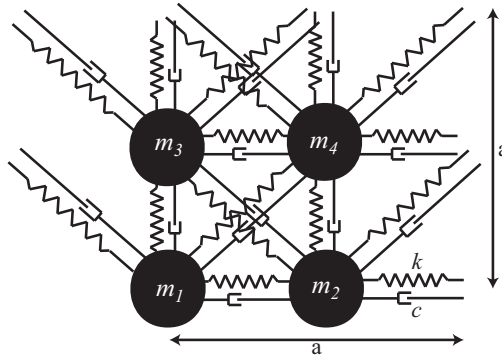


FIGURE 1. Lumped parameter unit cell model of a phononic crystal.

**2.2. Treatment of Viscous Damping.** For proportional damping, the equations of motion can be uncoupled by applying modal coordinates, while in general damping, these coordinates are not diagonalizable. In consequence, the system will remain coupled and complicated to solve. Bloch state-space formulation is a powerful tool to treat the modeled damped system and provide the complex eigenvalues  $\lambda_s$ ,  $s = 1, \dots, 8$ . This formulation is based on a transformation of variables,  $\bar{\mathbf{Y}} = [\dot{\bar{\mathbf{U}}}, \bar{\mathbf{U}}]^T$ , and is given by

$$\begin{bmatrix} \mathbf{0} & \mathbf{M} \\ \mathbf{M} & \mathbf{C}(\kappa_x, \kappa_y) \end{bmatrix} \dot{\bar{\mathbf{Y}}} + \begin{bmatrix} -\mathbf{M} & \mathbf{0} \\ \mathbf{0} & \mathbf{K}(\kappa_x, \kappa_y) \end{bmatrix} \bar{\mathbf{Y}} = \mathbf{0}. \quad (2.4)$$

By applying the solution of  $\bar{\mathbf{Y}} = \tilde{\mathbf{Y}}e^{\gamma t}$ , where  $\gamma$  and  $\tilde{\mathbf{Y}}$  correspond to eigenvalues and eigenvectors, the first-order eigenvalue problem can be formed as

$$\left( \begin{bmatrix} \mathbf{0} & \mathbf{M} \\ \mathbf{M} & \mathbf{C}(\kappa_x, \kappa_y) \end{bmatrix} \gamma + \begin{bmatrix} -\mathbf{M} & \mathbf{0} \\ \mathbf{0} & \mathbf{K}(\kappa_x, \kappa_y) \end{bmatrix} \right) \tilde{\mathbf{Y}} = \mathbf{0}. \quad (2.5)$$

Solving this equation results in eight complex conjugate pairs of eigenvalues  $\gamma$ . Among these pairs, only eigenvalues with positive imaginary part are physically meaningful,

$$\gamma_s = -\zeta_s \omega_s(\kappa_x, \kappa_y) + i\omega_{d_s}(\kappa_x, \kappa_y), \quad s = 1, 2, \dots, 8, \quad (2.6)$$

where  $\omega_s$  is the resonant frequency and  $\omega_{d_s}$  is the damped frequency as function of wavevector and can be found via

$$\omega_{d_s}(\kappa_x, \kappa_y) = \text{Im}[\gamma_s(\kappa_x, \kappa_y)], \quad s = 1, 2, \dots, 8, \quad (2.7)$$

and  $\zeta_s$ , the corresponding wavevector-dependent damping ratio is

$$\zeta_s(\kappa_x, \kappa_y) = \frac{\text{Re}[\gamma_s(\kappa_x, \kappa_y)]}{\text{Abs}[\gamma_s(\kappa_x, \kappa_y)]}, \quad s = 1, 2, \dots, 8. \quad (2.8)$$

**2.3. Treatment of Viscoelastic Damping.** For the case of viscoelastic damping, each of the dashpots in Fig. 1 are replaced with Maxwell elements which is a purely viscous damper and a purely elastic spring connected in series as illustrated in Fig. 2. Maxwell elements account for the energy dissipation and energy storage of the system via the dashpot and spring respectively. To treat viscoelasticity, Boltzmann's hereditary theory which relates the damping force to the past history of motion by a convolution integral over a kernel function  $G(t)$  is used. The kernel function for Maxwell element is

$$G(t) = ke^{-\frac{k}{c}t}H(t) = \mu_1 e^{-\mu_2 t}H(t). \quad (2.9)$$

By assuming  $\mu_1 = \mu_2 = \mu$ , a mathematically tractable form of the kernel function,  $G(t) = \mu e^{-\mu t}H(t)$ , is considered and an internal variable  $\bar{\mathbf{V}}(t)$  is defined,

$$\bar{\mathbf{V}}(t) = \int_0^t \mu e^{-\mu(t-\tau)} \dot{\bar{\mathbf{U}}}(\tau) d\tau. \quad (2.10)$$

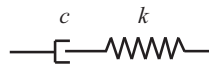


FIGURE 2. Maxwell element.

Differentiating this variable results in

$$\dot{\bar{\mathbf{V}}}(t) + \mu \bar{\mathbf{V}}(t) - \mu \dot{\bar{\mathbf{U}}}(t) = \mathbf{0} \quad (2.11)$$

Equation (2.11) is multiplied by  $\mathbf{C}(\kappa_x, \kappa_y)$  and divided by  $\mu^2$  which yields

$$\frac{\mathbf{C}(\kappa_x, \kappa_y)}{\mu^2} \dot{\bar{\mathbf{V}}} + \frac{\mathbf{C}(\kappa_x, \kappa_y)}{\mu} \bar{\mathbf{V}} - \frac{\mathbf{C}(\kappa_x, \kappa_y)}{\mu} \dot{\bar{\mathbf{U}}} = \mathbf{0}. \quad (2.12)$$

Utilizing Eq. (2.12), a state vector of  $\bar{\mathbf{Z}} = [\dot{\bar{\mathbf{U}}} \ \bar{\mathbf{U}} \ \bar{\mathbf{V}}]^T$ , and the Bloch state-space formulation for viscous damping in Eq. (2.4), a new Bloch state space form is constructed

$$\begin{bmatrix} \mathbf{0} & \mathbf{M} & \mathbf{0} \\ \mathbf{M} & \mathbf{C}(\kappa_x, \kappa_y) & -\frac{\mathbf{C}(\kappa_x, \kappa_y)}{\mu} \\ \mathbf{0} & -\frac{\mathbf{C}(\kappa_x, \kappa_y)}{\mu} & \frac{\mathbf{C}(\kappa_x, \kappa_y)}{\mu^2} \end{bmatrix} \dot{\bar{\mathbf{Z}}} + \begin{bmatrix} -\mathbf{M} & \mathbf{0} & \mathbf{0} \\ \mathbf{0} & \mathbf{K}(\kappa_x, \kappa_y) & \mathbf{0} \\ \mathbf{0} & \mathbf{0} & \frac{\mathbf{C}(\kappa_x, \kappa_y)}{\mu} \end{bmatrix} \bar{\mathbf{Z}} = \mathbf{0}. \quad (2.13)$$

Similar to viscous damping, a solution of the form  $\mathbf{Z} = \tilde{\mathbf{Z}}e^{\gamma t}$  is assumed for Eq. (2.13),

$$\left( \begin{bmatrix} \mathbf{0} & \mathbf{M} & \mathbf{0} \\ \mathbf{M} & \mathbf{C}(\kappa_x, \kappa_y) & -\frac{\mathbf{C}(\kappa_x, \kappa_y)}{\mu} \\ \mathbf{0} & -\frac{\mathbf{C}(\kappa_x, \kappa_y)}{\mu} & \frac{\mathbf{C}(\kappa_x, \kappa_y)}{\mu^2} \end{bmatrix} \gamma + \begin{bmatrix} -\mathbf{M} & \mathbf{0} & \mathbf{0} \\ \mathbf{0} & \mathbf{K}(\kappa_x, \kappa_y) & \mathbf{0} \\ \mathbf{0} & \mathbf{0} & \frac{\mathbf{C}(\kappa_x, \kappa_y)}{\mu} \end{bmatrix} \right) \tilde{\mathbf{Z}} = \mathbf{0}. \quad (2.14)$$

As before, the solutions are of the form in Eq. (2.6) and a set of eigenvalues,  $\gamma_{s^*}, s^* = 1, \dots, 24$ , are obtained mathematically. Of these solutions, eight roots appearing as physically represent the modes of damped wave propagation. One can recover Eq. (2.4) from Eq. (2.13) by limiting  $\mu \rightarrow \infty$ . Indeed, high values of  $\mu$  better represent viscous behavior, whereas low values of  $\mu$  represent more viscoelastic behavior.

### 3. RESULTS

For the PC modeled in Fig. 1, dispersion curves have been generated with the following properties:  $m_1/m_2 = m_1/m_3 = m_2/m_4 = 3, \omega = \sqrt{km_1} = 10$  rad/s,  $\beta = c/m_1 = 2$  1/s. Plot in Fig. 3 shows frequency and damping ratio band structures for a undamped, viscoelastically  $\mu = 50$ , and viscous  $\mu = 10^5$  damped 2D PC band structure. Springs and damping elements are assumed to be the same over the model (Case A). The frequency band diagram shows that in relation to the un-damped PC modes, there is a drop in the viscous damped PC while in the viscoelastic damped PC there is a rise. This phenomena can be seen in Fig. 5 which shows that for the viscous region (right hand side of transition region), band gaps are lower than un-damped PC and for viscoelastic region (left hand side of transition region), they are greater or the same as an un-damped PC. We have defined a region as the transition region (Orange shaded), which is defined via the range of relaxation parameter  $\mu$ , where the band gaps of the un-damped PC cross those of the damped PC. The damping ratio band diagram in Fig. 3b corresponds very well with the frequency band structure; the damping ratio for the viscoelastic damped PC is much smaller than that of the viscous damped PC.

In a damped PC, the rate of the descent and ascent of the branches depend on the relaxation parameter  $\mu$ , and frequency. When transitioning from viscoelastic to viscous damping, the band structure becomes sensitive to relaxation parameter; for lower frequency branches such as the acoustic, the rate of change is slow, in the first few optical

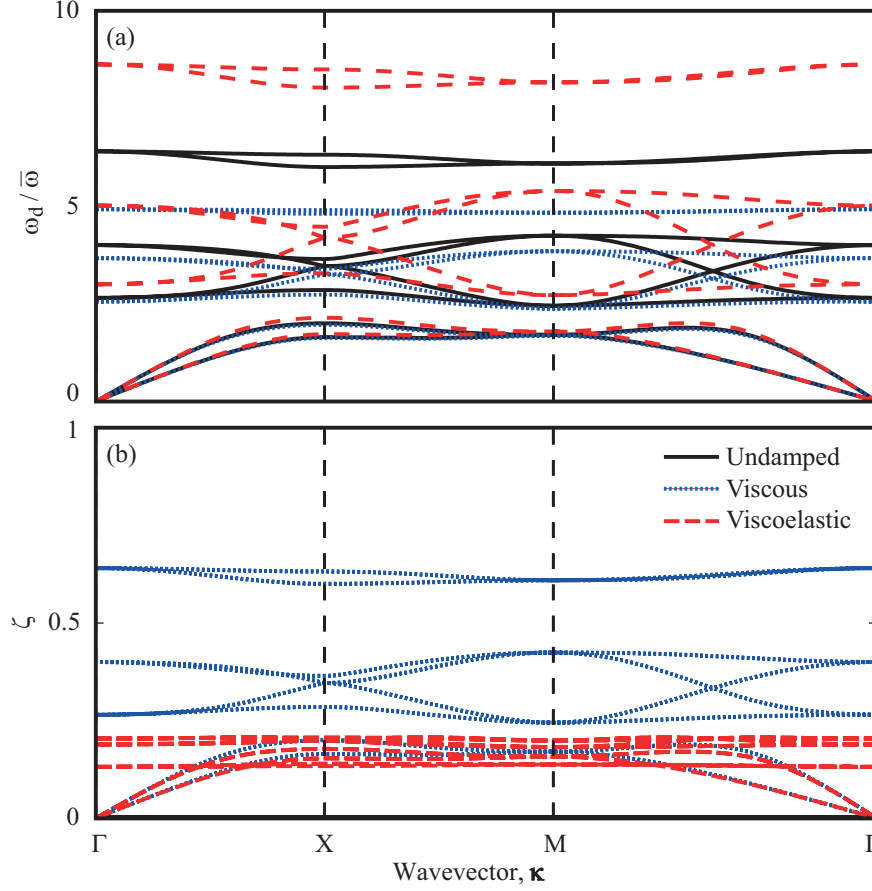


FIGURE 3. Band structure for a periodic unit cell, Case A. (a) Frequency, (b) damping ratio band structure for un-damped, viscous damped, and viscoelastic damped PC.

branches it is slightly faster, and for higher optical branches it is significantly faster. This phenomena can be seen in Fig. 4 for Case A where the second, third, sixth and seventh branches' band gap extremes for different  $\mu$  are plotted with solid thick lines, and band gaps for an un-damped PC not dependent on  $\mu$  is plotted with dash-dot lines for comparison. There are regions of  $\mu$  where the branches act opposite of each other, such as where the seventh optical branch ascends and the sixth branch is descends for  $\mu$  from 80 to 100 (Green shaded). In general, the trend of modes are not the same for the whole of relaxation parameters. Also of note, the width of band gap in viscoelastic damped PC is greater than that of the viscous damped PC.

In the viscoelastic damping section, we were able to recover viscous damping by increasing the amount of  $\mu$  in Bloch's state space transformation system; this can be seen clearly in Fig. 4. If  $\mu$  is such that  $C(\kappa) + 1/\mu C(\kappa) \approx C(\kappa)$ , then dominantly viscous behavior can be expected. For our model, we found  $\mu > 10^4$  reflects viscous behavior well. We chose  $\mu = 10^5$  (blue dot) to represent viscous damping and  $\mu = 50$  (red dash) for viscoelastic damping in our generated plots. On top of all of this

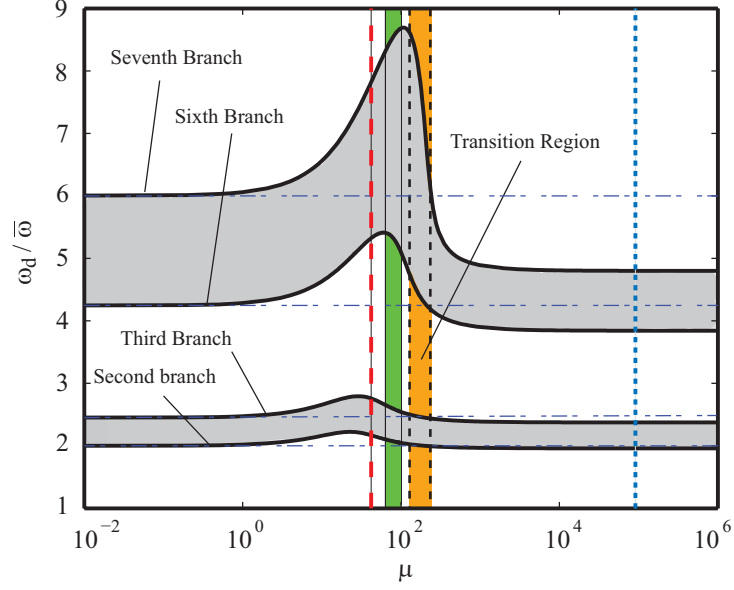


FIGURE 4. Band gap size vs. relaxation parameter.

information extracted from Fig. 4. We found the peaks of band gaps follow a nonlinear trend.

Figure 5 corresponds to the system where springs in the horizontal direction are neglected (Case B). These figures provide a clear picture of the difference in behavior of viscous and viscoelastic damping within a PC. We observed that for a fixed damping intensity  $\beta$ , and select  $\mu$ 's, the optical branches for viscous damping drop while for viscoelastic damping they rise. Also, we can see the cut off phenomena where lower modes cannot cover the whole Brillouin zone and band gaps with respect to wavevector are created. For Case B, the third and fourth branches open band gaps with respect to wavevector which correspond very well to damping ratios for same modes which rise to a maximum. It was also noticed that three different phenomena occurred for the undamped, viscous and viscoelastic damped PC due to the defect. Also it is noticed that because of defect in Case B, three different phenomena happens to un-damped, viscous and viscoelastic damped PC. By focusing on the  $[\Gamma X]$  wavevector, for un-damped PC, the first band gap between the acoustic and optical branches is closed due to perfect folding of the acoustic branch. For the viscous damped PC, this defect in unit cell resulted in cut off, and for the viscoelastic damped PC, caused a band gap due to local resonance.

#### 4. CONCLUSION

In this study, we started with equations of motions for a 2D PC in a square lattice and selected a combination of four masses for Case A and neglected horizontally arranged springs for Case B. We used generalized Bloch's theorem to account for the temporal attenuation behavior of damping. Then, for viscous and viscoelastic damping we reviewed Bloch's state space transformations. We solved this set of equations and extracted eigenvalues, that provided the damped frequencies and damping ratios.

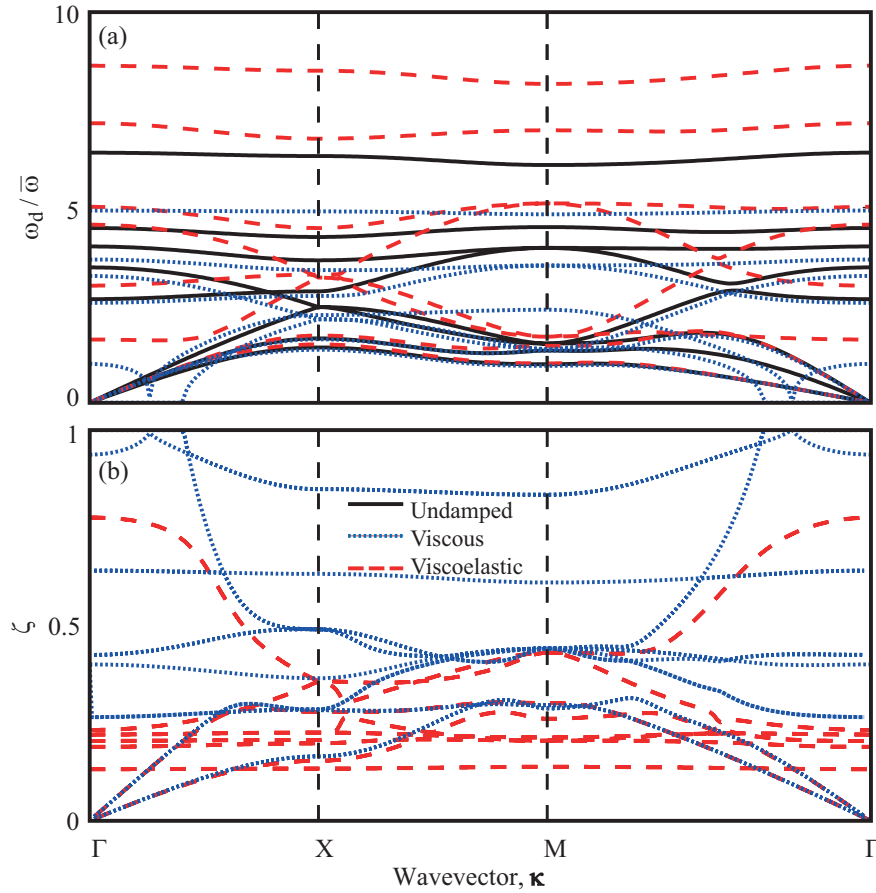


FIGURE 5. Band structure for a periodic unit cell, Case B. (a) Frequency, (b) damping ratio band structure for un-damped, viscous damped, and viscoelastic damped PC.

We studied frequency and damping ratio band structures for both Case A and B, and investigated the band gaps sizes for different relaxation parameters. We saw different behaviors for branches due to different values of  $\mu$  and the defect introduced to the PC, caused different effects of damping in different directions. Increasing the size of the band gap is a desirable feature for many applications such as vibration and noise reduction and isolation. On the other hand understanding the relation between the damping effect and unit cell anisotropy will provide a useful tool to control and tailor application specific solutions for wave guiding and energy flow in materials.

#### REFERENCES

- [1] DJ. Mead, "A general theory of harmonic wave propagation in linear periodic systems with multiple coupling," *Journal of Sound and Vibration*, **27**, 235-260 (1973).
- [2] E. Tassily, "Propagation of bending waves in a periodic beam," *International journal of engineering science*, **25**, 85-94 (1987).
- [3] R. Sprik, and H. W. Gerard, "Acoustic band gaps in composites of solids and viscous liquids." *Solid state communications*, **106**, 77-81 (1998).

ROMIK KHAJEHTOURIAN

- [4] X. Zhang, Z. Liu, J. Mei, and Y. Liu, "Acoustic band gaps for a two-dimensional periodic array of solid cylinders in viscous liquid." *Journal of Physics: Condensed Matter*, **15**, 8207 (2003).
- [5] J.S. Jensen, "Phononic band gaps and vibrations in one- and two-dimensional mass-spring structures." *Journal of Sound and Vibration*, **266**, 1053-1078 (2003).
- [6] W. Wang, J. Yu, and Z. Tang, "General dispersion and dissipation relations in a one-dimensional viscoelastic lattice." *Physics Letters A*, **273**, 5-8 (2008).
- [7] B. Merheb, P. A. Deymier, M. Jain, M. Alohyna-Lesuffleur, S. Mohanty, A. Berker, and R. W. Greger, "Elastic and viscoelastic effects in rubber/air acoustic band gap structures: A theoretical and experimental study." *Journal of Applied Physics*, **104**, 064913 (2008).
- [8] M. I. Hussein, "Theory of damped Bloch waves in elastic media." *Physical Review B*, **80**, 212301 (2009).
- [9] M. I. Hussein, and M. J. Frazier "Band structure of phononic crystals with general damping." *Journal of Applied Physics*, **108**, 093506 (2010).
- [10] M. I. Hussein, and M. J. Frazier "Damped Phononic Crystals and Acoustic Metamaterials." *Acoustic Metamaterials and Phononic Crystals*. Springer Berlin Heidelberg, 201-215 (2013).

*E-mail address:* r.k@colorado.edu

DEPARTMENT OF AEROSPACE ENGINEERING SCIENCES, UNIVERSITY OF COLORADO BOULDER,  
BOULDER, COLORADO 80309, USA

# THE GEOBIOLOGY OF SULFUR SPRINGS AT BORUP FIORD PASS

GRAHAM E. LAU

**ABSTRACT.** Sulfur is one of the most abundant elements in the universe and is essential for life as we know it. Characterizing the role of biology in the geochemical cycling of sulfur from regional to global scales is important for the future exploration of other worlds in our solar system and beyond. In this article, we present research on microbial sulfur cycling within a supraglacial sulfur spring system in the Canadian High Arctic. Specifically, we will discuss what we know and have yet to learn about the biological and abiotic processes that are responsible for cycling sulfur at this field site.

## 1. INTRODUCTION

Borup Fiord Pass, located on Ellesmere Island in the Canadian High Arctic, presents a unique environmental system where discharges of spring fluids on glacial ice source the deposition of sulfur-rich materials, including gypsum and elemental sulfur ( $S^0$ ). The deposition of  $S^0$  causes visibly yellow staining on the ice. It has been shown that the springs and associated deposits host diverse microbial assemblages for which sulfur metabolism is a key source of energy transduction [13] [6] [4]. The metabolism of sulfur by these microorganisms is hypothesized to play a key role in the deposition of the sulfur-rich deposits, perhaps through processes including the biomineralization of  $S^0$ . The potential for the formation and preservation of unique sulfur biosignatures makes this sulfur spring system at Borup Fiord Pass an ideal target for studying microbial sulfur cycling in cold environments. My graduate research has been targeted at characterizing the sulfur from the deposits to determine the role that biology plays in cycling this sulfurous material. Since this site represents a sulfur-dominated system where subsurface fluids are expressed at the surface of icy material, Borup Fiord Pass is also considered an ideal analog for astrobiological investigations of other worlds, such as Mars and Europa.

## 2. THE IMPORTANCE OF SULFUR ON EARTH AND BEYOND

Sulfur is a vital element for life as we know it: sulfur is the 6th most abundant element on Earth [7]; there is a large variation in chemical oxidation states that sulfur can assume (from 2− in sulfides to 6+ in sulfates); sulfur is of critical importance for biomolecule production (e.g. cysteine, methionine, biological sulfates); and sulfur is important for many microbial metabolisms. For instance, sulfur reduction, sulfur oxidation, and sulfur disproportionation are all utilized by various forms of life on this planet, driving transitions in sulfur speciation through metabolic processes (see [1] for a review). Such sulfur metabolisms are amongst the oldest biological processes to leave

---

*Date:* August 8, 2015.

*Key words and phrases.* sulfur, supraglacial sulfur spring, canadian high arctic, borup fiord pass, astrobiology.

GRAHAM E. LAU

FIGURE 1. Graham Lau poses on a cliff overlooking Borup Fiord Pass valley in the Canadian High Arctic.

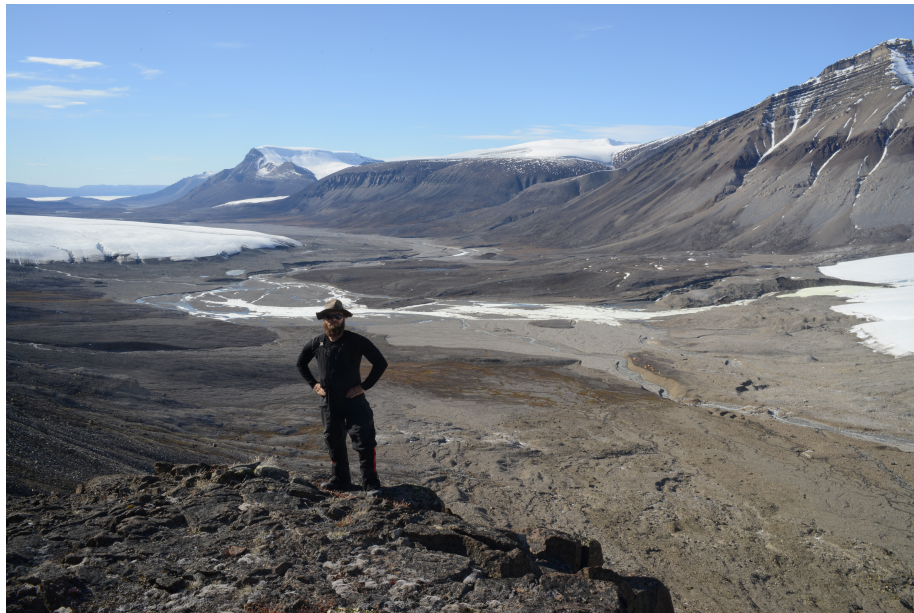


FIGURE 2. Graham Lau walking into a glacial cavern at Borup Fiord Pass.



traces in the rock record. For instance, isotopic signatures in pyrite granules from 3.47 to 3.49 Ga sedimentary units in North Pole, Australia, have been implicated as potential signatures of ancient microbial metabolisms [11] [12]. These isotopic signatures are thus potentially the oldest evidence of specific biological metabolisms that have been gleaned from the geologic record. Determination of the ancestry and importance of sulfur metabolisms for life on Earth can also be gleaned from analyses of genetic material in modern organisms. Sulfur metabolisms are abundant across all three domains of life, however phylogenies for the dissimilatory sulfite reductase (*dsr*) gene appear to show that this gene and the associated metabolic activity pre-dates the evolutionary divergence of Bacteria and Archaea [9].

Due to the importance of sulfur for life as we know it, investigations of the geo-biological cycling of sulfur on Earth are necessary for assessing the role of sulfur in potential living systems on other worlds. For instance, Domagal-Goldman et al. (2011) have proposed that biogenic sulfur gases acting on planetary atmospheres may be capable of providing spectroscopic evidence of active biospheres on extrasolar planets [3]. Sulfur biology may also have had a role to play if life ever originated and evolved in other regions of our own solar system. Mars and Europa, two current targets in the astrobiological investigation of our solar system, may have had past or even present sulfur metabolisms and/or interactions of living processes with sulfur chemistry. For instance, sulfates of calcium and magnesium have been identified globally on Mars through remote sensing, and ferric iron sulfates have also been detected in certain Martian localities through robotic exploration (see [8] for review). The future exploration of Mars will likely include work to determine whether biological mechanisms have been involved in processing these sulfur materials on that planet.

It is now widely accepted that Europa, a moon of Jupiter, likely has a subsurface ocean under its thick, icy crust. It's currently unknown if sulfur plays an important role within this ocean, however sulfur has been detected on the icy surface of Europa. Current models for the origin of this sulfur include exogenous delivery as well as sourcing from the subsurface ocean [14] [2]. If sulfur is transferred between the surface and the ocean of Europa, then it will be important to know what sulfur at the surface and near-surface on Europa can tell us about potential geochemical and biological processes on that world. The upcoming orbiting spacecraft mission in development by NASA, known temporarily as the Europa Multi Flyby Mission, is scheduled to launch sometime around 2020 and will provide spectroscopic analyses of the surface of Europa, including analyses of the sulfur on the surface. Furthermore, it is likely that a landing spacecraft mission will be sent to Europa in the coming decades [10]. Characterizations of sulfur signatures from biological and geochemical processes on Earth will be important for such upcoming missions to the icy world of Europa.

Although the physicochemical dynamics of Europa's ocean are likely far different from those in the subsurface below the Borup Fiord Pass glacier, the potential for geo-biological sulfur cycling within Europa and the likelihood of future astrobiological investigations on that moon demand that processes affecting the production and preservation of biosignatures in cold, sulfur-dominated environments on Earth be better characterized. Investigations at Borup Fiord Pass will thus highlight geobiological sulfur cycling relevant to Europa, especially since Borup Fiord Pass presents a system where the subsurface and surface are connected by fluids that are tunneled through glacial ice.

Furthermore, the relationship between communities of microorganisms and sulfur cycling at this unique Arctic site will bear upon questions of the history of life on Earth as well as for the potential discovery of extraterrestrial life beyond our solar system.

### 3. BORUP FIORD PASS IN A NUTSHELL

Borup Fiord Pass is a valley located at  $81^{\circ}01'N$ ,  $81^{\circ}35'W$  on Ellesmere Island in the Canadian High Arctic. Sulfur-rich springs and associated deposits of gypsum and  $S^0$  occur on the southern edge of a glacier within this valley. Visibly yellow staining of the glacier's surface from  $S^0$  has been seen to cover as much as  $2,000\text{ m}^2$ , although the extent of sulfur deposition varies from year-to-year [6]. The springs which deposit the sulfur are alkaline (pH values of 8 to 9) and have elevated levels of dissolved  $H_2S$  (up to  $4.4\text{ mM}$ ) and  $SO_4^{2-}$  (up to  $27.9\text{ mM}$ ; [4] [6]). Grasby and colleagues (2003) used stable-isotope analyses to determine that the springs are likely sourced from glacial meltwater that has been subsided and reacted with local geological units in the subsurface before returning to the surface and emerging onto the glacier [6]. Elevated levels of  $H_2S$  in spring fluids likely occur due to biological reduction of sulfate from local anhydrite beds in the subsurface. Once the fluids emerge at the surface, the sulfide is then oxidized to  $S^0$  and eventually to sulfate, though some sulfur deposits have been found at the site that appear to have been stable over periods of years. The processes through which such large accumulations of  $S^0$  form and then remain stable at the glacier's surface are not yet constrained, though microbial processes are considered to be a potentially important factor.

FIGURE 3. Graham Lau standing on a glacier where yellow elemental sulfur has been deposited on the ice.



Investigations of microbial populations at Borup have identified diverse populations through analyses of the 16S rRNA gene. For instance, the emerging spring fluids appear dominated by *Ralstonia* sp. and *Burkholderia* sp. while surface sulfur deposits show population dominance by *Flavobacteria* sp. A metagenome analysis of a downstream sulfur deposit showed that *Flavobacteria* sp. dominated the surface of the deposit while *Sulfurovum* sp. and *Sulfuricurvum* sp. dominated the greater deposit to a depth of 15 cm [13]. More recent investigations of samples collected in 2014 appear to also show the importance of *Flavobacteria* sp., *Sulfurovum* sp., and *Sulfuricurvum* sp., however *Sulfurimonas* sp. also appears dominant in ices that form from the spring fluids (data not yet published).

One of the more surprising findings in regards to the Borup Fiord Pass microbiology has been the observation of structures of biomineralized elemental sulfur within laboratory cultures. These lab-grown structures include apparently hollow sheaths (approximately 1  $\mu\text{m}$  diameter) decorated with  $S^0$  as well as long carbonaceous filaments (<100 nm diameter), both observed in association with globules of  $S^0$ . Work by Wright (2012) suggests that *Gillisia* sp., a member of the order Flavobacteriaceae, is the primary organism involved in the mineralization of elemental sulfur in these lab cultures [13]. It is not yet known if these structures are formed through direct or indirect biomineralization pathways. Furthermore, it is uncertain whether these structures are formed ubiquitously in the field or whether such processes may be relevant to the stabilization of  $S^0$  at the glacier's surface. Julie Cosmidis, a postdoc working in the Templeton Lab at CU Boulder, is currently working on characterizing these potential sulfur biominerals from culture experiments.

My work thus far as a graduate student has focused on characterizing the sulfur material collected from Borup Fiord Pass. I have been using instrumental techniques such as x-ray diffraction (XRD) and Raman spectroscopy for mineralogical analysis, infrared (IR) spectroscopy and x-ray absorption spectroscopy (XAS) to probe the speciation and possible organic associations of the sulfur, and also scanning and transmission electron microscopy (SEM/TEM) paired with energy dispersive x-ray spectroscopy (EDXS) to identify unique morphological structures within the material. Recently, while investigating a new suite of samples that were collected during our field expedition in 2014, I found that elemental sulfur within the sample is mineralogically expressed in three forms, two of which are not expected to form abiotically in cold environments (data not yet published). Furthermore, I have recently been interrogating unique morphological structures of the sulfur within the 2014 samples; these structures may be indicative of biological processing of the materials.

#### 4. CONCLUSION

The continued characterization of microbes and sulfurous materials from the spring system at Borup Fiord Pass will build upon our knowledge of the relationships between biological processes and expressions of unique sulfur chemistry. Due to the importance of sulfur for life as we know it, such analyses will allow us to better understand life's evolving role with regard to the sulfur chemistry on Earth through time. Furthermore, this work will be beneficial for future investigations of other worlds in our solar system

FIGURE 4. Yellow bubbles of elemental sulfur form on top of a melt pool at Borup Fiord Pass, Canadian High Arctic.



and beyond. For instance, biosignature characterization at Borup Fiord Pass will be useful for constraining which signs of life may be considered traces in future robotic explorations of Mars and Europa. Through combined biological and instrumental analyses, the processes of microbial sulfur cycling at Borup Fiord Pass will be further resolved to detail how sulfur and living processes are intimately related.

#### REFERENCES

- [1] Clark, Benton C. 1981. "Sulfur: Fountainhead of Life in the Universe?" In *Life in the Universe*, edited by J. Billingham, 47-60. Cambridge: MIT Press.
- [2] Dalton, J.B., T. Cassidy, C. Paranicas, J.H. Shirley, L.M. Prockter, and L.W. Kamp. 2013. "Exogenic Controls on Sulfuric Acid Hydrate Production at the Surface of Europa." *Planetary and Space Science* 77 (March). Elsevier: 45D63. doi:10.1016/j.pss.2012.05.013.
- [3] Domagal-Goldman, Shawn D, Victoria S Meadows, Mark W Claire, and James F Kasting. 2011. "Using Biogenic Sulfur Gases as Remotely Detectable Biosignatures on Anoxic Planets." *Astrobiology* 11 (5): 419D41. doi:10.1089/ast.2010.0509.
- [4] Gleeson, D F, C Williamson, S E Grasby, R T Pappalardo, J R Spear, and a S Templeton. 2011. "Low Temperature S(0) Biomineralization at a Supraglacial Spring System in the Canadian High Arctic." *Geobiology* 9 (4): 360D75. doi:10.1111/j.1472-4669.2011.00283.x.
- [5] Gleeson, Damhnait F, R T Pappalardo, M S Anderson, S E Grasby, R E Mielke, K E Wright, and a S Templeton. 2012. "Biosignature Detection at an Arctic Analog to Europa" *Astrobiology* 12 (2): 135D50. doi:10.1089/ast.2010.0579.

FIGURE 5. Graham Lau standing on a glacier on Ellesmere Island.



FIGURE 6. Graham Lau sitting on Permian rocks at Borup Fiord Pass, Canadian High Arctic.



- [6] Grasby, Stephen E, Carlton C Allen, Teresa G Longazo, John T Lisle, Dale W Griffin, and Benoit Beauchamp. 2003. "Supraglacial Sulfur Springs and Associated Biological Activity in the Canadian High Arctic-Signs of Life beneath the Ice." *Astrobiology* 3 (3): 583D96. doi:10.1089/153110703322610672.
- [7] Haynes, W M, ed. 2013. *CRC Handbook of Chemistry and Physics*, 94th Edition. Taylor and Francis Limited. <http://www.hbcnetbase.com/>.
- [8] King, P. L., and S. M. McLennan. 2010. "Sulfur on Mars." *Elements* 6 (2): 107D12. doi:10.2113/gselements.6.2.107.

- [9] Loy, Alexander, Stephan Duller, and Michael Wagner. 2008. "Evolution and Ecology of Microbes Dissimilating Sulfur Compounds: Insights from Siroheme Sulfite Reductases." In *Microbial Sulfur Metabolism*, edited by C Dahl and C G Friedrich, 46Ð59. Springer.
- [10] Pappalardo, R.T., S. Vance, F. Bagenal, B.G. Bills, D.L. Blaney, D.D. Blankenship, W.B. Brinckerhoff, et al. 2013. "Science Potential from a Europa Lander." *Astrobiology* 13 (8): 130807073521003. doi:10.1089/ast.2013.1003.
- [11] Philippot, Pascal, Mark Van Zuilen, Kevin Lepot, Christophe Thomazo, James Farquhar, and Martin J Van Kranendonk. 2007. "Early Archaean Microorganisms Preferred Elemental Sulfur, Not Sulfate." *Science (New York, N.Y.)* 317 (5844): 1534Ð37. doi:10.1126/science.1145861.
- [12] Wacey, David, Matt R. Kilburn, Martin Saunders, John Cliff, and Martin D. Brasier. 2011. "Microfossils of Sulphur-Metabolizing Cells in 3.4-Billion-Year-Old Rocks of Western Australia." *Nature Geoscience* 4 (10). Nature Publishing Group: 698Ð702. doi:10.1038/ngeo1238.
- [13] Wright, Katherine E, Charles Williamson, Stephen E Grasby, John R Spear, and Alexis S Templeton. 2013. "Metagenomic Evidence for Sulfur Lithotrophy by Epsilonproteobacteria as the Major Energy Source for Primary Productivity in a Sub-Aerial Arctic Glacial Deposit, Borup Fiord Pass." *Frontiers in Microbiology* 4 (April): 63. doi:10.3389/fmich.2013.00063.
- [14] Zolotov, M Y, and E L Shock. 2003. "Energy for Biologic Sulfate Reduction in a Hydrothermally Formed Ocean on Europa." *Journal of Geophysical Research* 108 (E4): 5022. doi:10.1029/2002JE001966.

*E-mail address:* [Graham.Lau@colorado.edu](mailto:Graham.Lau@colorado.edu)

DEPARTMENT OF GEOLOGICAL SCIENCES, UNIVERSITY OF COLORADO, BOULDER, COLORADO

# COMBINING CFD AND DISTRIBUTED PRESSURE SENSORS FOR WIND SENSING WITH UAS

ROGER J LAURENCE III

**ABSTRACT.** Numerous methods of obtaining wind field measurements exist, including radar, meteorological stations, weather balloons and manned aircraft. While all these methods have their own advantages and disadvantages, unmanned aircraft systems (UAS) are able to combine many of the advantages of the previously mentioned methods into a single system. Currently, one of the best ways to make *in situ* wind velocity measurements from an unmanned aircraft is to employ a multi-hole probe. These probes allow for the creation of high fidelity wind vector maps. With the rise of small UAS, whose airframes can cost an order of magnitude less than the multi-hole probes, it has become clear that an alternative method needs to be developed to help foster widespread wind measurements obtained via sUAS. Additionally, there is significant risk of permanent damage to the probes during a hard landing as many sUAS lack dedicated landing gear.

An alternative to multi-hole probes is currently being investigated. By installing numerous, off the shelf pressure sensors on the surface of the aircraft, both the cost and risk of damage to the wind sensing system is reduced. Earlier CFD simulations led to the sensor locations that best combined pressure predictability and range for both angle of attack and side slip[1]. To test the feasibility of this method of wind sensing, a 2/3 scale model of the Eagle Owl UAS is currently being fabricated. In addition, a nonlinear least squares estimator was investigated as a potential method of estimating the angle of attack and side slip from the measurements obtained by the sensors.

## 1. INTRODUCTION

The initial aircraft chosen for this project is the Eagle Owl UAS because of its simple geometry. This allowed for easier computational fluid dynamics (CFD) simulations and for the manufacture of a scale model for wind tunnel testing. By utilizing CFD software (STAR-CCM+ was the software of choice), the pressure on the surface of the aircraft was analyzed, leading to 10 locations that were deemed “ideal” based on a combination of the pressure range at the location and how well the change in pressure could be predicted.

## 2. CFD

The CAD model of the Eagle Owl can be seen in Figure 4 (a). CFD simulations were performed with an airspeed of 15 m/s, an environmental pressure close to the surface pressure of Boulder, CO, and varying angles of attack ( $\alpha$ ) and side slip ( $\beta$ ). The angle of attack ranged from  $-5^\circ$  to  $15^\circ$ , while the side slip ranged from  $0^\circ$  to  $5^\circ$  (both in  $1^\circ$

---

*Date:* August 8, 2015.

*Key words and phrases.* unmanned aircraft, wind sensing.

increments). For the simulations at each  $(\alpha, \beta)$  used, the pressure<sup>1</sup> at each cell on the surface was obtained. These pressures were then used with the MATLAB *fit* function to create a five degree by five degree polynomial surface fit between the pressure and the flow angles (for all ~180,000 surface points).

One output of interest from the *fit* function is the root mean square error (RMSE), which is a way of telling how well the surface fits to the provided pressure. A simple cost function was used to starting determining suitable locations:

$$J_\alpha = RMSE/P_r \quad (2.1)$$

where  $P_r$  is the pressure range experienced by the surface point and the objective is to minimize  $J_\alpha$ . This cost function lead to locations that had a higher resolution in the determination of  $\alpha$ , but poor resolution in  $\beta$ , so a second cost function was created:

$$J_\beta = - \left( \frac{RMSE - RMSE_l}{RMSE_u - RMSE_l} \right) \times 0.2 + \left( \frac{P_{r\beta} - P_{r\beta_{min}}}{P_{r\beta_{max}} - P_{r\beta_{min}}} \right) \times 0.8 \quad (2.2)$$

with  $RMSE_l$  and  $RMSE_u$  being the lower and upper limits on the RMSE (set to be 0.06 and 1.0, respectively), and  $P_{r\beta}$  representing the pressure range experienced by changing the side slip angle. The objective is to maximize  $J_\beta$ . Two sensor locations (7 and 9) were chosen according to  $J_\alpha$ , while three (1, 3 and 5) were chosen using  $J_\beta$ . Locations symmetric about the centerline were chosen to get a total of 10 locations (locations 1 and 2 are symmetric, etc). The locations chosen can be seen in Figure 1, while select surface fits can be found in Figure 2.

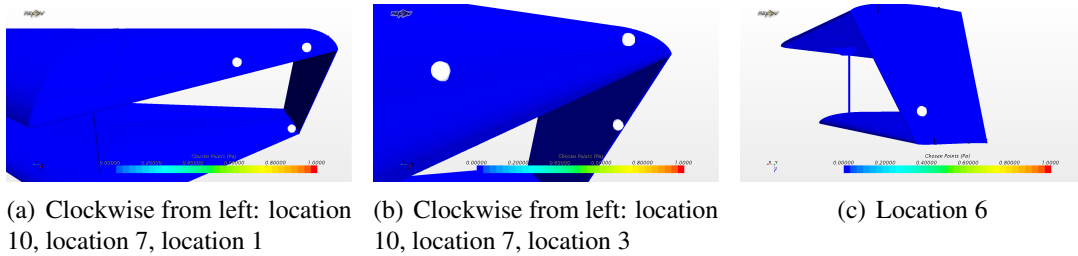


FIGURE 1. Locations of the sensor placements. Locations 1 and 2 are symmetric about the centerline, as are 3 and 4, etc.

### 3. ESTIMATOR

The surface fits obtained through CFD represent a model relating pressure to a given angle of attack and side slip. However, this is an inverse problem, as what is actually measured is pressure, but the objective is to obtain the flow angles. Due to the nonlinearity of the measurement models, and due to the simplicity in implementing the least squares method, nonlinear least squares is the first estimator to be investigated.

Due to the nature of the problem, there is no readily apparent dynamics model relating the flow angles from one time step to the next. There are ways of implementing

<sup>1</sup>The pressure output by the CFD simulation is actually gage pressure (absolute pressure minus static pressure). All references to pressure represent gage from here on out, unless otherwise noted.

## COMBINING CFD AND DISTRIBUTED PRESSURE SENSORS FOR WIND SENSING WITH UAS

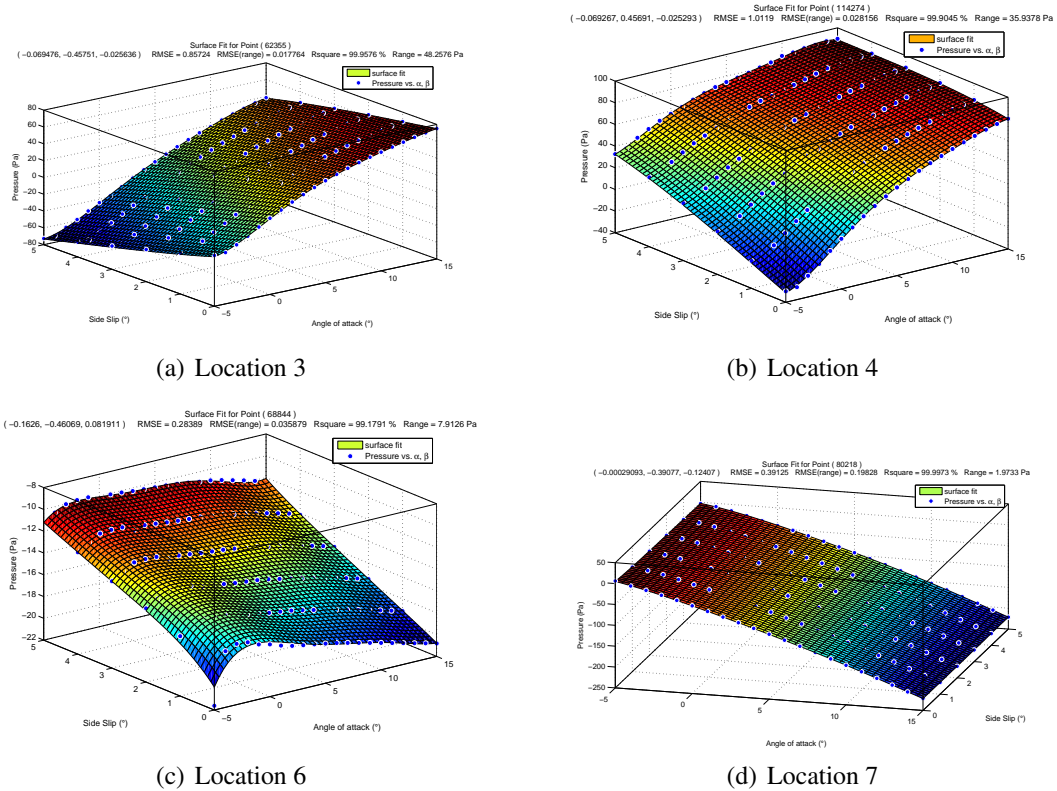


FIGURE 2. Fitted surfaces for locations 3, 4, 6 and 7. These are the measurement models that show how angle of attack, side slip and pressure are related.

a dynamics model, such as assuming the angles are constant during cruise (with some sort of process noise) or using the control inputs with the estimator, but for the time being, it is assumed that the measurements obtained at a certain time are independent of measurements at any other time. This represents a worst case scenario: the estimator can only take advantage of 10 measurements (one per sensor) to estimate the angle of attack and side slip. Future work will involve trying to take advantage of measurements at multiple time steps.

The measurement models will calculate the expected pressure for a given angle of attack and side slip. Sensor noise (obtained during a previous experiment and found to be zero-mean Gaussian with a standard deviation of about 5 Pa) can then be added onto the expected pressures to simulate measurements the sensors would produce. The results from this simulation can be found in Figure 3. The true angle of attack ranged from  $-5^\circ$  to  $15^\circ$ , while the true side slip ranged from  $0^\circ$  to  $5^\circ$ .

As can be seen from the figure, the estimate of  $\alpha$  tracks the truth slightly better than the estimate of  $\beta$ . Just as importantly, the estimates of the  $2\sigma$  error bounds oftentimes don't include the truth (more so in  $\beta$ ). Therefore, it is vital that the estimator is improved upon.

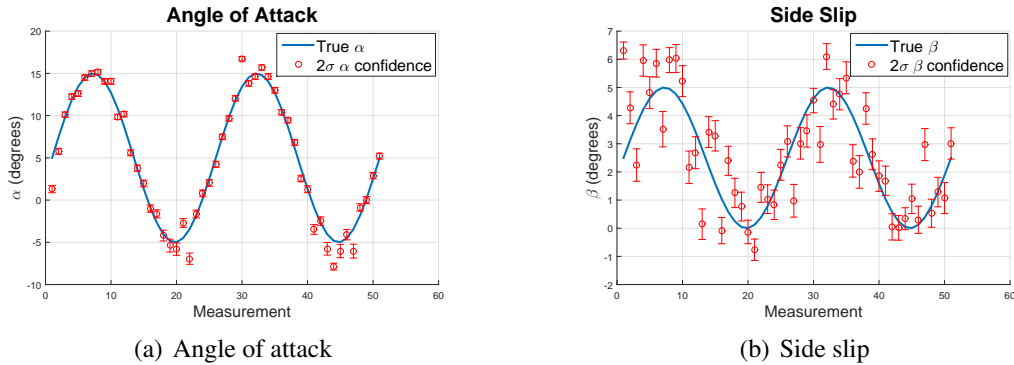


FIGURE 3. Results from the NLS estimator.

#### 4. FUTURE WORK

Much work still needs to be done with this project before flight experiments can be attempted. Work for the near term can be divided into two categories: the scale model and the estimator. For the scale model, assembly is already underway. Once the model is completed, steady state wind tunnel tests can be performed. With regards to the estimator, the nonlinear least squares method can be modified for cruise conditions. This would assume a mean angle of attack and side slip, with fluctuations about the mean. Attractive alternatives to the NLS estimator include nonlinear filters, such as the Extended Kalman Filter, the Unscented Kalman Filter and particle filters. With these filters, it is easier to implement process noise into the state dynamics, in an attempt to leverage more than just the 10 measurements at each time step, and allow for easy integration of control inputs, thereby allowing the filter to operate outside of cruise conditions or steady winds.

After wind tunnel tests have been completed, this project will move towards using the X-8 Skywalker UAS for actual flight experiments, seen in Figure 4 (b) during a deployment last summer. This aircraft has two notable advantages over the Eagle Owl: first, we have more experience flying it, and second, the wings are detachable, enabling different wings to be used. An area of interest is designing new wings that would enable greater accuracy in the estimation of the flow angles.

#### 5. CONCLUSION

Based on the results from the simulations performed up to this point, this project appears to be a viable alternative to using multi-hole probes for wind estimation. The nonlinear least squares method demonstrated how regression analysis could be used for multi-sensor wind estimation. However, alternative schemes, particularly nonlinear filters, should be investigated for improved estimates.

#### 6. ACKNOWLEDGMENTS

I would like to thank Trubee Davison and everyone else involved with STEMinar for all their hard work ensuring the success of the series. I would also like to thank the Graduate School for their continued support of STEMinar. Finally, I wish to acknowledge the support of my advisor Dr. Brian Argrow, along with Dr. Jack Elston, and of

COMBINING CFD AND DISTRIBUTED PRESSURE SENSORS FOR WIND SENSING WITH UAS

the Air Force Office of Scientific Research (under award no. FA9550-12-1-0412) and the National Science Foundation (under award no. AGS-1231096) for their support of this project.

APPENDIX A. AIRCRAFT

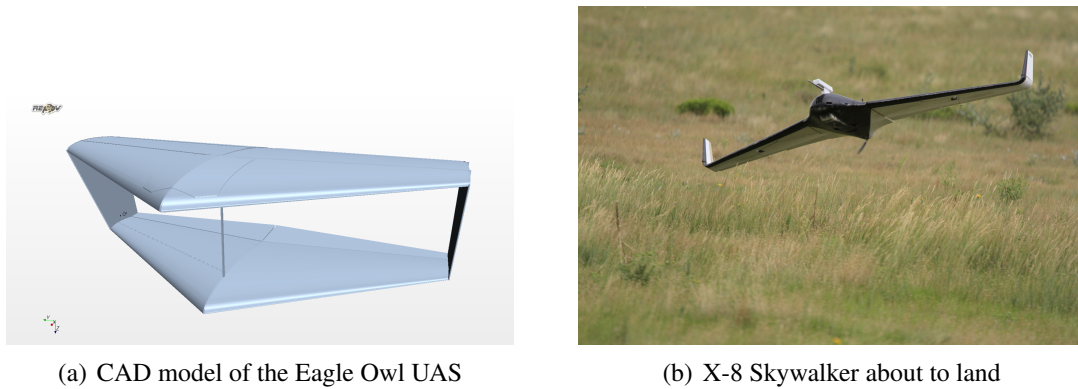


FIGURE 4. The two aircraft currently slated to be used in this project.

REFERENCES

- [1] Laurence III, R. J., Elston, J. S., and Argrow, B. M., "A Low-Cost System for Wind Field Estimation Through Sensor Networks and Aircraft Design", SciTech, Orlando, Florida, Jan 2015.

*E-mail address:* roger.laurenceiii@colorado.edu

DEPARTMENT OF AEROSPACE ENGINEERING SCIENCES, UNIVERSITY OF COLORADO, BOULDER, COLORADO

# KNOTS AND LINKS

CAROLINE MATSON

ABSTRACT. Knots are ubiquitous in our world. We use them to tie our shoes, knit our sweaters, and prevent our boats from floating away. There are many different kinds of knots, and one can be turned into another through the process of untying and retying. But what happens when you take the two loose ends of a knot and join them together? We obtain the mathematical version of a knot, an object that can be pulled and twisted into different shapes but that has no beginning or end. Intuitively we realize that it is no longer true that any knot can be transformed into any other. In this paper we discuss a few of the techniques for distinguishing one knot from another as well as some of the applications of this theory to other areas of math and science.

## 1. AN INTRODUCTION TO KNOT THEORY

In the late seventeenth century, it was believed that all space was filled with a substance called ether. The mathematical physicist William Thompson, also known as Lord Kelvin, hypothesized that atoms were in fact knots within this ether. This theory prompted physicist Peter Guthrie Tait to begin attempting to tabulate all possible knots in order to show that they corresponded with the known elements. Unfortunately for him, it was shown not long after that there was no ether pervading space, and so Lord Kelvin's theory was abandoned. But this mistake gave rise to the theory of knots and links, a field which has continued to develop to this day. [1]

1.1. **Preliminaries.** The study of knots is a subfield of the mathematical subject called topology. Like geometry, topology involves studying the shapes of objects in space. But where geometry is rigid, considering shapes to have fixed angles and sizes, topological objects are allowed to bend and stretch. A sphere and a cube are topologically equivalent since one could be stretched into the other if it were made of a sufficiently pliable material; however, a sphere is not topologically equivalent to a torus, which can be thought of as the surface of a donut, because one cannot be transformed into the other without cutting and gluing the material.

We rigorously define a **knot** to be an equivalence class of embeddings of the circle in the three-dimensional Euclidean space  $\mathbb{R}^3$ , where equivalence is given by ambient isotopy. In less technical terms, this means that a knot is a curve in three-dimensional space with no self-intersections that closes back onto itself. Two knots are the same if one can be deformed into the other by stretching, rotating, and bending it without allowing it to pass through itself. Knot theory also includes the study of links. A **link** is like a knot, but it may have multiple components that may or may not themselves

---

*Date:* August 8, 2015.

*Key words and phrases.* Math.

be knotted. In this paper we focus mainly on knots, which are links with only one component, but many of the results naturally generalize to links.

**1.2. Planar Projections of Knots and Links.** Knots exist in three dimensional space, but they are difficult to study in this context. For this reason we usually consider a specific planar projection of a knot, a two-dimensional representation of a knot that records its shape as seen from one direction as well as its over-and-under crossings.

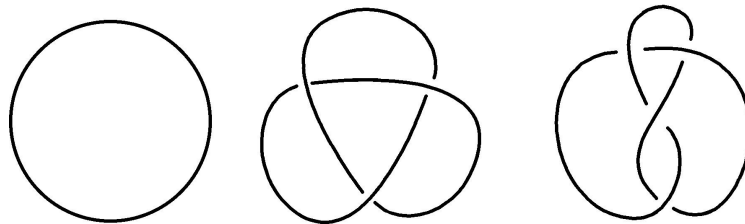


FIGURE 1. Planar projections of the unknot (or trivial knot), the trefoil knot, and the figure-eight knot. [2]

It should be clear that a planar projection of a knot will change under ambient isotopies of the knot in three-dimensional space. Some of these changes will appear as planar isotopies, deformations that pull and stretch the projection without changing any crossings. However, moving a knot in three-space may create, alter, or remove the appearance of crossings in a planar projection. To describe the changes that a projection may undergo, we introduce the **Reidemeister moves**. There are three types: the first

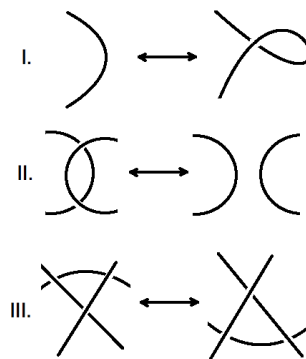


FIGURE 2. Reidemeister moves types I, II, and III.

adds a twist to a strand, the second allows two strands to pass by each other, and the third type allows a strand to move past a crossing which is completely above it. Intuitively, it makes sense that each of these represents a valid transformation of the knot. In fact, every change in a planar projection as a result of ambient isotopy can be represented by combinations of these moves together with planar isotopies. This means that we can show that two planar projections represent the same knot by explicitly constructing a sequence of Reidemeister moves and planar isotopies that transform one into the other.

However, we still have no way of showing that two projections do not represent the same knot. Indeed, we have not even shown that more than one knot exists! Even if we

cannot find a sequence of Reidemeister moves that transforms one knot into the other, that does not mean that such a sequence does not exist. In order to distinguish one knot from another, we will need to introduce some new tools.

## 2. INVARIANTS OF KNOTS

We would like to be able to rigorously prove that certain knots are distinct. Toward this end, we introduce the concept of a **knot invariant**. A knot invariant is a characteristic of a knot that can be computed from a planar projection and which is invariant under planar isotopy and the three Reidemeister moves. If two knots have different values for the same invariant, then they cannot possibly be the same knot.

One such invariant is **tricolorability**. Given a planar projection of a knot, we say that a **strand** is an arc of the projection that passes from one undercrossing to another without passing under any other arc in between. We say that a projection is tricolorable if it is possible to use either two or three different colors to shade the projection in such a way that each strand is one color and at each crossing either only one color is used or all three colors meet.

It should be clear tricolorability is not affected by planar isotopy. For it to be a knot invariant, we must also show that the property of being tricolorable is not changed by Reidemeister moves. Since Reidemeister moves act locally, then we would like to ensure that these moves do not force the exiting strands to change colors, as this could have global effects on the coloring of the knot.

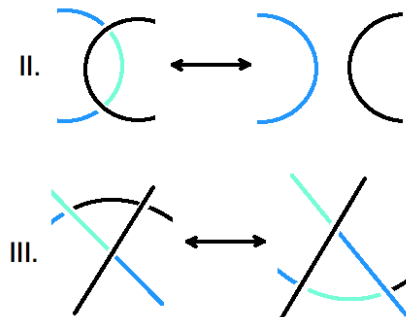


FIGURE 3. Tricolorability is preserved by Reidemeister moves.

Tricolorability is easily seen to be preserved by Reidemeister moves when all strands involved in the move are the same color; since this is the only possibility with type I moves, then they preserve this property. There is only one non-trivial case for type II moves, which is illustrated in Figure 3. Type III has several cases, one of which is illustrated in Figure 3, while the rest are left as an exercise to the reader. Since tricolorability is preserved by Reidemeister moves then it does not depend on the projection of the knot, so it is a knot invariant. Thus we can use it to tell knots apart. For example, the unknot is not tricolorable, since the most obvious projection cannot be shaded using more than one color. However, the trefoil knot is easily seen to be tricolorable, so finally we have shown that the trefoil knot and unknot are distinct! Tricolorability as an invariant is fairly weak; it can only be true or false, so it can only show the existence

of two distinct knots. To distinguish more knots from one another, we turn to a more powerful type of invariant: knot polynomials.

**2.1. Knot Polynomials.** The first knot polynomial was developed by J. Alexander around 1928. It used matrices to calculate a powerful invariant for knots and links. In 1969, John Conway developed a method to recursively calculate the Alexander polynomial using **skein relations**. A skein relation gives a linear relationship between a knot or link diagram and the diagrams obtained by undoing one of its crossings in two different ways. By recursively undoing crossings we end up with a linear expression for the original link in terms of the unknot, and thus we obtain a polynomial. It is important to note at this point that we use the term polynomial loosely here; both negative and fractional powers of the indeterminate are allowed.

We will describe one skein relation and use it to calculate the **bracket polynomial**  $\langle L \rangle$  of a link  $L$ . To undo a crossing, first note that a crossing of two strands splits the plane into four regions. Imagine rotating the over-strand counterclockwise until the two strands meet; the covered regions will be labeled A, and the other regions will be labeled B. Each uncrossing will either be an ‘A’ split, opening up a passage between the two A regions, or vice versa. The following rules give us a method for calculating the bracket polynomial.

$$\begin{aligned} \text{Rule 1: } \langle \bigcirc \rangle &= 1 \\ \text{Rule 2: } \langle \begin{array}{c} \diagup \\ \diagdown \end{array} \rangle &= A \langle \begin{array}{c} \diagdown \\ \diagup \end{array} \rangle + B \langle \begin{array}{c} \diagup \\ \diagdown \end{array} \rangle \\ \text{Rule 3: } \langle LU\bigcirc \rangle &= C \langle L \rangle \end{aligned}$$

FIGURE 4. A method for recursively calculating the bracket polynomial with undetermined coefficients A, B, and C.

We will now go about determining the values of  $A$ ,  $B$ , and  $C$  such that the polynomial is invariant under the three Reidemeister moves. We leave it as an exercise to show that the requirement of invariance under type II Reidemeister moves forces the relations

$$BA = 1 \quad \text{and} \\ A^2 + ABC + B^2 = 0,$$

allowing us to determine that  $B = A^{-1}$  and  $C = -A^2 - A^{-2}$ . It is now simple to show that the bracket polynomial is unaffected by type III Reidemeister moves in the following manner: First undo the central crossing, then use the fact that the bracket polynomial is invariant under type II moves to move the bottom strand over, and then redo the central crossing with the under strand now on the other side.

Lastly, we come to type I moves. These pose a serious problem. The addition of a twist to a strand results in multiplication of the entire polynomial by a factor of  $A^{\pm 3}$ . Thankfully, there is a way to correct this problem. Up until this point, we have ignored an important component of the knot’s position in space: its writhe. Writhe is a measurement of the degree to which a knot twists based on a particular planar projection. We calculate the writhe of a projection of a knot as follows. First, put an orientation on the

knot so that we can think of traversing it in a given direction. Each crossing corresponds to either a clockwise or counterclockwise twist on the positive ends of the strands. We consider counterclockwise twists as contributing  $+1$  to the writhe and clockwise twists as contributing  $-1$ . The sum over every crossing in the projection is the writhe.

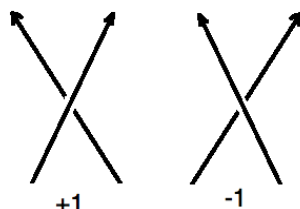


FIGURE 5. Calculating the writhe of a knot. The writhes of the planar projections in Figure 1 are 0,  $-3$ , and 0, respectively.

A Reidemeister type I move always changes the writhe of a knot by  $\pm 1$ . We account for this by creating a new polynomial  $X(L) = (-A^3)^{-w(L)}\langle L \rangle$ . By making the substitution  $A = t^{-1/4}$ , we obtain the **Jones polynomial**, the second invariant knot polynomial to be discovered. Interestingly, despite the substitution of  $t^{1/4}$  this polynomial is a Laurent polynomial for any link with an odd number of components, meaning that only integer powers of  $t$  occur; for an even number of link components, it is a Laurent polynomial multiplied by  $t^{1/2}$ . This invariant gives us a significantly more powerful tool for distinguishing various knots and links from one another. For example, the figure-eight knot has the polynomial  $V_{\text{figure-eight}}(t) = t^2 - t + 1 - t^{-1} + t^{-2}$  [3] while the unknot has the polynomial  $V_{\text{unknot}}(t) = 1$ . This shows that while neither knot is tricolorable, they are in fact distinct. The Jones polynomial can also sometimes distinguish a knot from its mirror image. One embedding of the trefoil knot has the polynomial  $V_{\text{trefoil}}(t) = t + t^3 - t^4$ , while its mirror image has the polynomial  $V_{\text{trefoil}^*}(t) = t^{-1} + t^{-3} - t^{-4}$  [4]. This shows that the trefoil knot is **chiral**, meaning that it has both a left-hand and right-hand form that are not equivalent. Since the development of the Jones polynomial many more polynomials have been discovered, and each provides a new tool for exploring the theory of knots and links.

### 3. APPLICATIONS TO OTHER SCIENCES

Knot theory has several interesting and sometimes surprising applications. One such application is in the field of genetics. Genetic material is stored in the form of DNA molecules, long double-helix strands that are tightly coiled inside the nucleus of every living cell. These molecules are not neatly organized; they are tangled and often become over-twisted, which can affect the ability of enzymes to move up and down the length of the double helix to utilize the information it carries. To correct this, enzymes called **topoisomerases** cut the phosphate backbone of the DNA molecule and guide its untangling before reattaching the two pieces. The resulting molecule has the same chemical structure as before, making it a chemical isomer, but is topologically different. We can use knot theory to learn about the actions of topoisomerases by allowing them to act on pieces of circular DNA and observing any knotting. We can also measure

CAROLINE MATSON

the number of twists an enzyme has added to a molecule by observing supercoiling, a phenomenon in which the writhe of a ribbon or cord in space increases to compensate for being over-twisted. You may have observed this phenomenon with twisted phone or power cords. Supercoiled DNA molecules are more compact, so they can be pulled through gel more quickly. This allows us to easily determine which DNA molecules are experiencing more twisting.

Knot theory can also be used in chemistry in relation to knotted molecules and chirality, in statistical mechanics to study lattices, and in quantum theory to describe entanglement. Knots can generalize to ribbons, which more accurately describe twisting forces, and can be naturally tied to signed planar graphs and to matrices. The theory of knots and links is an intuitive and pleasing subject that is worthy of study not only for its far-reaching applications, but also for its own inherent beauty.

#### 4. ACKNOWLEDGEMENTS

Thanks to Trubee Davison and the STEMinar for organizing this journal, as well as to Slava Krushkal, who first introduced me to knot theory and all its joys.

#### REFERENCES

- [1] C. Adams, *The Knot Book*, American Mathematical Society, Providence, Rhode Island, 2004.
- [2] Bubbles with knotted boundaries. (2009, March 17). Retrieved July 6, 2015.
- [3] Figure Eight Knot. (n.d.). Retrieved July 6, 2015.
- [4] Jones Polynomial. (n.d.). Retrieved July 6, 2015.

*E-mail address:* caroline.matson@colorado.edu

DEPARTMENT OF MATHEMATICS, UNIVERSITY OF COLORADO, BOULDER, COLORADO

# AN INTRODUCTION TO HOMOTOPY TYPE THEORY

MARK PULLINS

**ABSTRACT.** Set theory is commonly used as a foundational system for mathematics. Zermelo-Fraenkel set theory with the axiom of choice is the best known foundational system. However, recent discoveries linking set theory, homotopy theory, and higher category theory have given rise to a new foundational system for mathematics, called homotopy type theory. We will give a brief introduction to the background needed to understand homotopy type theory. Additionally, we will investigate how homotopy type theory treats traditional sets, and how mathematical propositions become objects under the rules of homotopy type theory.

## 1. INTRODUCTION

Although set theory is an area of current mathematical research, it's also a foundational system for mathematics. For this paper, we only need to consider it as a foundational system. In the earliest iteration, sets were imagined as collections of elements that share a particular property. Bertrand Russell famously found this to be too general when he imagined the set:

$$S = \{x : x \notin x\}.$$

This is the set of all sets that are not elements of themselves [3]. Russell asked whether or not  $S \in S$ . If  $S \in S$ , then  $S \notin S$  by definition and if  $S \notin S$ , then  $S \in S$ , by definition. We reach a contradiction either way. Today, axiomatic set theory is studied instead, which consists of a list of axioms that we accept as true. Zermelo-Fraenkel set theory with the axiom of choice, known as ZFC, is the most commonly known list of axioms. Selecting the correct axioms is incredibly important. We need to pick axioms that won't prove anything false; this is called being consistent. At first, we believed we could prove everything with the correct axioms, which is called being complete. However, Gödel proved that no axiom system can be complete and consistent.

Homotopy type theory is an alternative to set theory for foundational mathematics. Instead of relying on set theory, homotopy type theory uses recent connections between type theory, set theory, homotopy theory, and higher category theory. To gain a basic understanding of homotopy type theory, only a surface level understanding of type theory and homotopy theory is required. We will introduce the necessary concepts and use these to revisit some foundational concepts.

## 2. BACKGROUND

**2.1. Homotopy Type Theory Versus Set Theory.** Before moving to homotopy type theory, we should point out a few key differences between it and set theory. From now on, set theory will mean ZFC.

---

*Date:* August 8, 2015.

*Key words and phrases.* Math.

In set theory, we have the deductive system found in first-order logic on one layer, and on another layer we have the axioms selected in our axiomatic system. Type theory contains only a single layer; the deductive system is built into the theory. Everything is a type, including mathematical propositions, which are statements that can be proven true or false. This is fairly exotic because in set theory, propositions are not considered mathematical objects. Therefore, the act of proving a theorem is now equivalent to constructing an element of a specific type.

The second major difference is how we view equality. In type theory, there are two types of equality: propositional and judgmental. To say that  $a$  and  $b$  are propositionally equal in a type  $A$ , we write  $a =_A b$ . This statement is also a type. The other type of equality is judgmental equality; it says that two things are equal due to the definition, which does not create a new type. An example would be if  $f(x) = x^3$ , then  $f(3) \equiv 27$ . We use  $\equiv$  to mean judgmentally equal to avoid confusion.

Finally, it is worth noting that type theory is comprised solely of rules. That means there are no axioms. However, homotopy type theory does include some axioms, but they are irrelevant in the context of this paper.

**2.2. Type Theory.** Everything in type theory is a type. We write  $a : A$  to mean that ' $a$  has type  $A$ '. Other ways to say this include ' $A$  has proof  $a$ ' and ' $a$  is a witness to  $A$ '. When  $A$  represents a proposition, it's often easier to consider  $a$  as evidence rather than an element. Covering all the major types in type theory is too extensive, so we will only cover the basics. The general pattern found in [1] for introducing a new type is listed below:

- (1) **Formation Rules:** how to form new types of this kind.
- (2) **Constructors, Introduction Rules:** how to construct elements of this type.
- (3) **Eliminators, Elimination Rules:** how to use elements of this type.
- (4) **Computation Rule:** how an eliminator acts on a constructor.
- (5) (optional) **Uniqueness Principle:** expresses uniqueness of maps into or out of this type.

If we explicitly follow this pattern, it's easier to understand new types. Here is an introduction to the function type:

- (1) Given types  $A$  and  $B$ , we form the function type  $A \rightarrow B$  with domain  $A$  and codomain  $B$ . This is a rare instance of our normal notation for a function  $f : A \rightarrow B$  corresponding to the same thing in type theory.
- (2) To construct an element of  $A \rightarrow B$ , we can use either direct definition or  $\lambda$ -abstraction. To define  $f : A \rightarrow B$ , we write

$$f(x) ::= \Phi$$

where  $\Phi$  is some expression involving  $x$ . This is direct definition. Alternatively, we could use  $\lambda$ -abstraction and write

$$\lambda(x : A). \Phi$$

without using  $f$ .

- (3) The eliminator is function application. We take  $f : A \rightarrow B$  and  $a : A$ , then  $f(a) : B$ . This is the only elimination rule.
- (4) The computation rule states that when we apply  $f$  to  $a$ , then we can just replace  $x$  with  $a$  every time it appears in  $\Phi$ .
- (5) The uniqueness principle is that  $f \equiv \lambda(x : A).f(x)$ , which means that  $f$  is uniquely determined by its values.

To understand how sets are defined in homotopy type theory, we also need to discuss the dependent function type. We call  $\mathcal{U}$  the universe. A universe is a type whose elements are types. To form the type of dependent functions, we need a type  $A : \mathcal{U}$  and a family  $B : A \rightarrow \mathcal{U}$ . Then the dependent function type is written as

$$\prod_{(x:A)} B(x)$$

This is similar enough to the function type, that we will not delve into specifics; however, we will explain what  $B(x)$  denotes. Think of  $B$  as a function that takes  $x : A$  and returns a different codomain,  $B(x)$ . So, for  $f : \prod_{(x:A)} B(x)$ , then the codomain is dependent on  $x : A$ .

There are two other types worth briefly mentioning: products and coproducts. A product of two types,  $A$  and  $B$ , is written as  $A \times B$ . The null product type, which we denote  $\mathbf{1}$  has a single element,  $\star : \mathbf{1}$ . A coproduct of two types,  $A$  and  $B$ , is written as  $A + B$ . The empty coproduct, which we denote  $\mathbf{0}$ , has no elements.

**2.3. Homotopy Theory.** In this section, when we mention a space  $X$ , we are referring to a collection of points equipped with a topology.

**Definition 2.1.** [2] Given points  $x$  and  $y$  of a space  $X$ , a **path** in  $X$  from  $x$  to  $y$  is a continuous map  $f : [0, 1] \rightarrow X$  such that  $f(0) = x$  and  $f(1) = y$ .

Since we have introduced paths, we need a way of equating paths.

**Definition 2.2.** [2] If  $f$  and  $g$  are continuous maps of the space  $X$  into the space  $Y$ , we say that  $f$  is **homotopic** to  $g$  if there is a continuous map  $F : X \times [0, 1] \rightarrow Y$  such that

$$F(x, 0) = f(x) \quad \text{and} \quad F(x, 1) = g(x)$$

for each  $x$ . The map  $F$  is called a **homotopy** between  $f$  and  $g$ .

We want to start viewing types,  $A$ , as abstract spaces, and  $a : A$  as points in these spaces. In homotopy type theory, we think of  $p : x =_A y$  as a path that starts at  $x$  and ends at  $y$ . And, if we have  $p, q : x =_A y$ , then these are equivalent if  $p$  and  $q$  are homotopic.

There is no reason to stop at homotopies between paths. With a little imagination we can create homotopies between homotopies, then homotopies of those, and so on. There is a straightforward, albeit cluttered, way to express this in type theoretic notation. Say  $r$  is a homotopy between  $p$  and  $q$ , then  $r : p =_{(x=_A y)} q$ , where  $p, q : x =_A y$ . Then let's say  $r$  and  $s$  are homotopically equivalent, so we write

$$r =_{(p=(x=_A y)q)} s$$

## 3. SETS AND LOGIC IN HOMOTOPY TYPE THEORY

While we still want to view types as abstract spaces, there are some types that do behave more like traditional sets. We also must consider how to treat propositions, which are statements that can be proven true or false. Unlike ZFC, propositions are types in homotopy type theory, so we must be able to classify when a type is more like a proposition. Central to both of these concepts is the idea of types containing higher homotopic information. Please note that the following definitions, theorems, lemmas, and examples come from [1], if the reader would like a more in-depth coverage.

**3.1. Sets.** Sets, as we know them, only contain information about which elements are members. In a homotopic sense, all paths between points are the same. Thus, the following definition makes sense.

**Definition 3.1.** *A type  $A$  is a set if for all  $x, y : A$  and all  $p, q : x =_A y$ , we have  $p = q$ .*

We can define a type  $\text{isSet}(A)$  to check whether or not a type  $A$  is a set by writing

$$\text{isSet}(A) := \prod_{(x,y:A)} \prod_{(p,q:x=Ay)} p =_{(x=Ay)} q$$

This means that if  $\text{isSet}(A)$  is occupied, then  $A$  is a set.

Sets may also be referred to as **0-types**. This stems from the definition of a 1-type:  $A$  is a **1-type** if for all  $x, y : A$  and  $p, q : x = y$  and  $r, s : p = q$ , then  $r = s$ . Notice that this pattern can be continued to form the homotopy  $n$ -types. These are actually analogous to  $n$ -groupoids in category theory, which we will not discuss here. Notice that 0-types aren't even the simplest, since a  $-1$ -type would still make sense. The  $-1$ -type will actually allow us to fix some problems that occur with propositions.

**3.2. Propositions.** In homotopy type theory, we can interpret the types as symbols in first order logic. Under this interpretation, we can view the types as propositions, which makes the transition for a logician a bit simpler. Unfortunately, many types contain extra homotopic information, which their logical equivalents do not. Because of this, some tautologies in first order logic won't always be true in homotopy type theory.

**Theorem 3.2.** *It is not the case that for all  $A : \mathcal{U}$  we have  $A + \neg A$ .*

The proof is extremely complicated and can be found in [1] for the curious reader. The logical interpretation of this is  $A \vee \neg A$ , which can be thought of as 'A is true or A is not true'. This is called the law of excluded middle and is accepted in almost all mathematical circles. The problem with the type  $A + \neg A$  is that it contains higher homotopic information, whereas the first order formula does not. But there are still types that behave more like propositions and can be considered true or false.

**Definition 3.3.** *A type  $P$  is a mere proposition if for all  $x, y : P$ , we have  $x = y$ .*

Like with sets, we want to express this type, which is:

$$\text{isProp}(P) := \prod_{x,y:P} x = y$$

Our motivation for defining mere propositions stems from a search for type theoretic objects that act like normal propositions. In other words, if  $P$  is inhabited, it should be true and if  $P$  is not inhabited, then  $\neg P$  should be inhabited.

**Lemma 3.4.** *If  $P$  and  $Q$  are mere propositions such that  $P \rightarrow Q$  and  $Q \rightarrow P$ , then  $P \cong Q$ .*

*Proof.* Since  $P \rightarrow Q$  and  $Q \rightarrow P$ , then there must be  $f : P \rightarrow Q$  and  $g : Q \rightarrow P$ . For any  $x : P$ , then  $g(f(x)) = x$ , since  $P$  is a mere proposition and for any  $y : Q$ , then  $f(g(y)) = y$  since  $Q$  is a mere proposition. We conclude that  $f$  and  $g$  are quasi-inverses, and thus  $P \cong Q$ . □

**Theorem 3.5.** *If  $P$  is a mere proposition and  $x : P$ , then  $P \cong \mathbf{1}$ .*

*Proof.* We will accept as fact that  $\mathbf{1}$  is a mere proposition. Construct  $f : P \rightarrow \mathbf{1}$  by  $f(y) := \star$ , and construct  $g : \mathbf{1} \rightarrow P$  by  $g(z) := x$ . By Lemma 3.4, we have that  $P \cong \mathbf{1}$ . □

If we imagine  $\mathbf{1}$  as meaning true, then our definition of mere propositions acts exactly like we hoped. We have properly defined two familiar mathematical concepts in the language of homotopy type theory, now we'll conclude by seeing a few examples of sets.

**Example 3.6.**  $\mathbb{N}$ , the natural numbers, is a set. It can be proven within homotopy type theory that for any  $x, y : \mathbb{N}$  the equality type  $x =_{\mathbb{N}} y$ , is equivalent to either  $\mathbf{1}$  or  $\mathbf{0}$ .  $\mathbf{0}$  is the empty type, so it is vacuously true that any two elements are equal. It is also true that any two elements of  $\mathbf{1}$  are equal. Therefore, all paths are equal.

**Example 3.7.** The universe  $\mathcal{U}$  is not a set. Look at the type  $\mathbf{2} : \mathcal{U}$ , which is the same as  $\mathbf{1} + \mathbf{1}$ . We define  $0_2 = \star$  from the left  $\mathbf{1}$  and  $1_2 \equiv \star$  from the right  $\mathbf{1}$ . These are unique elements. Now construct  $f : \mathbf{2} \rightarrow \mathbf{2}$  by defining  $f(0_2) = 1_2$  and  $f(1_2) = 0_2$ . We have that  $f(f(x)) = x$  and so  $f$  gives rise to a path  $p$ , which is not the same as the identity path. Therefore, we have two paths which are not equal, which implies that  $\mathcal{U}$  is not a set.

#### 4. CONCLUSION

Since all proofs are constructions, homotopy type theory can feel very exotic compared to normal mathematical argument. Additionally, the loss of the law of excluded middle make it seem like a less attractive option to ZFC. Homotopy type theory does have one significant advantage though. Traditional mathematics is performed by humans and checked by humans; it doesn't translate well into the language of computers. On the other hand, homotopy type theory proofs are more easily checked by software, such as Coq. Reworking the foundations of math in terms of homotopy type theory opens up possibilities for proof checking. But even without this advantage, the way homotopy type theory links type theory, set theory, homotopy theory, and category theory, four very different mathematical areas, is intriguing enough to deserve future study.

#### 5. ACKNOWLEDGEMENTS

I'd like to thank Trubee Davison and the STEMinar for giving me the opportunity to contribute to this journal.

MARK PULLINS

REFERENCES

- [1] The Univalent Foundations Program, *Homotopy Type Theory: Univalent Foundations of Mathematics*, <http://homotopytypetheory.org/book>, 2013.
- [2] J. Munkres, *Topology*, Prentice Hall, 2000.
- [3] J. Jech, *Set Theory*, Springer, 2003.

*E-mail address:* `Mark.Pullins@colorado.edu`

DEPARTMENT OF MATHEMATICS, UNIVERSITY OF COLORADO, BOULDER, COLORADO

# **SIMULATION OF IMPACT OF BUBBLE DYNAMICS ON CELL MEMBRANE USING AN ADAPTIVE WAVELET CODE**

NAVID SHERVANI-TABAR

**ABSTRACT.** This research aims to develop a computational methodology to study the growth and collapse of a cavitation bubble near a membrane. In order to conduct this research, a computational approach involving integrating of level set methods with adaptive wavelet collocation method is being developed to track the propagation of the front of a curve and surface. This methodology approaches to be a base to investigate the growth and collapse of a cavitation bubble and study its effects on the cell membrane.

## 1. INTRODUCTION: CAVITATION

Cavitation is inception and rapid collapse of vapour cavities in a liquid zone. This phenomenon occurs when the liquid is subjected to a pressure less than the pressure of the saturated vapour in a specific temperature [1]. The outcomes of the collapse of a cavitation bubble are a microjet and a large shockwave [2]. Shockwaves are formed when the cavities rapidly expand or collapse. Collapse of the cavitation bubbles generates alternative highly intensive stresses [3]. These stresses are considered to have many adverse impacts on such cases as hydraulic machineries and shuttle turbopumps. However, it can positively affect human life in many ways. For instance, it has influenced the medical techniques to destruct the kidney stone, demolish the fat cells tissue, and dismantle tumors.

The impact load due to the collapse of the cavitation bubbles can cause major destructions. The cavitation bubble collapse is very harmful to the impeller of a hydraulic machine, which causes erosion and results in failure of the hydromachineries due to damages to its impellers. Therefore, cavitation is one of the most important parameters of pumps and hydraulic machineries design [4].

On the other hand, recent studies have shown useful applications of the bubbles. Cavitation has a broad range of applications in medicine. The shockwaves generated by the collapse of the bubbles can help in destruction of kidney stones. Cavitation bubbles can also lead to enhanced heating in the focal region of the High-Intensity Focused Ultrasound (HIFU) which is a thermal noninvasive treatment methodology for cancer [5].

Life time of a cavitation bubble is very short and is in the scale of micro-seconds or Nano-seconds. Avellan and Farhat in their work stated that the collapse of the bubbles happens only in a very short period of time, about several nanoseconds [2].

---

*Date:* August 8, 2015.

*Key words and phrases.* Wavelet, Level Set Method, Cavitation, CFD.

## 2. COMPUTATIONAL FLUID DYNAMICS

Computational Fluid Dynamics (CFD) is a field of fluid mechanics which aims to analyze the fluid motion with computer simulation. During the recent decade many researchers have carried out investigations with the aid of the set of methods developed in this area. The capability for simulation of flows has significantly affected recent developments in designing parameters [6].

## 3. WAVELETS

Wavelets, introduced in 1984 by Grossmann and Marlet, have significantly affected the science and technology [7]. The first utilization of the wavelets in fluid mechanics dates back to early 90's [8]. The unique properties of wavelets have resulted them to be a suitable choice to solve the Partial Differential Equations (PDE's) on adaptive grids [9]. Application of wavelets in CFD problems has been introduced at early 90's.

Wavelets are basis functions that are localized in both physical space and wave-number space. In this research, adaptive wavelet collocation method (AWCM), which is a general solution technique for solving differential equations on adaptive, collocated grids, will be used. This method uses wavelet properties to determine, on the fly, significant points needed for an accurate solution [9].

Despite their short existence, many wavelet techniques have been developed for numerical simulations of compressible and incompressible Euler and Navier-Stokes equations for both inert and reactive flows. The ability to precisely identify, isolate, and track localized, dynamically dominant flow structures such as shocks and flame fronts on adaptive computational meshes has distinguished wavelet techniques from conventional methods [9].

Wavelet techniques in CFD are a relatively new and advancing area, which involve many challenging issues to be investigated.

## 4. LEVEL SET METHOD

Level set method is a mathematical method to investigate the evolution of curves and surfaces. Propagation of the boundaries and interfaces occurs in nature in the form of ocean waves, burning flames, etc. This method was first developed by Sethian at University of California Berkley [10]. The main difference between level set method and the conventional methods is that in this method the points are not being evolved and interpolated to find the "front". The front is defined by the zero level set of a signed distance function. Mathematically, it is represented as  $\phi(\vec{x}) = 0$  in a 3D plane. The main equation of the evolution of the level set is [11]

$$\frac{d\phi}{dt} + (\vec{F} \cdot \nabla)\phi = 0,$$

where  $\vec{F}$  denotes the speed of the front in the normal direction to the boundary. The normal direction to the front is the same as gradient [11]

$$\vec{n} = \frac{\nabla(\phi)}{|\nabla(\phi)|}.$$

At the beginning of the iterations,  $\phi$  might be a distance function but later on, after  $\phi$  has evolved for some iterations, the gradient gets out of hand. In this case, we reinitialize it to make the modulus of the gradient to be 1 again. Therefore, to reinitialize the  $\phi$ , we solve the equation

$$1 - i \nabla \phi \vee i$$

$$\phi_t = \text{sign}(\phi)i$$

which provides us with a new value  $\phi$  that has the property  $|\nabla \phi| = 1$ .

In this research the growth and collapse of a bubble near a membrane would be investigated using a wavelet based level set method to track the front of the bubble. To do so, the level set method was implemented on the existing wavelet code. This consists of the following steps:

- Implementing level set evolution equation.
- Implementing reinitialization procedure.

In each step, the reinitialization subroutine is being called and it results in diffusing the regions, information of where we do not need and it convects the area within  $\delta \Delta x$  of the zero level set, where  $\delta$  and  $\Delta x$  are a constant integer and the distance between two adjacent grid points, respectively.

To compute the fluid motion, the Navier-Stokes equation had been implemented on the code.

## REFERENCES

- [1] Shervani-Tabar, M. T., Shervani-Tabar, N., "Movement of Location of Tip Vortex Cavitation along Blade Edge due to Reduction of Flow Rate in an Axial Pump," *International Journal of Mechanical and Aerospace Engineering*, 6 2012 (2012).
- [2] Avellan, F., Farhat, M., "Shock pressure generated by cavitation vortex collapse," *Proceedings of the Third International Symposium on Cavitation Noise and Erosion in Fluid Systems, FED-vol. 88, ASME Winter Annual Meeting, San Francisco, CA*, pp. 119 125. (1989)
- [3] Brennen, C. E., *Cavitation and Bubble Dynamics*, Oxford University Press, London, 1995.
- [4] Wei-guo, Z., Ling-xin, Z., "Numerical simulation of cavitation flow under high pressure and temperature," *Journal of Hydrodynamics*, 2011,23(3):289-294, doi: 10.1016/S1001-6058(10)60115-1 (2011)
- [5] Chen, H., Li X., Wan M., "The Inception of Cavitation Bubble Clouds Induced By High-Intensity Focused Ultrasound," *Ultrasonics*, 44 (2006) e427-e429, doi:10.1016/j.ultras.2006.05.021 (2006)
- [6] Zhang X. B., Qiu L. M., Gao Y., Zhang X. J., "Computational fluid dynamic study on cavitation in liquid nitrogen," *Cryogenics*, 48 (2008) 432 438, doi:10.1016/j.cryogenics.2008.05.007 (2008)
- [7] Grossmann A., Morlet J., "Decomposition of Hardy functions into square integrable wavelets of constant shape," *SIAM J. Math. Anal.* 15:723-36 (1984)
- [8] Farge M., "Wavelet transforms and their application to turbulence," *Annu. Rev. Fluid Mech.* 24:395-457 (1992)
- [9] Schneider K., Vasilyev O. V., "Wavelet Methods in Computational Fluid Dynamics," *Annu. Rev. Fluid Mech.* 2010. 42:473-503 (2010)
- [10] Sethian J. A., *An analysis of flame propagation*, Ph.D. dissertatiobn, Department of Mathematics, University of California, Berkley, 1982.
- [11] Sethian J. A., *Level Set Methods and Fast Marching Methods: Evolving interfaces in computational geometry, fluid mechanics, computer vision, and materials science (Second Edition)*, Cambridge University Press, New York, 1999.

NAVID SHERVANI-TABAR

*E-mail address:* navidst@colorado.edu

DEPARTMENT OF MECHANICAL ENGINEERING, UNIVERSITY OF COLORADO, BOULDER, COLORADO